Soft-Chemical Synthesis and Electrochemical Properties of Lithium Transition Metal Oxides

Kazuki CHIBA

February 2019

Soft-Chemical Synthesis and Electrochemical Properties of Lithium Transition Metal Oxides

Kazuki CHIBA

Doctoral Program in Nano-Science and Nano-Technology

Submitted to the Graduate School of

Pure and Applied Sciences

in Partial Fulfillment of the Requirements

for the Degree of Doctor of Philosophy in

Engineering

at the

University of Tsukuba

Contents

Chapter I
Introduction

Section I-I Introduction

Compared with other secondary batteries, lithium ion secondary batteries (LIBs) have excellent characteristics such as high energy density and high voltage. Therefore, they are widely used as power sources for smartphones and laptop computers. Since the number of battery electric vehicles increase in future, higher capacity, higher potential, and lower cost of LIBs are required. LIBs are composed of four parts: positive electrode, negative electrode, separator, and electrolyte. Among these parts, $LiCoO_2$ with layered rock-salt type structure is considered as a positive electrode active material. $LiCoO_2$ shows reversible Li^+ extraction and insertion reaction of about 4 V vs Li/Li^+. Although the theoretical capacity of $LiCoO_2$ is 274 mAh g^{-1}, there is a problem in the stability of the crystal structure at the time of charge. Actually, it can only use about half of the theoretical capacity.

Since this active material uses Co, which is a rare metal, it is expensive. In addition, 35% of the world's Co production is used in the battery industry. From these facts, only $LiCoO_2$ cannot meet future demand growth. For this reason, lithium transition metal oxides containing Mn and Ni, which are less expensive than Co, are being developed as promising alternative materials for $LiCoO_2$ with layered rock-salt type structure.

$LiMn_2O_4$ ($Li_{0.5}MnO_2$) with spinel-type structure is known as a positive electrode active material having high thermal stability, the theoretical capacity of 148 mAh g^{-1}, and Li^+ extraction and insertion reaction of about 4 V vs Li/Li^+. $Li_{0.44}MnO_2$ has tunnel structure and is prepared using tunnel-type $Na_{0.44}MnO_2$ as a starting material [1-8]. Because $Li_{0.44}MnO_2$ is metastable, it is prepared from $Na_{0.44}MnO_2$ via Na/Li ion-exchange reaction at a relatively low temperature. Such a preparation method is called soft chemical synthesis. Figure 1-1 shows the crystal structure of $Li_{0.44}MnO_2$. Unlike $LiMn_2O_4$ ($Li_{0.5}MnO_2$) with spinel-type structure and $LiMnO_2$ with layered rock-salt type structure, the crystal structure of $Li_{0.44}MnO_2$ has been reported to not undergo phase transition during charge and discharge cycles [9-12]. However, when graphite is used as the negative electrode active material, the specific capacity is low because the amount of Li in the crystal structure of $Li_{0.44}MnO_2$ is small.

In addition, substituting Ni or Co for a part of Mn in $LiMn_2O_4$ with spinel-type structure increases the charge and discharge potential. The charge and discharge potential of Ni-substituted $LiNi_{0.5}Mn_{1.5}O_4$ is 4.7 V vs Li/Li^+, which is higher than $LiMn_2O_4$. The Mn valence number of $LiNi_{0.5}Mn_{1.5}O_4$ is tetravalent, and it has a high charge and discharge potential due to the redox reaction of Ni^{2+}/Ni^{4+}. On the other hand, the charge and discharge potential of Co-substituted $LiCoMnO_4$ is 5.2 V vs Li/Li^+, which is even higher than $LiNi_{0.5}Mn_{1.5}O_4$ due to the redox reaction of Co^{3+}/Co^{4+} [13]. Furthermore, $LiCoMnO_4$ is expected as a high-potential positive electrode of all-solid-state LIBs because the volume change in charge and discharge reaction is small [14]. However, due to the cation-mixing of Li/Co atoms, the specific capacity is low [15].

The common feature of both layered rock-salt type and spinel-type is the crystal structure of rock-salt type based on the cubic close-packed structure of O atoms. Figure 1-2 shows rock-salt type MnO, layered rock-salt type $LiCoO_2$, and spinel-type $LiMn_2O_4$. In rock-salt type MnO, Mn atom occupies the octahedron center composed of O atoms in the cubic close-packed structure. On the other hand, in layered rock-salt type $LiCoO_2$, Li atom occupies 1/2 of the octahedron

center composed of O atoms in the cubic close-packed structure, and Co atom occupies the remaining octahedron. Furthermore, in spinel-type $LiMn_2O_4$, Li atom occupies 1/2 of the tetrahedron center composed of O atoms in the cubic close-packed structure, and Mn atoms occupies 1/2 of the octahedron. In this way, both the layered rock-salt type and the spinel-type adopt the arrangement of O atoms of the rock-salt type. Therefore, the layered rock-salt type structure undergoes phase transition to the spinel-type structure during charge and discharge cycles. Layered rock-salt type $Li_{0.67}Ni_{0.33}Mn_{0.67}O_2$ is expected as a high capacity material, but it has not been put to practical use for the same reason [16].

In this study, we used Mn and Ni with less resource constraints than Co, synthesized tunnel-type $Li_{0.44}MnO_2$, spinel-type $LiCoMnO_4$, layered rock-salt type $Li_{0.67}Ni_{0.33}Mn_{0.67}O_2$ by soft chemical method. Furthermore, it aimed to clarify the crystal structure and electrochemical properties of them.

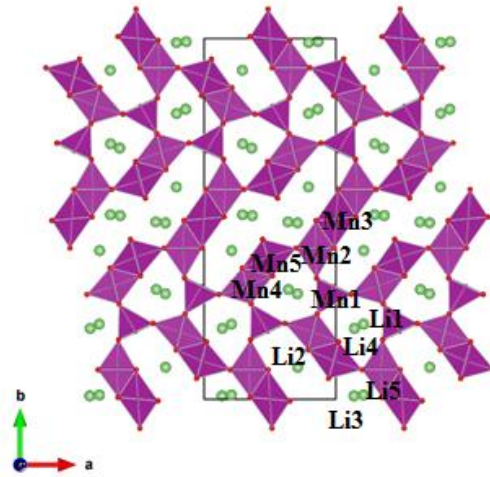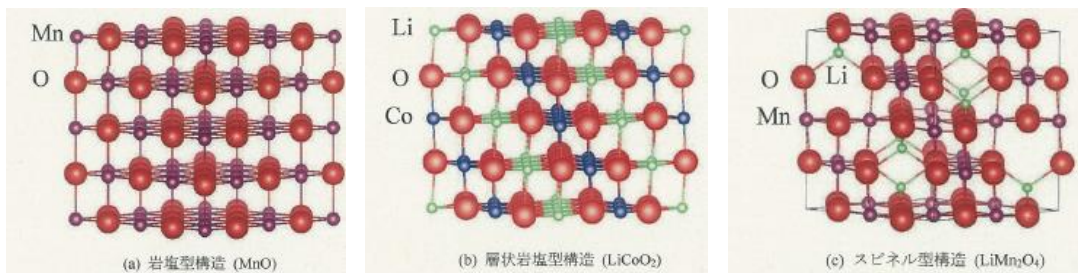Fig.1-1-1 Crystal structure of $Li_{0.44}MnO_2$.

Fig. 1-1-2 Comparison of (a) rock-salt type MnO, (b) layered rock-salt type $LiCoO_2$, and (c) spinel-type $LiMn_2O_4$.

Section I-II   Soft-chemical synthesis

In recent years, application of ion exchange reaction to material synthesis has attracted attention. Synthesis method by Host-Guest reaction such as ion exchange is said to be soft chemical synthesis because it can be synthesized under mild reaction conditions such as relatively low temperature as compared with the inorganic synthesis method [17].

Conventional inorganic syntheses include solid state reaction, flux, hydrothermal, sol-gel method, and others. In these synthesis methods, the chemical composition and the crystal structure of the starting material are brought into disjointed state and then recombined to synthesize the target material having a new chemical composition and crystal structure (Fig. 1-2-1). Therefore, it is difficult to predict and synthesize the chemical composition and crystal structure of the target material. Compared with these synthesis methods, soft chemical synthesis uses raw materials that can perform Host-Guest reaction such as ion exchange as starting materials. An inorganic compound can be converted into a new chemical composition and crystal structure by completely or partly leaving the chemical bond of the framework. That is, it can be said to be a synthetic method having an idea similar to organic synthesis. Since soft chemical synthesis uses the chemical bond of the starting material, it is usually possible to synthesize even under mild reaction conditions at relatively low temperature.
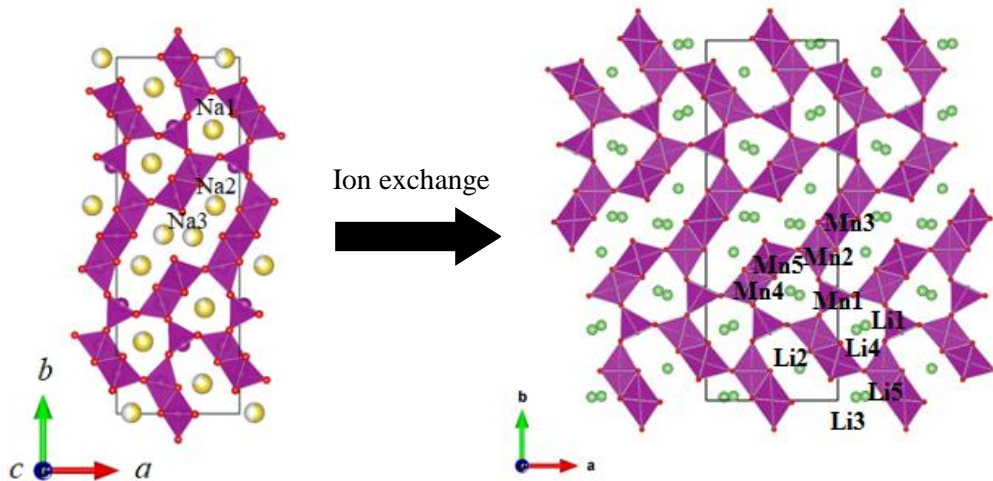
Fig. 1-2-1 Ion exchange reaction from $Na_{0.44}MnO_2$ to $Li_{0.44}MnO_2$.

Section I-III   Crystal structure analysis

Rietveld analysis is a structural analysis method that refines crystal structure for powder X-ray and neutron diffraction patterns. A crystal structure model is obtained from the assumed crystal structure model by least squares method between an ideal and an observed diffraction profile. There is R factor as reliability factor for estimating the progress of Rietveld analysis and the degree of agreement between the observed intensity y_i and the calculated intensity $f_i(x)$. Typical R factors are shown in (1) to (3). In the equation, N represents the number of observed data and P represents the number of parameters to be refined. Among these R factors, the most important factor R is R_{wp} (R-weighted pattern). However, since R_{wp} and R_p (R-pattern) are equal to the summation of the observation intensities of the denominator, diffraction intensity and

4

background intensity largely affect these values. Therefore, the index S for comparing R_{wp} and R_p equal to the expected minimum R_{wp} indicates fitness. In equation (4), $S = 1$ means that refinement is best.

$$R_{\mathrm{wp}} = \left\{ \frac{\sum_i w_i \left[y_i - f_i(\mathbf{x}) \right]^2}{\sum_i w_i y_i^2} \right\}^{1/2} \tag{1}$$

$$R_{\mathrm{p}} = \frac{\sum_i |y_i - f_i(\mathbf{x})|}{\sum_i y_i} \tag{2}$$

$$R_{\mathrm{e}} = \left(\frac{N - P}{\sum_i w_i y_i^2} \right)^{1/2} \tag{3}$$

$$S = \frac{R_{\mathrm{wp}}}{R_{\mathrm{e}}} = \left\{ \frac{\sum_i w_i \left[y_i - f_i(\mathbf{x})^2 \right]}{N - P} \right\}^{1/2} \tag{4}$$

X-ray absorption fine structure (XAFS) is observed near the X-ray absorption edge. By the analysis of XAFS, information such as the electronic state of X-ray absorbing atoms and nearby structure can be obtained. Unlike X-ray crystal structure analysis, the measurement sample does not require long distance order and is not limited to the crystalline material. In X-ray Absorption Spectroscopy, X-ray is incident on the measurement sample and its absorption spectrum is analyzed. As the energy of the incident X-ray is gradually increased, the absorption coefficient of the X-ray abruptly increases with energy corresponding to the binding energy of the inner shell electron of the X-ray absorption atom in the measurement sample. In the X-ray absorption spectrum, this edge structure is called an absorption edge. Since the energy at the absorption edge is determined by the absorbed atom and the electron arrangement of the excited inner shell electrons, it is written as Co K absorption edge, Mn K absorption edge or the like by using the symbol of the element and the symbol of the electron shell. When the energy of the incident X-ray becomes larger than the absorption edge, the absorption coefficient gradually decreases. However, a change in absorption coefficient is observed from the absorption edge to the high energy region of about 1000 eV. This fine structure is XAFS.

References

[1] M. M. Doeff, M. Y. Peng, Y. Ma, L. C. De Jonghe, *J. Electrochem. Soc.* **141** (1994) L145.

[2] M. M. Doeff, T. J. Richardson, L. Kepley, *J. Electrochem. Soc.* **143** (1996) 2507.

[3] A. R. Armstrong, H. Huang, R. A. Jennings, P. G. Bruce, *J. Mater. Chem.* **8** (1998) 255.

[4] Y. U. Jeong, A. Manthiram, *Electrochem. Solid-State Lett.* **2** (1999), 421.

[5] M. M. Doeff, A. Anapolsky, L. Edman, T. J. Richardson, L. C. De Jonghe, *J. Electrochem. Soc.* **148** (2001), A230.

[6] Y. U. Jeong, A. Manthiram, *J. Solid State Chem.* **156** (2001) 331.

[7] M. M. Doeff, T.-J. Richardson, J. Hollingsworth, C.-W. Yuan, M. Gonzales, *J. Power Sources*. **112** (2002) 294.

[8] M. M. Doeff, T. J. Richardson, K.-T. Hwang, *J. Power Sources*. **135** (2004), 240.

[9] J. Akimoto, Y. Takahashi, Y. Gotoh, K. Kawaguchi, K. Dokko, I. Uchida, *Chem. Mater*. **15** (2003), 2984.

[10] J. Akimoto, Y. Takahashi, N. Kijima, Y. Gotoh, *Solid State Ionics*. **172** (2004), 491.

[11] Y. Takahashi, J. Akimoto, Y. Gotoh, K. Dokko, M. Nishizawa, I. Uchida, *J. Phys. Soc. Jpn*. **72** (2003) 1483.

[12] J. Akimoto, Y. Takahashi, N. Kijima, *Electrochem. Solid-State Lett*. **8** (2005) A361.

[13] H. Kawai, M. Nagata, H. Tukamoto, A. R. West, *Electrochem. Solid-State Lett*. **1** (1998) 212.

[14] N. Kuwata, S. Kudo, Y. Matsuda, J. Kawamura, *Solid State Ionics*. **262** (2014) 165.

[15] H. Shigemura, M. Tabuchi, H. Kobayashi, H. Sakaebe, A. Hirano, H. Kageyama, *J. Mater. Chem*. **12** (2002) 1882.

[16] J.M. Paulsen, J.R. Dahn, *J. Electrochem. Soc.* **147** (2000) 2478.

[17] C. Delmas, J.-J. Braconnier, A. Maazaz, P. Hagenmuller, *Revue de Chimie Mimerale*, **19** (1982) 343.

Chapter II

Lithium manganese oxide $Li_{0.44+x}MnO_2$

－Estimation of specific capacity by clarifying lithium sites－

Section II-I   Introduction

In recent years, lithium ion secondary batteries (LIBs) are used as small power sources for smartphones and laptop computers. LIBs are also expected to be widely used as large power sources for electric vehicles in future, and their importance has been increasing more and more. LIBs are composed of four parts: positive electrode, negative electrode, separator, and electrolyte. Among these parts, $LiCoO_2$ and $LiNiO_2$ with layered rock-salt type structure and $LiMn_2O_4$ ($Li_{0.5}MnO_2$) with spinel-type structure are considered as positive electrode active materials. Among them, $LiCoO_2$ is superior in electrochemical properties such as operating potential and reversible Li^+ extraction and insertion reaction, so future demand will increase. However, $LiCoO_2$ is expensive because it uses Co which is a rare metal. Since this active material uses Co, which is a rare metal, it is expensive. In addition, 35% of the world's Co production is used in the battery industry. From these facts, only $LiCoO_2$ cannot meet future demand growth. For this reason, lithium transition metal oxides containing Ni and Mn are less expensive than $LiCoO_2$.

$LiNiO_2$ with layered rock-salt type structure has advantages in cost and specific capacity, and is being developed as a promising alternative material for $LiCoO_2$. However, LIBs using $LiNiO_2$ as the positive electrode active material have a risk of heat generation, thermal runaway, and fire due to instability of $LiNiO_2$ in the fully charged state, and there are many problems concerning safety. It is a promising active material to use Mn which is less resource-constrained and inexpensive and which can withstand the chemical bond change of Mn-O in the redox reaction of Mn^{3+}/Mn^{4+}. In particular, spinel-type $LiMn_2O_4$ uses Mn, which is less expensive than Co and Ni, and is also practically used because it is excellent in safety in the fully charged state. However, since spinel-type $LiMn_2O_4$ ($Li_{0.5}MnO_2$) has a lower specific capacity than $LiCoO_2$ and $LiNiO_2$, this active material is less widespread than expected.

Research on tunnel-type $Li_{0.44}MnO_2$ prepared by ion exchange method using $Na_{0.44}MnO_2$ as a starting material has also been reported [1-8]. Such a method of preparing using ion exchange or phase transition is called soft chemical method. The crystal structure of $Li_{0.44}MnO_2$ (Fig. 1-1) consists of double and triple rutile-type chains of edge-sharing MnO_6 octahedra and a single chain of edge-sharing MnO_5 that share vertices to produce a framework containing large tunnels along the c-axis. Hence, this compound does not undergo a conversion to spinel structure during normal cycling or upon heating below approximately 400 °C [7]. However, since the reported $Li_{0.44}MnO_2$ has a small Li content of 0.44, the charge capacity is about 100 mAh g^{-1}. For this reason, it has not reached a practical level and improvement of capacity is required [1,2]. Recently, the specific capacity and discharge profile were improved by an additional Li insertion treatment in molten $LiNO_3$-LiOH salt at low temperature [7,8]. The obtained $Li_{0.55}MnO_2$ sample exhibited the initial charge capacity of about 150 mAh g^{-1} with the average discharge voltage of 3.7 V vs. Li/Li$^+$. In addition, a further chemical lithiation treatment using LiI was performed to increase the Li content in the $Li_{0.82}MnO_2$ sample [8]. The obtained $Li_{0.82}MnO_2$ sample exhibited the initial charge capacity of about 210 mAh g^{-1} between 4.8 and 2.5 V vs. Li/Li$^+$ with a fixed current density of 10 mA g^{-1} at 25 °C. However, the structural details of $Li_{0.44+x}MnO_2$, especially the Li site positions, have not been revealed yet, to our knowledge. By revealing the Li site positions, it is possible to estimate the maximum specific capacity of the crystal structure.

In the present research, we have successfully determined the precise positions of the Li atoms in $Li_{0.44+x}MnO_2$ for the first time.

Section II-II   Experiment

II-II-I   Synthesis

   Tunnel-type $Li_{0.44+x}MnO_2$ was prepared by the synthetic reported route using $Na_{0.44}MnO_2$ as the starting material [1-8]. First, tunnel-type $Na_{0.44}MnO_2$ was synthesized by mixing Na_2CO_3 (99% pure) and Mn_2O_3 (99.9% pure) at a molar ratio of 1:2 at 900 °C for 12 h in air. The molar ratio of Na / Mn= 0.5 was required to prevent loss of the sodium component by volatilization. Next, tunnel-type $Li_{0.44}MnO_2$ was prepared from $Na_{0.44}MnO_2$ via Na/Li ion-exchange reaction using $LiNO_3$ molten salt at 270 ° C for 10 h in air [6-8]. After ion-exchanged, the reaction mixture was washed with distilled water and ethanol, and then dried at room temperature. Further, tunnel-type $Li_{0.55}MnO_2$ was prepared by adding the obtained $Li_{0.44}MnO_2$ to the molten salt of $LiOH-LiNO_3$ at 270 °C for 10 h. This process is important to improve the discharge capacity in the 4 V plateau region, as previously reported [7,8]. The resulting reaction mixture was washed with distilled water and ethanol, and dried in an oven at 60 ° C. Finally, $Li_{0.77}MnO_2$ and $Li_{0.82}MnO_2$ were prepared by adding $Li_{0.55}MnO_2$ to a solution of 10 mol% excess of LiI as a reducing agent in acetonitrile and refluxing at 80 °C for 5 h and 10 h, respectively. After the reaction, the obtained samples were washed with acetonitrile and then dried in vacuum at 120 °C for 12 h [8].

II-II-II   Crystal structure analysis

   Rietveld analysis was performed on the obtained powder sample by powder X-ray diffraction measurement data. Rietveld analysis is a technique for refining the crystal structure of the entire powder X-ray and neutron diffraction patterns. It is a method to obtain a reasonable crystal structure model by decreasing the difference between the diffraction profiles of the observed and that of the assumed crystal structure model by the least squares method. R factor is a reliability factor for estimating the degree of coincidence between diffraction intensity and calculated intensity of Rietveld analysis.

   In order to determine the crystal structure, refinements by Rietveld analysis using powder synchrotron X-ray diffraction (XRD) and neutron diffraction (ND) data were performed. Synchrotron X-ray experiments were carried out in BL19B2 at SPring-8 (Sayo-gun, Hyogo, Japan). The powder samples were sealed in a Lindeman glass capillary with 0.3 mm diameter. The incident X-ray wavelength was 0.49996 Å, and exposure time was 15–20 min. Synchrotron powder XRD data were collected in steps of 0.01° over a 2θ range of 4–75°. ND experiments were carried out at room temperature with wavelength $\lambda = 1.8024$ Å using a HERMES diffractometer (JAEA, JRR3M beamlineT1–3). The ND data were collected in steps of 0.05° over a 2θ range of 7–157°. Rietveld analysis was performed using Jana2006 [9]. The crystal structure of $Li_{0.44+x}MnO_2$ was estimated with electron diffraction pattern by transmission electron microscopy (TEM by HITACHI H-800) to possible of superstructures. X-ray absorption fine structure spectroscopy (XAFS) at Mn-*K* edges was carried out in BL-9C at Photon Factory in High Energy Accelerator Research Organization (Tsukuba, Ibaraki, Japan). The Athena software was used for the analysis of XAFS data.

II-II-III   ICP emission spectroscopic analysis

For the obtained sample, elemental analysis of Na, Li, Mn was performed using Inductively

Coupled Plasma Atomic Emission Spectroscopy (ICP-AES by HITACHI P-4010).

II-II-IV   Electrochemical measurement

  Electrochemical measurements were performed using coin-type cells (CR2032). Working electrodes were prepared using 5 mg of active materials, 5 mg of acetylene black as the conductive agent, and 1 mg of polyvinylidene difluoride as the binder. An Al mesh was used as the current collector, and the electrode diameter was 15 mm. A circular Li foil, having a diameter of 15 mm and a thickness of 0.2 mm, was used as the counter electrode. A microporous polypropylene sheet was used as the separator. A 1 M $LiPF_6$ solution in a 1:1 (v/v) mixture of ethylene carbonate and diethyl carbonate was used as the electrolyte. Cells were constructed in an argon-filled grove box. Electrochemical measurements were conducted with a current density of 10 mA g^{-1} at 25 °C after standing overnight under open-circuit conditions. The cell was first charged to 4.8 V, and then kept at 4.8 V for 4h. The cell was discharge charged to 2.5 V at same current density.

Section II-III Results and Discussion

II-III-I Crystal structure analysis of $Na_{0.44}MnO_2$

Figure 2-3-1-1 shows the diffraction pattern of $Na_{0.44}MnO_2$ by powder synchrotron radiation XRD measurement and the results of the fitting by Jana2006 program using the previous report as the initial crystal structure model [10]. The diffraction pattern was identified to be single phase with an orthorhombic crystal system and space group *Pbam*. The orthorhombic lattice parameters for $Na_{0.44}MnO_2$ were refined to be $a = 9.10657$ (8) Å, $b = 26.4292$ (2) Å, $c = 2.828802$ (7) Å, and $Z = 18$. The lattice parameters of $Na_{0.44}MnO_2$ were similar to the reported values [10]. The resultant R values of $Na_{0.44}MnO_2$ reached $R_{wp} = 4.92$ % and $R_p = 3.71$ %, with a fit indicator of $S = R_{wp}/R_e = 1.33$.
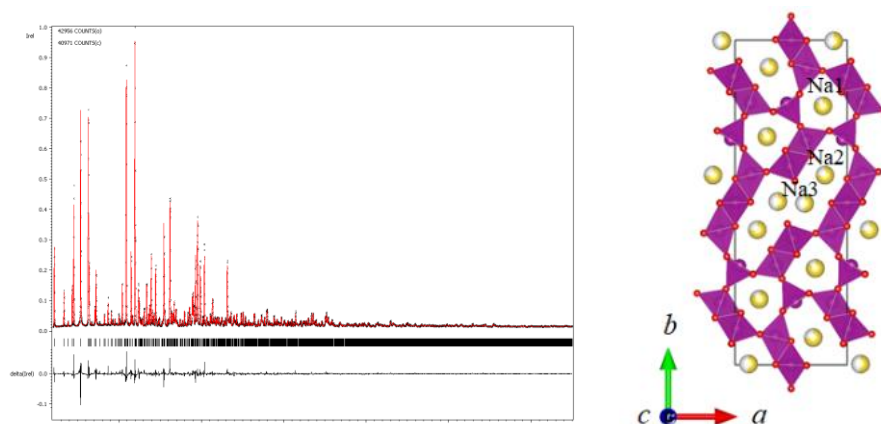

Figure 2-3-1-1 Observed, calculated, and difference pattern for the Rietveld refinement using the powder synchrotron radiation XRD data of $Na_{0.44}MnO_2$. The short vertical lines below the profiles mark positions of all position Bragg reflections of $Na_{0.44}MnO_2$. A schematic illustration of tunnel-type $Na_{0.44}MnO_2$ is also shown.

Table 2-3-1-1 summarizes the atomic coordinates of $Na_{0.44}MnO_2$. The chemical composition was estimated to be $Na_{0.47}MnO_2$ from the refinement of the crystal structure. The crystal structure of $Na_{0.44}MnO_2$ projected down to the *c*-axis direction is shown in Fig. 2-3-1-1. The framework structure consists of double and triple rutile-type chains of edge-sharing MnO_6 octahedra and a single chain of edge-sharing MnO_5.

Table 2-3-1-1. Structural parameters of $Na_{0.44}MnO_2$ determined by Rietveld analysis using synchrotron powder XRD data.

atom	Site	x / a	y / b	z / c	occupancy	U_{eq} / Å^2
Na1	4g	0.21594	0.20263	0	0.850	0.045
Na2	4h	0.69762	0.08410	1/2	0.743	0.051
Na3	4g	0.11988	0.00289	0	0.521	0.022
Mn1	4h	0.86482	0.19276	1/2	1.00	0.001
Mn2	2c	1/2	0	0	1.00	0.001
Mn3	4g	0.53846	0.19478	0	1.00	0.001
Mn4	4h	0.3593	0.08851	1/2	1.00	0.001

Mn5	4g	0.01685	0.11052	0	1.00	0.001
O1	4h	0.9661	0.06546	1/2	1.00	0.004
O2	4g	0.91835	0.23432	0	1.00	0.004
O3	4h	0.05077	0.15985	1/2	1.00	0.004
O4	4g	0.49915	0.07300	0	1.00	0.004
O5	4g	0.21915	0.09459	0	1.00	0.004
O6	4h	0.36136	0.00153	1/2	1.00	0.004
O7	4h	0.42524	0.16635	1/2	1.00	0.004
O8	4h	0.66021	0.22049	1/2	1.00	0.004
O9	4g	0.82172	0.14516	1/2	1.00	0.004

Table 2-3-1-2 summarizes the selected bond distances for $Na_{0.44}MnO_2$. The bond valence analysis using the individual Mn-O distance revealed that the calculated valence states were +3.9 for the Mn1 site, +4.0 for the Mn2 site, +3.0 for the Mn3 site, +3.1 for the Mn4 site, and +3.7 for the Mn5 site. These results suggested the manganese valence Mn^{3+}/Mn^{4+} ordering in $Na_{0.44}MnO_2$. Three types of Na sites located in the tunnel space. The Na-O coordination polyhedra were mono-capped trigonal prism for the Na1 site, distorted trigonal prism for the Na2 site, and mono-capped trigonal prism for the Na3 site (Table 2-3-1-2).

Table 2-3-1-2. Selected Bond Distances (Å) for $Na_{0.44}MnO_2$

Na1	O3	× 2	2.3540	Mn1	O2	× 2	1.8560
	O2	× 1	2.4848		O3	× 1	1.9037
	O8	× 2	2.5272		O9	× 2	1.9332
	O7	× 2	2.5598		O1	× 1	2.0023
Na2	O4	× 2	2.3138	Mn2	O6	× 4	1.8964
	O6	× 1	2.3260		O4	× 2	1.9292
	O9	× 2	2.4252				
	O1	× 1	2.4941				
Na3	O1	× 2	2.4243	Mn3	O7	× 2	1.9047
	O5	× 1	2.5867		O8	× 2	1.9213
	O1	× 2	2.5877		O2	× 1	2.1697
	O6	× 2	2.6148				
				Mn4	O5	× 2	1.9118
					O4	× 2	1.9470
					O7	× 1	2.1431
					O6	× 1	2.2990
				Mn5	O5	× 1	1.8898
					O4	× 2	1.9060

O7	× 2	1.9481
O6	× 1	1.9988

II-III-II Crystal structure analysis of $Li_{0.44}MnO_2$

  Figure 2-3-2-1 shows the diffraction pattern of $Li_{0.44}MnO_2$ by powder synchrotron radiation XRD measurement and the results of the fitting by Jana2006 program using the framework of tunnel-type $Na_{0.44}MnO_2$ obtained in Fig. 2-3-1-1 as the initial crystal structure model. The diffraction pattern was identified to be single phase with an orthorhombic crystal system and space group *Pbam*. The orthorhombic lattice parameters for $Li_{0.44}MnO_2$ were refined to be $a = 8.9243 (1)$ Å, $b = 24.2568 (4)$ Å, $c = 2.82927 (4)$ Å, and $Z = 18$. The lattice parameters of $Li_{0.44}MnO_2$ were similar to the reported values [6,8]. $Li_{0.44}MnO_2$ kept the tunnel structure, and the a and b axis lengths were shorter than $Na_{0.44}MnO_2$. This was presumed to be due to the difference in ionic radius between Na^+ (1.02 Å) and Li^+ (0.76 Å) [11]. The resultant R values of $Li_{0.44}MnO_2$ reached $R_{wp} = 7.69$ % and $R_p = 5.60$ %, with a fit indicator of $S = R_{wp}/R_e = 1.37$. Refinement of the Li sites was attempted, but it was unknown even by difference Fourier synthesis.
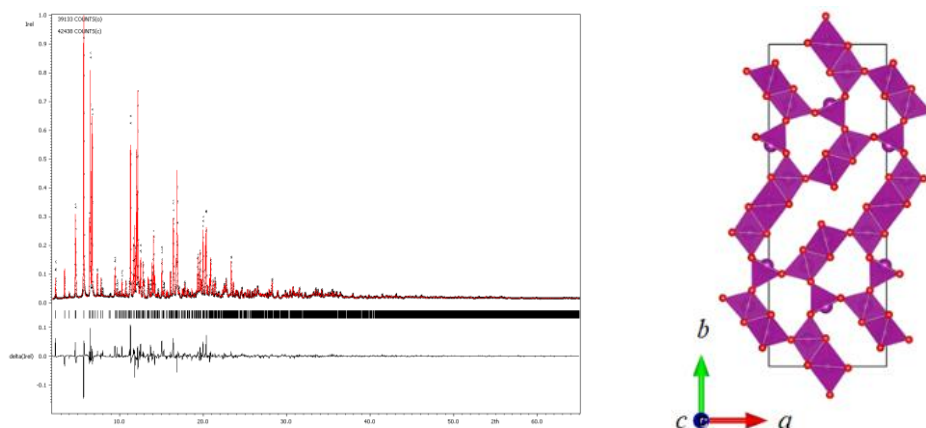

Figure 2-3-2-1 Observed, calculated, and difference pattern for the Rietveld refinement using the powder synchrotron radiation XRD data of $Li_{0.44}MnO_2$. The short vertical lines below the profiles mark positions of all position Bragg reflections of $Li_{0.44}MnO_2$. A schematic illustration of tunnel-type $Li_{0.44}MnO_2$ is also shown.

  Next, the result of powder ND measurement to determine the Li sites of $Li_{0.44}MnO_2$, which was unknown is shown in Fig. 2-3-2-1. Rietveld analysis was performed using the framework obtained in Fig. 2-3-2-1 as the initial crystal structure model. The Li sites were refined using difference Fourier synthesis [12]. Figure 2-3-2-2 shows the diffraction pattern of $Li_{0.44}MnO_2$ by powder ND measurement and the results of the fitting by Jana2006 program. The diffraction pattern was identified to be single phase with an orthorhombic crystal system and space group *Pbam*. The orthorhombic lattice parameters for $Li_{0.44}MnO_2$ were refined to be $a = 8.92515 (8)$ Å, $b = 24.2590 (3)$ Å, $c = 2.82908 (2)$ Å, and $Z = 18$. The resultant R values of $Li_{0.44}MnO_2$ reached $R_{wp} = 10.29$ % and $R_p = 4.50$ %, with a fit indicator of $S = R_{wp}/R_e = 2.29$.

  Table 2-3-2-1 summarizes the atomic coordinates of $Li_{0.44}MnO_2$. The chemical composition was estimated to be $Li_{0.420}MnO_2$ from the refinement of the crystal structure, which was almost consistent with the result of ICP-AES. The crystal structure of $Li_{0.44}MnO_2$ projected down to the c-axis direction is shown in Fig. 2-3-2-2. The Li site of $Li_{0.44}MnO_2$ was found for the first time to occupy a site different from the Na site of $Na_{0.44}MnO_2$ as the starting material.
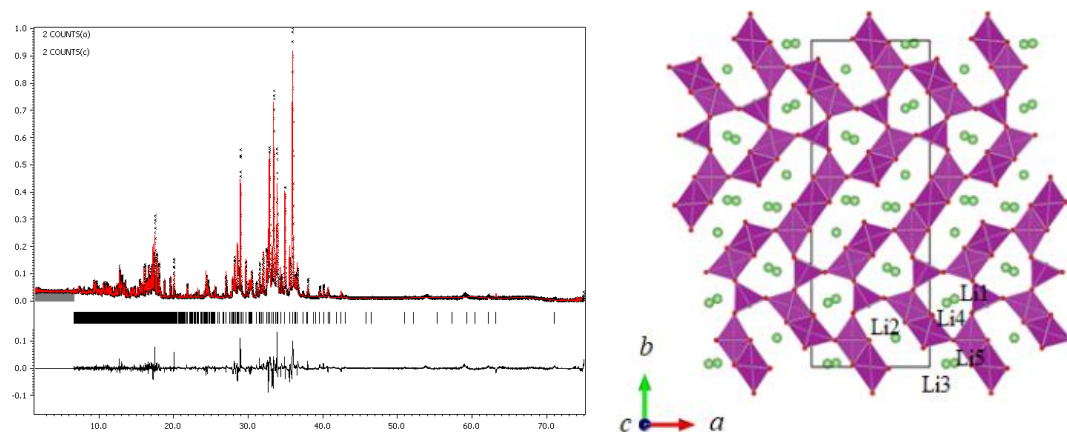
Figure 2-3-2-2 Observed, calculated, and difference pattern for the Rietveld refinement using the powder ND data of $Li_{0.44}MnO_2$. The short vertical lines below the profiles mark positions of all position Bragg reflections of $Li_{0.44}MnO_2$. A schematic illustration of tunnel-type $Li_{0.44}MnO_2$ is also shown.

Table 2-3-2-1. Structural parameters of $Li_{0.44}MnO_2$ determined by Rietveld analysis using powder ND data.

atom	Site	x/a	y/b	z/c	occupancy	U_{eq} / Å^2
Li1	4h	0.208	0.208	1/2	0.35	0.030
Li2	4h	0.210	0.412	1/2	0.39	0.030
Li3	4h	0.365	0.509	1/2	0.33	0.030
Li4	4g	0.139	0.196	0	0.52	0.030
Li5	4g	0.292	0.511	0	0.31	0.030
Mn1	4g	−0.01998	0.31271	0	1.00	0.004
Mn2	4h	0.33448	0.08192	1/2	1.00	0.004
Mn3	2c	0	1/2	0	1.00	0.004
Mn4	4h	0.32079	0.31286	−1/2	1.00	0.004
Mn5	4g	−0.00646	0.10522	0	1.00	0.004
O1	4h	0.34721	0.00572	1/2	1.00	0.007
O2	4g	0.19540	0.08171	0	1.00	0.007
O3	4h	0.01785	0.15835	1/2	1.00	0.007
O4	4h	0.35258	0.16586	1/2	1.00	0.007
O5	4h	0.11389	0.29159	1/2	1.00	0.007
O6	4g	0.35747	0.26323	0	1.00	0.007
O7	4g	0.28589	0.36455	0	1.00	0.007
O8	4g	0.48283	0.08209	0	1.00	0.007
O9	4h	0.44350	0.44162	1/2	1.00	0.007

Table 2-3-2-2 summarizes the selected bond distances for $Li_{0.44}MnO_2$. The bond valence analysis using the individual Mn-O distance revealed that the calculated valence states were +3.1 for the Mn1 site, +3.8 for the Mn2 site, +3.3 for the Mn3 site, +4.0 for the Mn4 site, and

16

+3.9 for the Mn5 site. The average valence state of Mn was hardly changed, as compared with $Na_{0.44}MnO_2$. These results suggested the manganese valence Mn^{3+}/Mn^{4+} ordering in $Li_{0.44}MnO_2$. A similar valence ordering was reported in spinel-type $LiMn_2O_4$ [13]. Five types of Li sites located in the tunnel space. The Li-O coordination polyhedra were distorted trigonal bipyramid for the Li1 site, distorted trigonal prism for the Li2 site, trigonal bipyramid for the Li3 site, distorted square pyramid for the Li4 site, and distorted square pyramid for the Li5 site (Table 2-3-2-2). The average valence state of Li was hardly changed, as compared with $Na_{0.44}MnO_2$.

Table 2-3-2-2. Selected Bond Distances (Å) for $Li_{0.44}MnO_2$

Li1	O4	× 1	1.6463	Mn1	O4	× 2	1.8881
	O3	× 1	2.0811		O5	× 2	1.9212
	O5	× 1	2.1948		O6	× 1	2.1425
	O6	× 2	2.3613				
Li2	O7	× 2	1.9454	Mn2	O1	× 1	1.8520
	O9	× 1	2.2044		O2	× 2	1.8819
	O1	× 1	2.3302		O8	× 2	1.9375
	O8	× 2	2.4764		O4	× 1	2.0427
Li3	O9	× 1	1.7784	Mn3	O1	× 4	1.9697
	O1	× 1	1.8957		O8	× 2	1.9974
	O9	× 1	2.0872				
	O2	× 2	2.3244				
Li4	O3	× 2	2.0011	Mn4	O6	× 2	1.8862
	O4	× 2	2.4838		O3	× 1	1.8923
	O6	× 1	2.5421		O7	× 2	1.9158
					O5	× 1	1.9175
Li5	O2	× 1	1.7191	Mn5	O9	× 2	1.8685
	O1	× 2	1.8871		O2	× 1	1.8897
	O9	× 2	2.5811		O3	× 2	1.9260
					O7	× 1	1.9931

II-III-III   Crystal structure analysis of $Li_{0.55}MnO_2$

  Figure 2-3-3-1 shows the diffraction pattern of $Li_{0.55}MnO_2$ by powder ND measurement and the results of the fitting by Jana2006 program using tunnel-type $Li_{0.44}MnO_2$ obtained in Fig. 2-3-2-2 as the initial crystal structure model. The diffraction pattern was identified to be single phase with an orthorhombic crystal system and space group *Pbam*. The orthorhombic lattice parameters for $Li_{0.55}MnO_2$ were refined to be a = 8.8782 (2) Å, b = 24.2490 (7) Å, c = 2.82239 (9) Å, and Z = 18. The lattice parameters of $Li_{0.55}MnO_2$ were similar to the reported values [8]. The resultant R values of $Li_{0.55}MnO_2$ reached R_{wp} = 5.76 % and R_p = 4.37 %, with a fit indicator of $S = R_{wp}/R_e$ = 1.32.

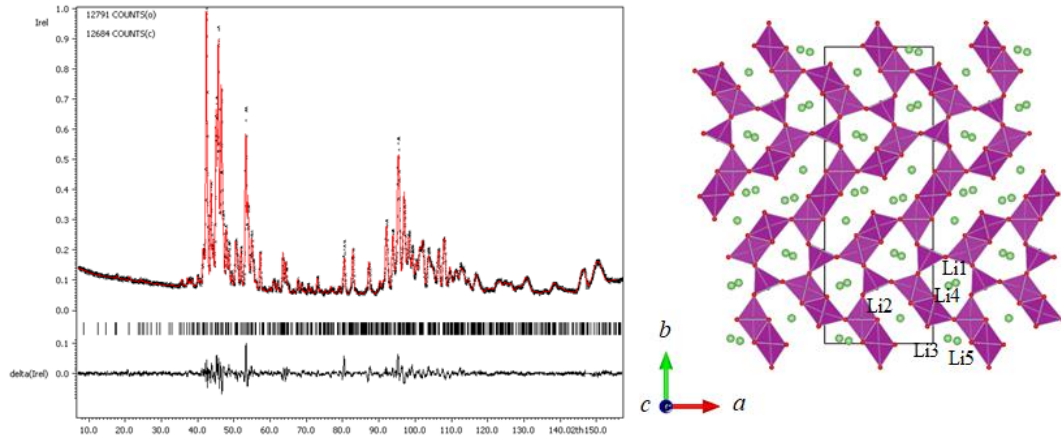Figure 2-3-3-1 Observed, calculated, and difference pattern for the Rietveld refinement using the powder ND data of $Li_{0.55}MnO_2$. The short vertical lines below the profiles mark positions of all position Bragg reflections of $Li_{0.55}MnO_2$. A schematic illustration of tunnel-type $Li_{0.55}MnO_2$ is also shown.

  Table 2-3-3-1 summarizes the atomic coordinates of $Li_{0.55}MnO_2$. The chemical composition was estimated to be $Li_{0.520}MnO_2$ from the refinement of the crystal structure, which was almost consistent with the result of ICP-AES. The crystal structure of $Li_{0.55}MnO_2$ projected down to the *c*-axis direction is shown in Fig. 2-3-3-1. Occupancy rate (OCC) in the Li sites of $Li_{0.55}MnO_2$ was increased, as compared with $Li_{0.44}MnO_2$. The increased 0.11 amount of Li was inserted into the same Li sites as $Li_{0.44}MnO_2$.

Table 2-3-3-1. Structural parameters of $Li_{0.55}MnO_2$ determined by Rietveld analysis using powder ND data.

atom	Site	x/a	y/b	z/c	occupancy	U_{eq} / Å^2
Li1	4*h*	0.20879	0.20495	1/2	0.4534	0.0248
Li2	4*h*	0.19674	0.41465	1/2	0.5478	0.0248
Li3	4*h*	0.36494	0.51732	1/2	0.5709	0.0248
Li4	4*g*	0.14214	0.19513	0	0.5384	0.0248
Li5	4*g*	0.27809	0.50933	0	0.2290	0.0248
Mn1	4*g*	−0.01891	0.31361	0	1.00	0.0048

Mn2	4h	0.33925	0.08429	1/2	1.00	0.0048
Mn3	2c	0	1/2	0	1.00	0.0048
Mn4	4h	0.32305	0.31179	−1/2	1.00	0.0048
Mn5	4g	−0.00718	0.10373	0	1.00	0.0048
O1	4h	0.35231	0.00394	1/2	1.00	0.0086
O2	4g	0.19346	0.08087	0	1.00	0.0086
O3	4h	0.02040	0.15748	1/2	1.00	0.0086
O4	4h	0.35138	0.16445	1/2	1.00	0.0086
O5	4h	0.11431	0.29159	1/2	1.00	0.0086
O6	4g	0.36055	0.26295	0	1.00	0.0086
O7	4g	0.29256	0.36444	0	1.00	0.0086
O8	4g	0.48732	0.08037	0	1.00	0.0086
O9	4h	0.44610	0.44180	1/2	1.00	0.0086

Table 2-3-3-2 summarizes the selected bond distances for $Li_{0.55}MnO_2$. The bond valence analysis using the individual Mn-O distance revealed that the calculated valence states were +3.0 for the Mn1 site, +3.7 for the Mn2 site, +3.7 for the Mn3 site, +4.0 for the Mn4 site, and +4.1 for the Mn5 site. The average valence state of Mn in $Li_{0.55}MnO_2$ increased despite the Li insertion treatment, as compared with $Li_{0.44}MnO_2$. This may be because trivalent manganese has absorbed oxygen in order to treat the Li insertion near 300 °C [14]. On the other hand, the average Li-O distance in the five types of $Li_{0.55}MnO_2$ was hardly changed as compared with $Li_{0.44}MnO_2$.

Table 2-3-3-2. Selected Bond Distances (Å) for $Li_{0.55}MnO_2$

Li1	O4	× 1	1.6022	Mn1	O4	× 2	1.8975
	O3	× 1	2.0304		O5	× 2	1.9171
	O5	× 1	2.2622		O6	× 1	2.1429
	O6	× 2	2.4052				
Li2	O7	× 2	2.0489	Mn2	O1	× 1	1.9520
	O9	× 1	2.3097		O2	× 2	1.9167
	O1	× 1	2.2085		O8	× 2	1.9310
	O8	× 2	2.3373		O4	× 1	1.9467
Li3	O9	× 1	1.9485	Mn3	O1	× 4	1.9287
	O1	× 1	1.9559		O8	× 2	1.9522
	O9	× 1	1.9679				
	O2	× 2	2.1529				
Li4	O3	× 2	1.9984	Mn4	O6	× 2	1.8722
	O4	× 2	2.4486		O3	× 1	1.9040
	O6	× 1	2.5425		O7	× 2	1.9221

					O5	× 1	1.9169
Li5	O2	× 1	1.7531	Mn5	O9	× 2	1.8391
	O1	× 2	1.8300		O2	× 1	1.8656
	O9	× 2	2.6264		O3	× 2	1.9366
					O7	× 1	1.9383

II-III-IV   Crystal structure analysis of $Li_{0.77}MnO_2$

Figure 2-3-4-1 shows the diffraction pattern of $Li_{0.77}MnO_2$ by powder neutron diffraction measurement and the results of the fitting by Jana2006 program using tunnel-type $Li_{0.55}MnO_2$ obtained in Fig. 2-3-3-1 as the initial crystal structure model and the Li sites were refined using difference Fourier synthesis. The diffraction pattern was identified to be single phase with an orthorhombic crystal system and space group *Pbam*. The orthorhombic lattice parameters were refined to be a = 8.8860 (1) Å, b = 24.3930 (3) Å, c = 2.82918 (2) Å, and Z = 18. The resultant R values of $Li_{0.77}MnO_2$ reached R_{wp} = 9.29 % and R_p = 4.31 %, with a fit indicator of $S = R_{wp}/R_e$ = 2.16.
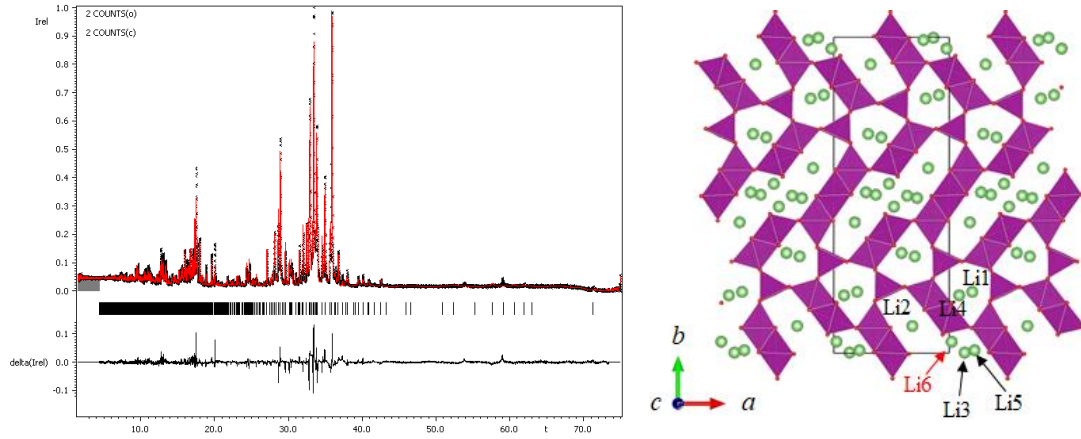
Figure 2-3-4-1 Observed, calculated, and difference pattern for the Rietveld refinement using the powder ND data of $Li_{0.77}MnO_2$. The short vertical lines below the profiles mark positions of all position Bragg reflections of $Li_{0.77}MnO_2$. A schematic illustration of tunnel-type $Li_{0.77}MnO_2$ is also shown.

Table 2-3-4-1 summarizes the atomic coordinates of $Li_{0.77}MnO_2$. The chemical composition was estimated to be $Li_{0.744}MnO_2$ from the refinement of the crystal structure, which was almost consistent with the result of ICP-AES. The crystal structure of $Li_{0.77}MnO_2$ projected down to the *c*-axis direction is shown in Fig. 2-3-4-1. $Li_{0.77}MnO_2$ was found for the first time that a new lithium (Li6) site was added, as compared with $Li_{0.55}MnO_2$.

Table 2-3-4-1. Structural parameters of $Li_{0.77}MnO_2$ determined by Rietveld analysis using powder ND data.

atom	Site	x/a	y/b	z/c	occupancy	U_{eq} / Å^2
Li1	4h	0.20204	0.19387	1/2	0.550	0.0690
Li2	4h	0.18126	0.41409	1/2	0.683	0.0690
Li3	4h	0.3641	0.50159	1/2	0.560	0.0690
Li4	4g	0.08788	0.18294	0	0.513	0.0690
Li5	4g	0.2780	0.5090	0	0.520	0.0690
Li6	4g	0.4780	0.5361	0	0.520	0.0690
Mn1	4g	−0.01284	0.31269	0	1.00	0.0048

Mn2	4h	0.34026	0.08405	1/2	1.00	0.0048
Mn3	2c	0	1/2	0	1.00	0.0048
Mn4	4h	0.32288	0.30856	−1/2	1.00	0.0048
Mn5	4g	−0.00888	0.10519	0	1.00	0.0048
O1	4h	0.35231	0.00394	1/2	1.00	0.0086
O2	4g	0.19310	0.08020	0	1.00	0.0086
O3	4h	0.02324	0.15899	1/2	1.00	0.0086
O4	4h	0.35631	0.16547	1/2	1.00	0.0086
O5	4h	0.11212	0.29007	1/2	1.00	0.0086
O6	4g	0.35954	0.26368	0	1.00	0.0086
O7	4g	0.28509	0.36325	0	1.00	0.0086
O8	4g	0.49075	0.08037	0	1.00	0.0086
O9	4h	0.44472	0.44108	1/2	1.00	0.0086

Table 2-3-4-2 summarizes the selected bond distances for $Li_{0.77}MnO_2$. The bond valence analysis using the individual Mn-O distance revealed that the calculated valence states were +3.1 for the Mn1 site, +3.5 for the Mn2 site, +3.5 for the Mn3 site, +4.0 for the Mn4 site, and +3.9 for the Mn5 site. The average valence state of Mn in $Li_{0.77}MnO_2$ decreased with the additional Li insertion treatment, as compared with $Li_{0.55}MnO_2$. Six types of Li sites located in the tunnel space. The Li-O coordination polyhedra were distorted trigonal bipyramid for the Li1 site, distorted trigonal prism for the Li2 site, trigonal bipyramid for the Li3 site, distorted octahedron for the Li4 site, distorted square pyramid for the Li5 site, and distorted square pyramid for the Li6 site (Table 2-3-4-2). However, the average valence state of Li was increased, as compared with $Li_{0.55}MnO_2$.

Table 2-3-4-2. Selected Bond Distances (Å) for $Li_{0.77}MnO_2$

Li1	O4	× 1	1.5360	Mn1	O4	× 2	1.9071
	O3	× 1	1.8024		O5	× 2	1.8811
	O5	× 1	2.4788		O6	× 1	2.1809
	O6	× 2	2.6190				
Li2	O7	× 2	2.0952	Mn2	O1	× 1	1.9868
	O9	× 1	2.4316		O2	× 2	1.9287
	O1	× 1	2.1759		O8	× 2	1.9487
	O8	× 2	2.2102		O4	× 1	1.9911
Li3	O9	× 1	1.6417	Mn3	O1	× 4	1.9566
	O1	× 1	1.8854		O8	× 2	1.9623
	O9	× 1	2.2012				
	O2	× 2	2.4366				
Li4	O3	× 2	1.6348	Mn4	O6	× 2	1.8181

	O4	× 2	2.8058		O3	× 1	1.9485
	O6	× 1	2.4108		O7	× 2	1.9732
	O2	× 1	2.6749		O5	× 1	1.9264
Li5	O2	× 1	1.7558	Mn5	O9	× 2	1.8554
	O1	× 2	1.8110		O2	× 1	1.8954
	O9	× 2	2.6353		O3	× 2	1.9505
					O7	× 1	1.9861
Li6	O9	× 2	1.6685				
	O2	× 1	1.8625				
	O9	× 2	2.7325				

II-III-V   Crystal structure analysis of $Li_{0.82}MnO_2$

Figure 2-3-5-1 shows the diffraction pattern of $Li_{0.82}MnO_2$ by powder ND measurement and the results of the fitting by Jana2006 program using tunnel-type $Li_{0.77}MnO_2$ obtained in Fig. 2-3-4-1 as the initial crystal structure model. The diffraction pattern was identified with an orthorhombic crystal system and space group *Pbam*. Diffraction peaks of Li_2CO_3 were observed as an impurity phase. The orthorhombic lattice parameters were refined to be $a = 8.8998$ (2) Å, $b = 24.5827$ (5) Å, $c = 2.83125$ (5) Å, and $Z = 18$. The resultant R values of $Li_{0.82}MnO_2$ reached $R_{wp} = 12.29$ % and $R_p = 6.50$ %, with a fit indicator of $S = R_{wp}/R_e = 1.89$.
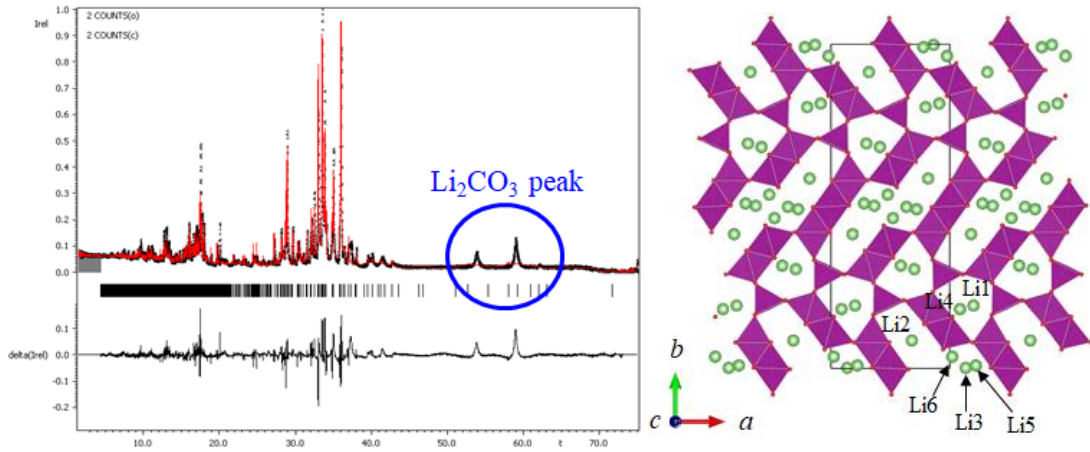
Figure 2-3-5-1 Observed, calculated, and difference pattern for the Rietveld refinement using the powder ND data of $Li_{0.82}MnO_2$. The short vertical lines below the profiles mark positions of all position Bragg reflections of $Li_{0.82}MnO_2$. A schematic illustration of tunnel-type $Li_{0.82}MnO_2$ is also shown.

Table 2-3-5-1 summarizes the atomic coordinates of $Li_{0.82}MnO_2$. The chemical composition was estimated to be $Li_{0.784}MnO_2$ from the refinement of the crystal structure, which was almost consistent with the result of ICP-AES. In this tunnel structure, the maximum lithium amount is estimated in the vicinity of $Li_{0.80}MnO_2$ due to the limit of the crystal structure. The crystal structure of $Li_{0.82}MnO_2$ projected down to the c-axis direction is shown in Fig. 2-3-5-1. Occupancy rate (OCC) in the Li sites of $Li_{0.82}MnO_2$ was increased, as compared with $Li_{0.77}MnO_2$. The increased 0.05 amount of Li was inserted into the same Li sites as $Li_{0.77}MnO_2$.

Table 2-3-5-1. Structural parameters of $Li_{0.82}MnO_2$ determined by Rietveld analysis using powder ND data.

atom	Site	x/a	y/b	z/c	occupancy	$U_{eq}/$ Å^2
Li1	4h	0.20204	0.19387	1/2	0.590	0.0690
Li2	4h	0.18126	0.41409	1/2	0.703	0.0690
Li3	4h	0.3641	0.50159	1/2	0.640	0.0690
Li4	4g	0.08788	0.18294	0	0.513	0.0690
Li5	4g	0.2780	0.5090	0	0.560	0.0690
Li6	4g	0.4780	0.5361	0	0.520	0.0690

Mn1	4g	−0.01284	0.31269	0	1.00	0.0048
Mn2	4h	0.34026	0.08405	1/2	1.00	0.0048
Mn3	2c	0	1/2	0	1.00	0.0048
Mn4	4h	0.32288	0.30856	−1/2	1.00	0.0048
Mn5	4g	−0.00888	0.10519	0	1.00	0.0048
O1	4h	0.34806	0.00265	1/2	1.00	0.0086
O2	4g	0.19310	0.08020	0	1.00	0.0086
O3	4h	0.02324	0.15899	1/2	1.00	0.0086
O4	4h	0.35631	0.16547	1/2	1.00	0.0086
O5	4h	0.11212	0.29007	1/2	1.00	0.0086
O6	4g	0.35954	0.26368	0	1.00	0.0086
O7	4g	0.28509	0.36325	0	1.00	0.0086
O8	4g	0.49075	0.08037	0	1.00	0.0086
O9	4h	0.44472	0.44108	1/2	1.00	0.0086

Table 2-3-5-2 summarizes the selected bond distances for $Li_{0.82}MnO_2$. The bond valence analysis using the individual Mn-O distance revealed that the calculated valence states were +3.1 for the Mn1 site, +3.5 for the Mn2 site, +3.5 for the Mn3 site, +4.0 for the Mn4 site, and +3.9 for the Mn5 site. The average valence state of Mn in $Li_{0.82}MnO_2$ slightly decreased with the additional Li insertion treatment, as compared with $Li_{0.77}MnO_2$. On the other hand, the average Li-O distance in the six types of $Li_{0.82}MnO_2$ was hardly changed as compared with $Li_{0.77}MnO_2$.

Table 2-3-5-2. Selected Bond Distances (Å) for $Li_{0.82}MnO_2$

Li1	O4	× 1	1.5403	Mn1	O4	× 2	1.9101
	O3	× 1	1.8077		O5	× 2	1.8841
	O5	× 1	2.4965		O6	× 1	2.1942
	O6	× 2	2.6294				
Li2	O7	× 2	2.1022	Mn2	O1	× 1	2.0022
	O9	× 1	2.4365		O2	× 2	1.9309
	O1	× 1	2.1927		O8	× 2	1.9509
	O8	× 2	2.2129		O4	× 1	2.0066
Li3	O9	× 1	1.6526	Mn3	O1	× 4	1.9588
	O1	× 1	1.8883		O8	× 2	1.9775
	O9	× 1	2.2101				
	O2	× 2	2.4491				
Li4	O3	× 2	1.6376	Mn4	O6	× 2	1.8242
	O4	× 2	2.8100		O3	× 1	1.9535
	O6	× 1	2.4189		O7	× 2	1.9811
	O2	× 1	2.6936		O5	× 1	1.9300

Li5	O2	× 1	1.7692	Mn5	O9	× 2	1.8616
	O1	× 2	1.8130		O2	× 1	1.8996
	O9	× 2	2.6453		O3	× 2	1.9582
					O7	× 1	1.9811
Li6	O9	× 2	1.6712				
	O2	× 1	1.8693				
	O9	× 2	2.7484				

In order to probe the crystal structure of $Li_{0.82}MnO_2$, we take selected area electron diffraction (SAED) patterns of typical plane by TEM. Figure 2-3-5-2 shows SAED patterns. Figure (a), (b), (c), and (d) show the obtained $a*c*$ plane, the simulated $a*c*$ plane, the obtained $b*c*$ plane, and the simulated $b*c*$ plane, respectively. Both Fig. (a) and (c) matched with the simulated SAED patterns of the tunnel structure. Super reflections in the obtained patterns was not observed in both Fig. (a) and (c). Therefore, no change in framework structure due to Li insertion was confirmed.
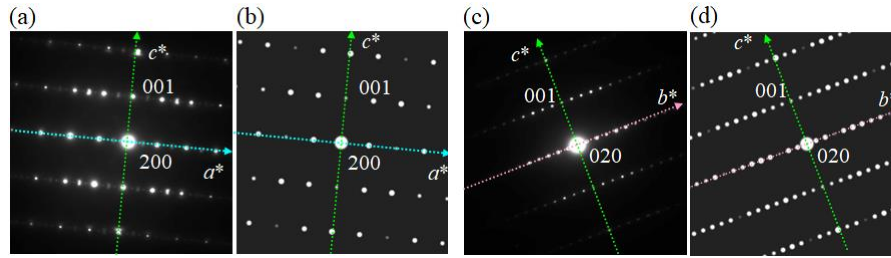
Figure 2-3-5-2. SAED patterns. (a) the obtained $a*c*$ plane, (b) the simulated $a*c*$ plane, (c) the obtained $b*c*$ plane, and (d) the simulated $b*c*$ plane.

Figure 2-3-5-3 shows normalized Mn K-edge X-ray absorption near-edge structure (XANES) spectra of $Li_{0.44}MnO_2$ and $Li_{0.82}MnO_2$. The shift of the main peak, labeled M, is noticed with an assist from the vertical dashed line in Fig. 2-3-5-3. The main peak of $Li_{0.82}MnO_2$ was slightly shifted after Li insertion in $Li_{0.44}MnO_2$. Therefore, the valence of Mn in $Li_{0.82}MnO_2$ is not more than that in $Li_{0.44}MnO_2$ [15]. From this result, it was also confirmed that Li-ions were inserted in the tunnel space.
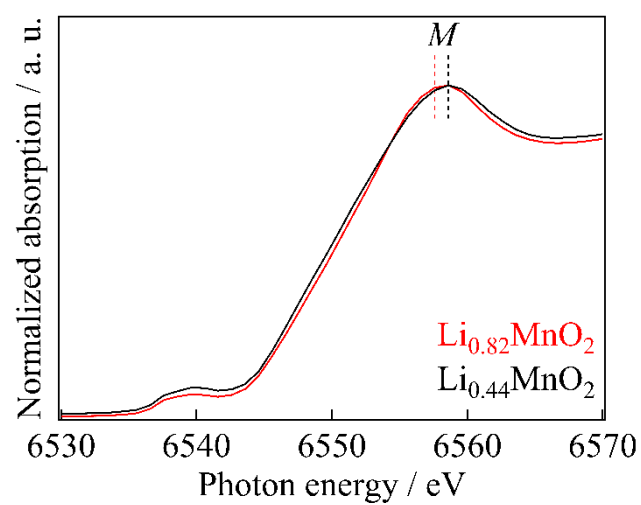
Figure 2-3-5-3. Mn K-edge XANES spectra of $Li_{0.44}MnO_2$ and $Li_{0.82}MnO_2$.

II-III-VI   Electrochemical properties

Figure 2-3-6-1 shows the initial charge and discharge curves for $Li_{0.420}MnO_2$, $Li_{0.520}MnO_2$, $Li_{0.744}MnO_2$, and $Li_{0.784}MnO_2$ in the voltage range between 4.8 and 2.5 V vs Li/Li^+ at a constant current density of 10 mA g^{-1} (C/20) at 25 °C. The initial charge and discharge capacities increased from 88 and 161 mA g^{-1} for $Li_{0.420}MnO_2$ to 136 and 192 mAh g^{-1} for $Li_{0.520}MnO_2$, respectively. In addition, the discharge capacity at the 4 V plateau region in $Li_{0.520}MnO_2$ (about 100 mAh g^{-1}) was increased to twice that in $Li_{0.420}MnO_2$ (about 50 mAh g^{-1}). The initial charge capacity also increased by the additional Li insertion treatment from 136 mAh g^{-1} for $Li_{0.520}MnO_2$ to 180 and 200 mAh g^{-1} for $Li_{0.744}MnO_2$ and $Li_{0.784}MnO_2$, respectively. However, the residual Li_2CO_3 after the additional Li insertion treatment has a slight influence on the electrochemical properties of $Li_{0.784}MnO_2$. Given the limitations of the crystal structure, the maximum capacity of tunnel-type $Li_{0.44+x}MnO_2$ is estimated to be about 200 mAh g^{-1}. On the contrary, the initial discharge curve of $Li_{0.744}MnO_2$ and $Li_{0.784}MnO_2$ remained unchanged from that of $Li_{0.520}MnO_2$. This result suggested that the lithium insertion sites in $Li_{0.744}MnO_2$ and $Li_{0.784}MnO_2$ with tunnel-type $Na_{0.44}MnO_2$ structure remained unchanged from $Li_{0.520}MnO_2$, even after the additional Li insertion treatment. Furthermore, this suggestion was consistent with the increase in OCC at the Li sites in the crystal structure.
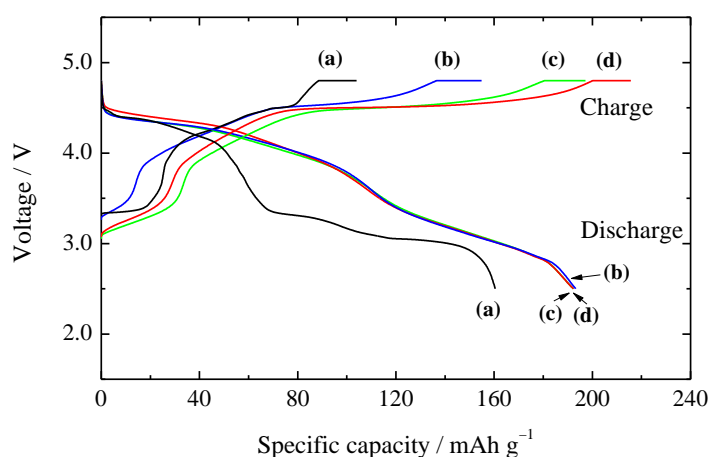
Figure 2-3-6-1. Initial charge and discharge curves for (a) $Li_{0.420}MnO_2$, (b) $Li_{0.520}MnO_2$, (c) $Li_{0.744}MnO_2$, and (d) $Li_{0.784}MnO_2$.

Figure 2-3-6-2 shows the charge and discharge curves of $Li_{0.784}MnO_2$ in the voltage range between 4.8 and 2.5 V vs Li/Li^+ at a constant current density of 10 mA g^{-1} (C/20) at 25 °C. The initial charge and discharge capacities were 200 and 192 mAh g^{-1}, respectively, with the initial coulombic efficiency of 96%. The values of charge and discharge capacities are equivalent to 0.69 and 0.63 electron transfers per formula unit, respectively. From this result, the chemical formula at 4.8 V charging state can be estimated to be $Li_{0.095}MnO_2$. This means that all of the lithium ions in $Li_{0.784}MnO_2$ could not be fully extracted at 4.8 V charging. It should be noted that the initial charge curve differs from those for the subsequent cycles. A remarkable 4.5 V plateau in the initial charge almost disappeared, and two plateaus at 3 V and 4 V regions are formed in the charge and discharge curves after the second cycle (Fig. 2-3-6-2). This fact may suggest the rearrangement of Li sites in the tunnel space after initial lithium extraction and
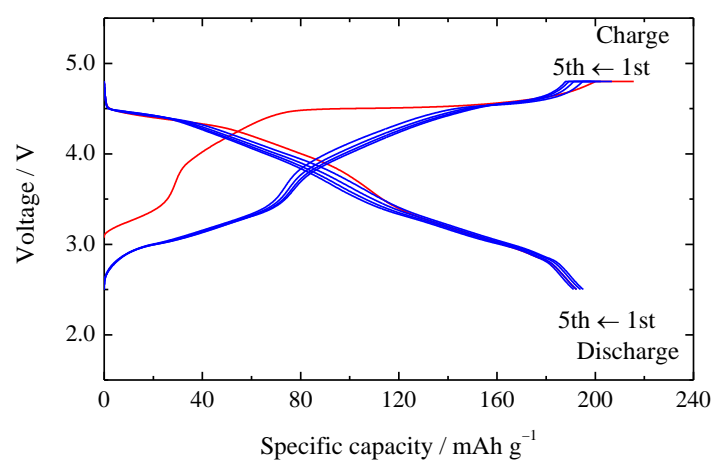
insertion reaction.

Figure 2-3-6-2. Charge and discharge curves for $Li_{0.784}MnO_2$.

Section II-IV Conclusion

  The crystal structure and electrochemical properties of a series of lithium manganese oxides, $Li_{0.44+x}MnO_2$ with tunnel-type $Na_{0.44}MnO_2$ structure were re-examined in the present study. Ion exchanged $Li_{0.44}MnO_2$ was synthesized from starting $Na_{0.44}MnO_2$. In addition, $Li_{0.55}MnO_2$, $Li_{0.77}MnO_2$, and $Li_{0.82}MnO_2$ were successfully prepared by the lithium insertion treatment. We first clarified the Li sites of $Li_{0.44+x}MnO_2$ from the crystal structure analysis using the ND measurement, and the Li sites were different from the Na sites of starting $Na_{0.44}MnO_2$. The Li sites of $Li_{0.55}MnO_2$ were determined, and the inserted 0.11 amounts of lithium was the same Li sites as $Li_{0.44}MnO_2$. In $Li_{0.77}MnO_2$ and $Li_{0.82}MnO_2$, one new Li site which was not present in $Li_{0.55}MnO_2$ was generated. Furthermore, since impurity phase Li_2CO_3 was present in $Li_{0.82}MnO_2$, the maximum Li amount was found to be around 0.80 due to the limitations of the crystal structure. The theoretical capacity of $Li_{0.44+x}MnO_2$ is 232 mAh g^{-1}, which is smaller than that of $LiCoO_2$. By clarifying the lithium sites by crystal structure analysis, the theoretical capacity can be estimated.

References

[1] M. M. Doeff, M. Y. Peng, Y. Ma, L. C. De Jonghe, *J. Electrochem. Soc.*, **141** (1994) L145.

[2] M. M. Doeff, T. J. Richardson, L. Kepley, *J. Electrochem. Soc.*, **143** (1996) 2507.

[3] A. R. Armstrong, H. Huang, R. A. Jennings, P. G. Bruce, *J. Mater. Chem.*, **8** (1998) 255.

[4] Y. U. Jeong, A. Manthiram, Electrochem. *Solid-State Lett.*, **2** (1999), 421.

[5] M. M. Doeff, A. Anapolsky, L. Edman, T. J. Richardson, L. C. De Jonghe, *J. Electrochem. Soc.*, **148** (2001), A230.

[6] J. Akimoto, J. Awaka, Y. Takahashi, N. Kijima, M. Tabuchi, A. Nakashima, H. Sakaebe, K. Tatsumi, Electrochem. *Solid-State Lett.*, **8** (2005) A554.

[7] J. Awaka, J. Akimoto, H. Hayakawa, Y. Takahashi, N. Kijima, M. Tabuchi, H. Sakaebe, and K. Tatsumi, *J. Power Sources*, **174**, (2007) 1218.

[8] N. Ishida, H. Hayakawa, H. Shibuya, J. Imaizumi, J. Akimoto, *J. Electrochem. Soc.*, **160** (2013) A297.

[9] V. Petricek, M. Dusek, L Palatinus, *Z. Kristallogr.*, 229 (2014) 345.

[10] J. Akimoto, H. Hayakawa, N. Kijima, J. Awaka, F. Funabiki, *Solid State Phenom.*, **170** (2011) 198.

[11] R. D. Shannon, *Acta Crystallogr.*, **A 32** (1976) 751.

[12] K. Kataoka, J. Awaka, N. Kijima, H. Hayakawa, K. Ohshima, J. Akimoto, *Chem. Mater.*, **23** (2011) 2344.

[13] J. Akimoto, Y. Takahashi, Y. Gotoh, S. Mizuta, *Chem. Mater.*, **12** (2000) 3246.

[14] J. Song, D. W. Shin, Y. H. Lu, C. D. Amos, A. Manthiram, J. B. Goodenough, *Chem. Mater.*, **24** (2012) 3101.

[15] H. Yamaguchi, A. Yamada, H. Uwe, *Phys. Rev. B*, **58** (1998) 8.

Chapter III
Lithium cobalt oxide LiCoMnO$_4$

－Investigation of phase transition

from layered rock-salt to spinel structure by heat treatment－

Section III-I   Introduction

Lithium cobalt manganese oxides have attracted great interest as cathode materials for lithium ion batteries due to their high potential and high capacity [1-10]. In particular, $LiCoMnO_4$ with spinel structure has been investigated as a promising cathode material [11-25]. Recently, thin-film all solid-state batteries using $LiCoMnO_4$ exhibited good cycling performance [17,20]. The redox potential at about 5 V vs. Li/Li$^+$ is due to redox reactions of $Co^{3+/4+}$. However, there are few studies on polycrystalline $LiCoMnO_4$ because of decomposition of the liquid electrolyte at about 5 V vs. Li/Li$^+$. Polycrystalline $LiCoMnO_4$ were synthesized by various synthetic methods, such as solid-state, sol-gel, and flux growth method [11-13,15,16,19-25].

Small single-crystal morphology of cathode materials is known to have advantages in rate capability and cycling performance, as demonstrated in the case of $LiNi_{0.5}Mn_{1.5}O_4$ with spinel structure [26–28]. Recently, we reported the synthesis of micrometer-sized $LiCoMnO_4$ single crystals by flux method at 750 °C, and electrochemical and structural properties were investigated [19]. Unfortunately, the initial discharge capacity of the obtained single-crystal $LiCoMnO_4$ sample was approximately 80 mA h g^{-1}, which was still less than the expected capacity from the redox reactions of $Co^{3+/4+}$. Rietveld analysis using power XRD data revealed the cation-mixing of Li/Co atoms not only at the tetrahedral 8a site but also the octahedral 16d site. The occupation value of Co atom in 8a site was determined to be about 4 %. This is a possible reason for the poor initial discharge capacity of $LiCoMnO_4$ with spinel structure; hence, the occupation value of Co atom in 8a site should be reduced. Lowering the synthesis temperature could be a way to reduce the occupation value.

Lithium-deficient $Li_{0.6}Co_{0.5}Mn_{0.5}O_2$ with O6-type layered rocksalt structure was prepared by ion-exchange of Na$^+$ for Li$^+$ from $Na_{0.6}Co_{0.5}Mn_{0.5}O_2$ with P2-type layered rocksalt structure [10]. The layered structures are named by the packing designation commonly used for ordered rocksalt-type oxides. For example, the letters O and P denote the alkali metal coordination (octahedral and prismatic, respectively), and the numbers 2, 3, and 6 denote the number of sheets within the unit cell [29]. The lithium content in $Li_xCo_{0.5}Mn_{0.5}O_2$ can be controlled by the starting $Na_xCo_{0.5}Mn_{0.5}O_2$ in the composition range of $0.6 \leq x \leq 1.0$ [2]. A similar chemical composition of lithium-deficient $Li_{0.7}Ni_{0.5}Mn_{0.5}O_2$ with O3-type layered rocksalt structure was reported to have a transformation of the crystal structure, depending on the heating temperature [30]. Above 300 °C, the crystal structure of O3-$Li_{0.7}Ni_{0.5}Mn_{0.5}O_2$ transformed to spinel structure. However, $LiCoMnO_4$ has not been reported to be prepared by a soft-chemical method upon heating O6-$Li_xCo_{0.5}Mn_{0.5}O_2$. The soft-chemical method is the lower synthesis temperature than the conventional solid-state method. Hence, the $LiCoMnO_4$ structure by the soft-chemical method is expected to reduce the occupation value of Co atom in 8a site, which may improve the electrochemical properties.

We study spinel structure of $LiCoMnO_4$ by the soft-chemical method, and electrochemical and structural properties of the samples are investigated for the first time.

Section III-II   Experiment

III-II-I   Synthesis

LiCoMnO$_4$ with spinel structure was synthesized by three steps. First, the starting Na$_x$Co$_{0.5}$Mn$_{0.5}$O$_2$ was synthesized prepared by solid-state method [10]. Co$_3$O$_4$ and Mn$_2$O$_3$ were crushed and mixed in an atomic ratio of Co:Mn = 1:1 in an agate mortar for a certain time. They were mixed with Na$_2$CO$_3$ in an atomic ratio of Mn:Na = 1:1.4, 1:1.2, and 1:1.1. The mixture was fired at 900 °C for 10 h in air. The starting Na$_x$Co$_{0.5}$Mn$_{0.5}$O$_2$ samples are referred to as NCMO1, NCMO2, and NCMO3 in order of increasing Na content.

Next, ion-exchanged Li$_x$Co$_{0.5}$Mn$_{0.5}$O$_2$ was prepared from the starting Na$_x$Co$_{0.5}$Mn$_{0.5}$O$_2$ by ion-exchange of Na$^+$ for Li$^+$ using LiNO$_3$ at 280 °C for 10 h in air [10]. The prepared mixture was washed with distilled water, and then dried 60 °C. The ion-exchanged Li$_x$Co$_{0.5}$Mn$_{0.5}$O$_2$ samples are referred to as LCMO1, LCMO2, and LCMO3 in order of increasing Li content.

Finally, to induce a structural transformation to spinel structure, ion-exchanged Li$_x$Co$_{0.5}$Mn$_{0.5}$O$_2$ was heated at 600 °C for 72 h in air. The heating samples are referred to as S-LCMO1, S-LCMO2, and S-LCMO3 in order of increasing Li content.

In comparison with soft-chemical method, LiCoMnO$_4$ was synthesized by flux method using MnCl$_2$, CoCl$_2$, and LiOH·H2O [19]. MnCl$_2$ and CoCl$_2$ were crushed and mixed in an atomic ratio of Co:Mn = 1:1 in the agate mortar under dry air for a certain time, and they were mixed with LiOH·H$_2$O in an atomic ratio of Mn:Li = 1:1.5. Excess LiOH·H$_2$O was used as a flux. Their mixture was fired at 650 °C for 48 h in a crucible sealed with a lid and cooled to around 100 °C at a cooling rate of 6 °C h^{-1}. The obtained sample was separated from the flux with distilled water, and then dried 60 °C. The obtained sample synthesized by flux method is referred to as F-LCMO.

III-II-II   Characterization

Phase purity was determined by X-ray diffraction (XRD) using Rigaku RINT-2550V equipped with a graphite monochromator with Cu Kα radiation operated at 40 kV and 200 mA. XRD data were recorded over a 2θ range of 10 to 70°, with a step time and size of 1.0 s and 0.03°, respectively. The structure refinement by Rietveld analysis using synchrotron XRD data was performed. Synchrotron XRD measurements were carried out in BL19B2 at SPring-8 (Sayo-gun, Hyogo, Japan). The powder samples were sealed in a Lindeman glass capillary with 0.3 mm diameter. The incident X-ray wavelength was 0.49996 Å, and exposure time was a range of 15 to 20 min. Synchrotron XRD data were recorded over a 2θ range of 4 to 75°, with a step size of 0.01°. Rietveld analysis was performed using Jana2006 program [31]. X-ray absorption fine structure spectroscopy (XAFS) at Co- and Mn-K edges was carried out in BL9C at Photon Factory in High Energy Accelerator Research Organization (Tsukuba, Ibaraki, Japan).

Chemical composition analysis was performed by inductively coupled plasma-atomic emission spectroscopy (ICP-AES) using HITACHI P-4010. Thermogravimetric and differential thermal analysis (TG-DTA) were performed using SII TG/DTA7200 from 100 to 800 °C at a heating rate of 10 °C min−1 in air. The particle morphology and size were observed by scanning electron microscopy (SEM) using JEOL JCM-6000.

Electrochemical measurements were performed using coin cells (CR2032) assembled in an argon-filled glove box. The working electrode was prepared using 5 mg of active material, 5 mg

of acetylene black (AB) as the conductive agent, and 1 mg of polytetrafluoroethylene (PTFE) as the binder. In order to investigate electrochemical properties inherently possessed by the active material, the high conductive agent ratio, which is not affected by the electrode preparation method, was used. An aluminum mesh was used as the current collector, and the electrode diameter was 15 mm. The counter electrode was a circular Li foil with a diameter of 16 mm. The separator was a microporous polypropylene sheet. The liquid electrolyte was a 1 M LiPF6 solution in a mixture of ethylene carbonate (50 vol %) and diethyl carbonate (50 vol %). The cells were charged at 10 mA g^{-1} for 24 h at 25 °C and discharged to 3.0 V vs. Li/Li$^+$.

Section III-III   Results and Discussion

III-III-I   Synthesis

 Figure 2-3-1-1 shows the XRD patterns of the starting NCMO with the different content of Na. These patterns were indexed to P2-type layered rocksalt structure with space group $P6_3/mmc$ [10]. Table 2-3-1-1 summarizes the chemical composition of all the samples by ICP-AES. The Na content of all the starting NCMO was smaller than the nominal amount of Na_2CO_3 because it vaporized by the higher firing temperature than the melting point of Na_2CO_3. The hexagonal lattice parameters of NCMO were calculated by least-squares method, as listed in Table 1. The lattice parameters of NCMO were similar to the reported values for P2-$Na_{0.6}Co_{0.5}Mn_{0.5}O_2$ [10].
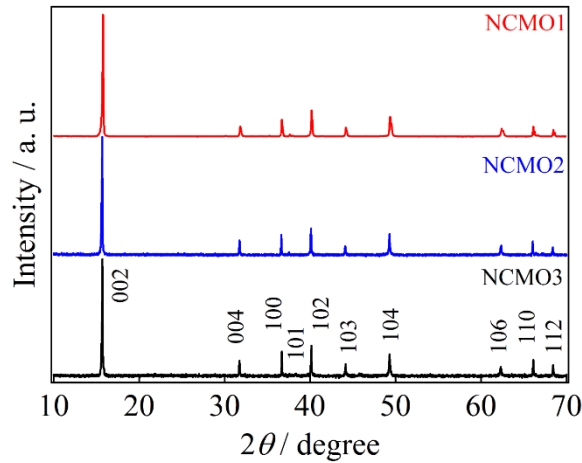
Figure 2-3-1-1. X-ray diffraction patterns of NCMO1, NCMO2, and NCMO3.

Table 2-3-1-1. Chemical composition and lattice parameters of all the samples in the present study.

Sample#	Chemical comp.	Crystal system (S.G.)	a (Å)	c (Å)
Starting samples[1] fired at 900 °C for 10 h				
NCMO1	$Na_{0.70}Co_{0.50}M_{0.50}O_2$	Hexagonal ($P6_3/mmc$)	2.82440 (11)	11.2351 (9)
NCMO2	$Na_{0.60}Co_{0.50}Mn_{0.50}O_2$	Hexagonal ($P6_3/mmc$)	2.82731 (12)	11.2550 (10)
NCMO3	$Na_{0.55}Co_{0.50}Mn_{0.50}O_2$	Hexagonal ($P6_3/mmc$)	2.82448 (12)	11.2647 (10)
Ion-exchanged samples[2] after ion-exchange of Na^+ for Li^+ at 280 °C for 10 h				
LCMO1	$Li_{0.60}Co_{0.51}Mn_{0.49}O_2$	Rhombohedral ($R-3m$)	2.81327 (12)	29.550 (4)
LCMO2	$Li_{0.54}Co_{0.50}Mn_{0.50}O_2$	Rhombohedral ($R-3m$)	2.81742 (15)	29.628 (4)
LCMO3	$Li_{0.50}Co_{0.50}Mn_{0.50}O_2$	Rhombohedral ($R-3m$)	2.81881 (13)	29.626 (8)
Spinel samples[2] after heating at 600 °C for 72 h				
S-LCMO1	$Li_{1.10}Co_{0.96}Mn_{0.94}O_4$	Cubic ($Fd-3m$)	8.0559 (6)	
S-LCMO2	$Li_{1.05}Co_{0.98}Mn_{0.97}O_4$	Cubic ($Fd-3m$)	8.0570 (8)	
S-LCMO3	$Li_{1.00}Co_{1.01}Mn_{0.99}O_4$	Cubic ($Fd-3m$)	8.0577 (9)	

1) Nominal chemical composition

2) Analytical chemical composition determined by ICP-AES

Figure 2-3-1-2 shows the XRD patterns of ion-exchanged LCMO prepared from the starting NCMO. These patterns were indexed to O6-type layered rocksalt structure with space group $R-3m$ [10]. The hexagonal lattice parameters of LCMO were calculated by least-squares method, as listed in Table 2-3-1-1. The control of Li content in ion-exchanged LCMO was successfully carried out by adjusting the nominal amount of Na_2CO_3. The residual Na content for all the ion-exchanged LCMO was less than 0.01 per chemical formula, indicating the completion of ion-exchange under this experimental condition. The lattice parameters of LCMO were similar to the reported values for O6-$Li_{0.6}Co_{0.5}Mn_{0.5}O_2$ [10].
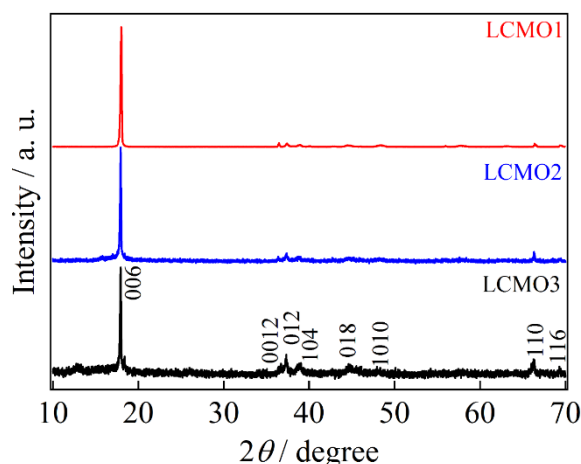
Figure 2-3-1-2. X-ray diffraction patterns of LCMO1, LCMO2, and LCMO3.

Figure 2-3-1-3 shows the TG-DTA curves of ion-exchanged LCMO1. The TG curve exhibited a weight loss from 125 to 700 °C. A similar weight loss has been reported to be caused by oxygen loss [7,30]. The DTA curve exhibited an endothermic peak at about 600 °C due to the structural transformation to spinel structure, as confirmed by the following XRD patterns of S-LCMO.
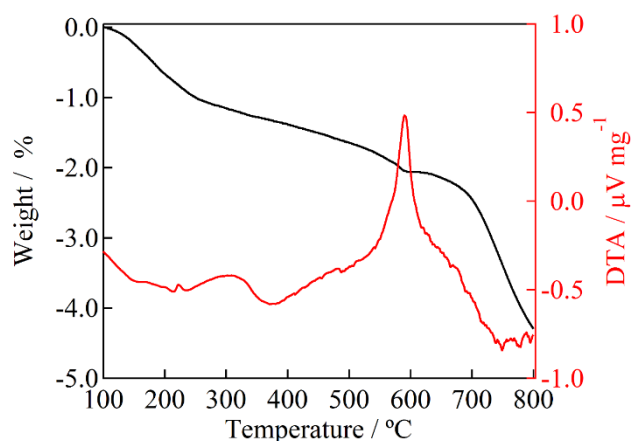
Figure 2-3-1-3. TG-DTA curves of LCMO1.

Figure 2-3-1-4 shows the XRD patterns of S-LCMO prepared by heating ion-exchanged LCMO. These patterns were indexed to spinel structure with space group $Fd-3m$ [13,19,21–25]. Table 1 lists the cubic lattice parameters of S-LCMO refined by Rietveld analysis. The a-axis

length of S-LCMO was similar to the reported value for LiCoMnO$_4$, the value of which was 8.0565(4) Å [13]. In addition, the *a*-axis length of S-LCMO decreased as the substitution content of Li increased from 1.00 to 1.10. The change of the *a*-axis length follows Vegard's law, which linearly depends on the substitution content of Li.
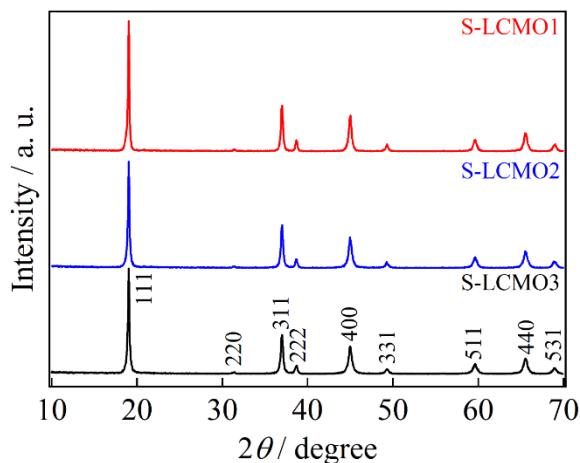
Figure 2-3-1-4. X-ray diffraction patterns of S-LCMO1, S-LCMO2, and S-LCMO3.

Figure 2-3-1-5 compares the SEM images of S-LCMO1 and F-LCMO. The SEM image of S-LCMO1 showed a platelet-like morphology with an average size of 5 μm, which was larger than previously reported [15,16,19,21–24]. The particle morphology and size remained nearly unchanged from those in the starting material NCMO1. On the contrary, the SEM image of F-LCMO showed an octahedral crystal morphology with an average size of 0.5 μm.
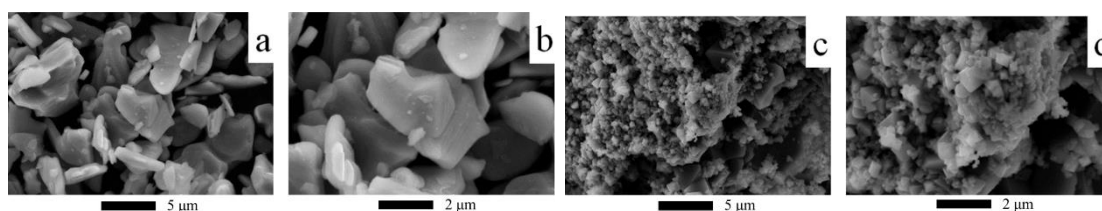
Figure 2-3-1-5. SEM images of (a, b) S-LCMO1 and (c, d) F-LCMO.

III-III-II   Crystal structure of LiCoMnO$_4$

  Figure 2-3-2-1 shows normalized Co and Mn K-edge X-ray absorption near-edge structure (XANES) spectra of S-LCMO and F-LCMO. Each spectrum is plotted together with CoO, Co$_3$O$_4$, Mn$_2$O$_3$, and β-MnO$_2$ as standards for comparison; the pre-edge peak area of each sample is shown in more detail in the corresponding inset. The XANES spectra of S-LCMO and F-LCMO were similar to those of LiCoMnO$_4$ reported previously [12,13]. The main absorption edge peaks of S-LCMO and F-LCMO were similar to those from Co$_3$O$_4$ (Co$^{2.7+}$) and β-MnO$_2$ (Mn^{4+}) as standards, in which Co and Mn were primarily in +2.7 and +4.0 oxidation states, respectively. Small differences in the pre-edge peak intensity (Fig. 2-3-2-1 inset) between these samples suggest that there may be slight differences in local structures [6]. In particular, the presence of a small amount of Mn^{3+} was suggested, because the intensity A2/A1 ratio of S-LCMO and F-LCMO at the pre-edge peak of Mn K edge was smaller than that of β-MnO$_2$ (Mn^{4+}), as shown in the inset of Fig. 2-3-2-1[3,32,33]. Accordingly, the valence state of S-LCMO is consistent with that of F-LCMO, as confirmed by the following Rietveld analysis.
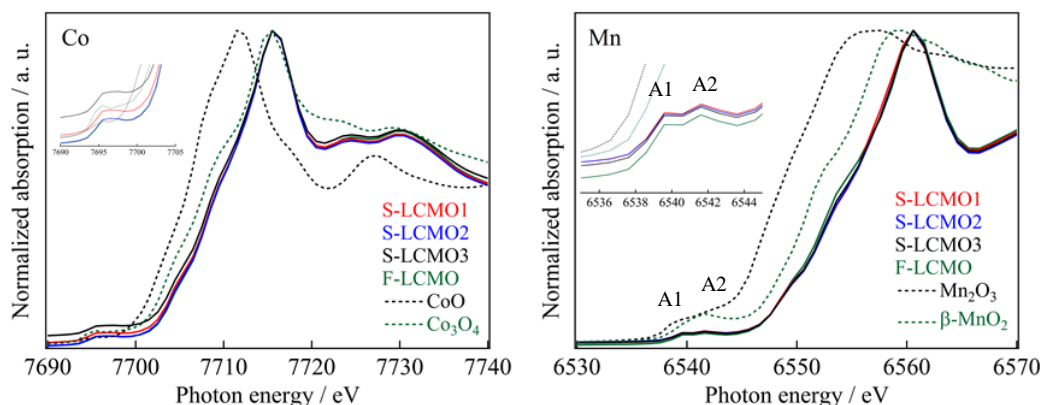
Figure 2-3-2-1. Normalized Co and Mn K-edge XANES spectra of S-LCMO1, S-LCMO2, S-LCMO3, and F-LCMO. Each spectrum is plotted together with CoO and Co$_3$O$_4$ or Mn$_2$O$_3$ and β-MnO$_2$ as standards for comparison.

  In order to determine accurately the crystal structure of S-LCMO1 and F-LCMO, the refinement was performed by Rietveld analysis using synchrotron XRD data, and the structural formula (Li$_{1-x}$Co$_x$)$_{8a}$[Co$_{1-y-z}$Mn$_y$Li$_z$]$_{16d}$O$_4$ and space group Fd-$3m$ in the previous report were used as initial structure models [13,19]. The chemical composition of S-LCMO1 and F-LCMO was fixed to be Li$_{1.10}$Co$_{0.96}$Mn$_{0.94}$O$_4$ and Li$_{0.96}$Co$_{1.05}$Mn$_{0.99}$O$_4$ by ICP-AES, respectively. In addition, the isotropic atomic displacement parameters (U_{iso}) were refined for each atom except for the O atom.

  Figure 2-3-2-2 shows the observed and calculated XRD diffraction patterns of S-LCMO1 and F-LCMO. Good agreements were obtained between the observed and calculated diffraction patterns of S-LCMO1 and F-LCMO. The resultant R values of S-LCMO1 reached R_{wp} = 6.44 % and R_p = 4.23 %, with a fit indicator of $S = R_{wp}/R_e$ = 1.95. These patterns were indexed to spinel structure with space group Fd−$3m$, except for broad peaks in the 2θ range of 6 to 8°. The broad peaks were most likely to be Li$_2$MnO$_3$, which originated from Li and Mn atoms ordering in transition metal sites in layered rocksalt structure [34,35]. Tables 2-3-2-1 and 2-3-2-2 summarize the atomic coordinates of S-LCMO1 and F-LCMO, respectively.
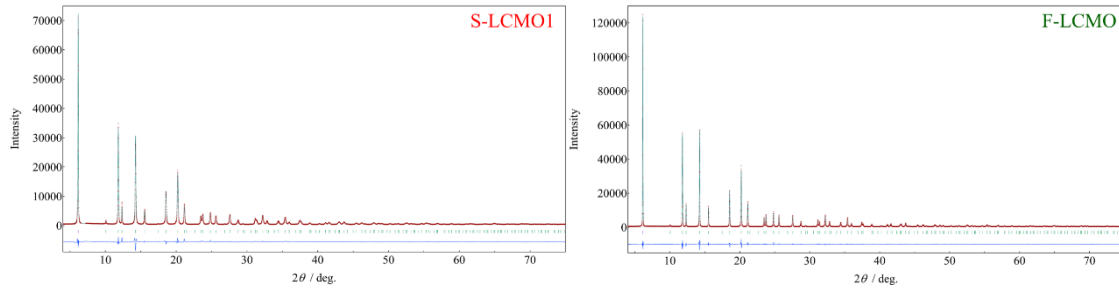
Figure 2-3-2-2. Observed (plus marks), calculated (solid line), and difference (bottom) patterns for Rietveld analysis from synchrotron powder XRD diffraction data of S-LCMO1 and F-LCMO. The short vertical lines below the profile indicate the peak positions of all the possible Bragg reflections.

Table 2-3-2-1. Structural parameters of S-LCMO1 determined by Rietveld analysis using synchrotron XRD data. SG: $Fd\bar{3}m$, $a = 8.05338(4)$ Å, $R_{wp} = 6.44\%$, $R_p = 4.23\%$, $S = 1.95$, $Z = 8$.

Atom	Site	x/a	y/b	z/c	Occupancy	U_{iso} / Å^2
Li1	8a	1/8	1/8	1/8	0.9184(14)	0.0087(8)
Co1	8a	1/8	1/8	1/8	0.0816(14)	0.0087(8)
Co2	16d	1/2	1/2	1/2	0.423	0.00209(7)
Mn1	16d	1/2	1/2	1/2	0.480	0.00209(7)
Li2	16d	1/2	1/2	1/2	0.097	0.00209(7)
O1	32e	0.26227(7)	0.26227(7)	0.26227(7)	1	0.006

Table 2-3-2-2. Structural parameters of F-LCMO determined by Rietveld analysis using synchrotron XRD data. SG: $Fd\bar{3}m$, $a = 8.05478(2)$ Å, $R_{wp} = 6.90\%$, $R_p = 4.72\%$, $S = 2.14$, $Z = 8$.

Atom	Site	x/a	y/b	z/c	Occupancy	U_{iso} / Å^2
Li1	8a	1/8	1/8	1/8	0.9704(15)	0.0108(12)
Co1	8a	1/8	1/8	1/8	0.0296(15)	0.0108(12)
Co2	16d	1/2	1/2	1/2	0.495	0.00244(4)
Mn1	16d	1/2	1/2	1/2	0.5042	0.00244(4)
Li2	16d	1/2	1/2	1/2	0.0008	0.00244(4)
O1	32e	0.26203(7)	0.26203(7)	0.26203(7)	1	0.006

The cubic lattice parameter for S-LCMO1 was refined to be $a = 8.05338(4)$ Å and $Z = 8$. The a-axis length of S-LCMO1 ($Li_{1.10}Co_{0.96}Mn_{0.94}O_4$) was smaller than that of $Li_{1.10}Mn_{1.90}O_4$, the value of which was $a = 8.2401(9)$ Å [36]. This difference is due to the substitution of Co for Mn. The octahedral 16d site is occupied by Co, Mn, and Li atoms. They are coordinated by six neighboring oxygen atoms in a (Co, Mn, Li)O_6 octahedron. The average bond distance of (Co, Mn, Li) − O in the octahedron was 1.920 Å, and the average valence states of Co and Mn were + 2.80 and + 3.88, respectively, by bond valence sum (BVS) calculations [37]. As in the case of LCMO1 before the structural transformation to spinel structure (S-LCMO1), the transition metal sites are occupied by Co and Mn atoms. The average bond distance of (Co, Mn) − O in the octahedron was 1.899 Å, and the average valence states of Co and Mn were + 2.96 and + 4.10, respectively [10]. This difference between S-LCMO1 and LCMO1 can be explained by

oxygen loss, as shown in Fig. 2-3-1-3. The tetrahedral $8a$ site is occupied by Li and Co atoms. They are coordinated by four neighboring oxygen atoms in a (Li, Co)O_4 tetrahedron. The average bond distance of (Li, Co) − O in the tetrahedron was 1.915 Å, and the average valence state of Co was +1.89. The occupation rate of Co atom at the tetrahedral $8a$ site was 8.16 %. The cation-mixing of the octahedral $16d$ and tetrahedral $8a$ site is possible, because the ionic radius of these cations is similar. For Mn^{4+} and low spin Co^{3+} in the octahedral coordination, the ionic radiuses are 0.53 and 0.545 Å, respectively; for Li^+ and Co^{2+} in the tetrahedral coordination, the ionic radiuses are 0.58 and 0.59 Å, respectively [38]. According to Reeves's report, Co^{2+} was found to migrate from the octahedral $16d$ site to the tetrahedral $8a$ site, after reduction of Co^{3+} to Co^{2+} due to oxygen loss during the synthesis of $LiCoMnO_4$ with spinel structure [18]. In addition, in parallel with the reduction of Co^{3+} to Co^{2+}, Mn^{4+} was reduced to Mn^{3+} during the synthesis of $LiCoMnO_4$ with spinel structure [18].

As in the case of F-LCMO, the resultant R values reached R_{wp} = 6.90 % and R_p = 4.72 %, with a fit indicator of $S = R_{wp}/R_e$ = 2.14. The cubic lattice parameter for F-LCMO was refined to be a = 8.05478(2) Å and Z = 8. The a-axis length of F-LCMO was similar to S-LCMO1, the value of which was 8.05338(4) Å. The occupation rate of Co atom at the tetrahedral $8a$ site was 2.96 %. The intensity of 220 diffraction line at about 2θ = 10° is slightly smaller than that for S-LCMO1, indicating that a small amount of Co is present at the tetrahedral $8a$ site. The average bond distance of (Li, Co) − O in the tetrahedron was 1.914 Å, and the average valence state of Co was + 1.89. The average bond distance of (Co, Mn, Li) − O in the octahedron was 1.920 Å, and the average valence states of Co and Mn were + 2.79 and + 3.87, respectively. Accordingly, we can conclude that no apparent difference in the average valence states of Co and Mn was observed between S-LCMO1 and F-LCMO.

III-III-III   Electrochemical properties

Figure 2-3-3-1 shows the charge and discharge curves of F-LCMO and S-LCMO for initial seven cycles. The irreversible capacity of F-LCMO and S-LCMO was due to decomposition of the liquid electrolyte at about 5.0 V vs. Li/Li$^+$. Because the amount of decomposition depends on the holding time at high potential, the irreversible capacity increases in the case of low current rate of 10 mA g^{-1}. In the case of high current rate, the irreversible capacity can be reduced [15]. The discharge capacity of F-LCMO was about 90 mAh g^{-1} in the second cycle. Two plateaus at 5.1 and 4.9 V vs. Li/Li$^+$ were due to redox reactions of Co$^{3+/4+}$ [39]. The 4 V shoulders were due to redox reactions of Mn$^{3+/4+}$, such as LiMn$_2$O$_4$ and LiNi$_{0.4}$Mn$_{1.6}$O$_4$, indicating the presence of Mn^{3+} in F-LCMO [40]. This was consistent with BVS calculations. In comparison with LiCoMnO$_4$ having the cation-mixing of 11.3 %, the discharge capacity of F-LCMO, which reduced the cation-mixing to 2.96 %, did not increase [22]. Therefore, it is suggested that the cause of the low discharge capacity is not cation-mixing.
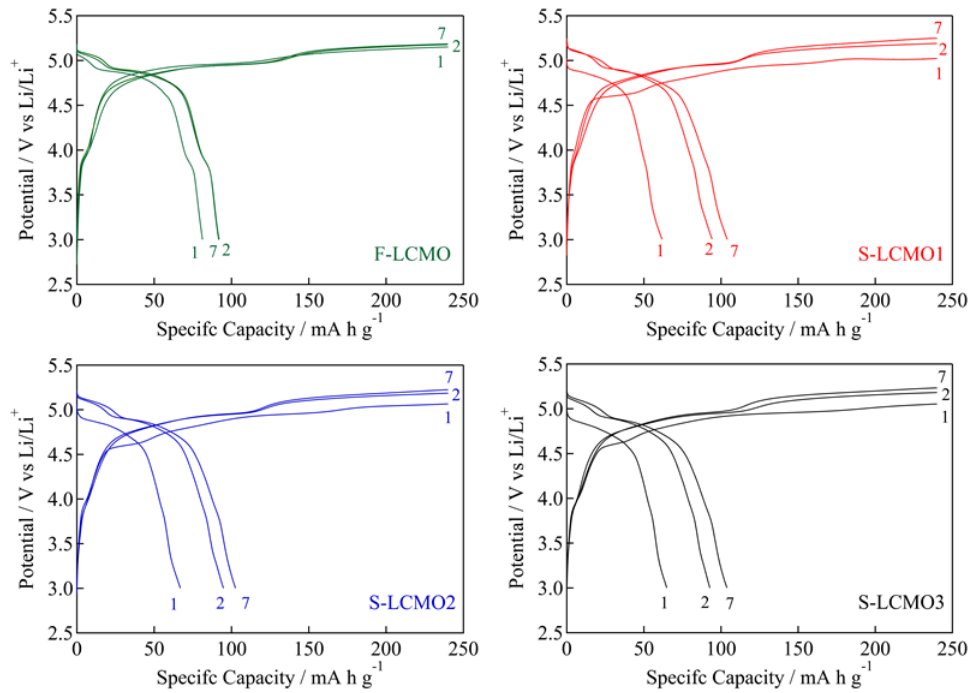
Figure 2-3-3-1. Charge and discharge curves of F-LCMO, S-LCMO1, S-LCMO2, and S-LCMO3 for initial seven cycles.

The initial charge curve of S-LCMO exhibits a 4.5 V vs. Li/Li$^+$ plateau that suggests the presence of Li$_2$MnO$_3$ [41,42]. A similar initial charge plateau at about 4.5 V vs. Li/Li$^+$ was previously observed in O3-Li$_{0.7}$Ni$_{1-y}$Mn$_y$O$_2$ ($0.5 \leq y \leq 0.8$) using heat treatment, as detected for Li$_2$MnO$_3$ by ^{6}Li-MAS-NMR [31]. The second charge curve of S-LCMO does not exhibit the 4.5 V plateau. The maximum discharge capacity of S-LCMO was about 105 mAh g^{-1}. The 4 V shoulders, which were due to redox reactions of Mn$^{3+/4+}$, disappeared in spite of the presence of Mn^{3+}. In comparison with F-LCMO, the shape of the discharge curves exhibits a gradually sloping profile from 4.5 to 3.0 V, which suggests the presence of Li$_2$MnO$_3$ [42]. This fact was supported by synchrotron XRD data. As a result, S-LCMO showed similar electrochemical property to F-LCMO, in spite of both the large micrometer-sized particle and the presence of

Li$_2$MnO$_3$.

Section III-IV Conclusion

We have reported a novel synthetic route of micrometer-sized $LiCoMnO_4$ with spinel structure from ion-exchanged $Li_xCo_{0.5}Mn_{0.5}O_2$ with O6-type layered rocksalt structure. The average particle size of about 5 μm was almost the same as that of the starting $Na_xCo_{0.5}Mn_{0.5}O_2$ with P2-type layered rocksalt structure. Rietveld analysis revealed the cation-mixing of Li/Co atoms not only at the tetrahedral 8*a* site but also the octahedral 16*d* site. In addition, some weak peaks assigned to Li_2MnO_3 are observed. The present $LiCoMnO_4$, which had the cation-mixing of 11.3 %, exhibited a maximum discharge capacity of about 105 mA h g^{-1} at 25 °C, in spite of both the large micrometer-sized particle and the presence of Li_2MnO_3. In this synthesis route, the cation-mixing was not reduced, but almost the same discharge capacity as the previous report was obtained. Therefore, the cation mixing is not a cause of low discharge capacity.

Reference

[1] A. Kajiyama, K. Takada, T. Inada, M. Kouguchi, S. Kondo, M. Watanabe, *J. Electrochem. Soc.*, **148** (2001) 981.

[2] A. Kajiyama, K. Takada, T. Inada, M. Kouguchi, S. Kondo, M. Watanabe, *Solid State Ionics*, **149** (2002) 39.

[3] Y. J. Park, Y.-S. Hong, X. Wu, M. G. Kim, K. S. Ryu, S. H. Chang, *Bull. Korean Chem. Soc.*, **25** (2004) 511.

[4] F. Tournadre, L. Croguennec, I. Saadoune, F. Weill, Y. Shao-Horn, P. Willmann, C. Delmas, *Chem. Mater.*, **16** (2004) 1411.

[5] F. Tournadre, L. Croguennec, I. Saadoune, M. Morcrette, P. Willmann, C. Delmas, Chem. Mater. 16 (2004) 1418–1426.

[6] J. Bareño, M. Balasubramanian, S. H. Kang, J. G. Wen, C. H. Lei, S. V. Pol, I. Petrov, D. P. Abraham, *Chem. Mater.*, **23** (2011) 2039.

[7] S. Komaba, L. Croguennec, F. Tournadre, P. Willmann, C. Delmas, *J. Phys. Chem. C*, **117** (2013) 3264.

[8] E. McCalla, C. M. Lowartz, C. R. Brown, J. R. Dahn, *Chem. Mater.*, **25** (2013) 915.

[9] B. R. Long, J. R. Croy, F. Dogan, M. R. Suchomel, B. Key, J. Wen, D. J. Miller, M. M. Thackeray, M. Balasubramanian, *Chem. Mater.*, **26** (2014) 3565.

[10] J. Akimoto, A. Takashima, K. Kataoka, N. Ishida, Y. Idemoto, Synthesis, *Solid State Ionics*, **263** (2014) 167.

[11] H. Kawai, M. Nagata, H. Tukamoto, A. R. West, *Electrochem. Solid-State Lett.*, **1** (1998) 212.

[12] H. Kawai, M. Nagata, H. Kageyama, H. Tukamoto, A. R. West, *Electrochim. Acta* **45** (1999) 315.

[13] H. Shigemura, M. Tabuchi, H. Kobayashi, H. Sakaebe, A. Hirano, H. Kageyama, *J. Mater. Chem.*, **12** (2002) 1882.

[14] K. Dokko, N. Anzue, M. Mohamedi, T. Itoh, I. Uchida, *Electrochem. Commun.*, **6** (2004) 384.

[15] M. Hu, Y. Tian, L. Su, J. Wei, Z. Zhou, *ACS Appl. Mater. Interfaces*, **5** (2013) 12185.

[16] M. Hu, Y. Tian, J. Wei, D. Wang, Z. Zhou, *J. Power Sources*, **247** (2014) 794.

[17] N. Kuwata, S. Kudo, Y. Matsuda, J. Kawamura, *Solid State Ionics*, **262** (2014) 165.

[18] N. Reeves-McLaren, J. Sharp, H. Beltran-Mir, W. M. Rainforth, A. R. West, *Proc. R. Soc. A*, **472** (2016) 20140991.

[19] Y. Hamada, N. Hamao, K. Kataoka, N. Ishida, Y. Idemoto, J. Akimoto, *J. Ceram. Soc. Japan*, **124** (2016) 706.

[20] H. Li, W. C. West, M. Motoyama, Y. Iriyama, *Thin Solid Films*, **615** (2016) 210.

[21] A. Windmüller, CL. Tsai, S. Möller, M. Balski, Y. J. Sohn, S. Uhlenbruck, O. Guillon, *J. Power Sources*, **341** (2017) 122.

[22] K. Mukai, T. Uyama, *ACS Omega*, **2** (2017) 5142.

[23] C. Dräger, F. Sigel, S. Indris, D. Mikhailova, L. Pfaffmann, M. Knapp, H. Ehrenberg, *J. Power Sources*, **371** (2017) 55.

[24] K. Ariyoshi, H. Yamamoto, Y. Yamada, *Electrochim. Acta*, **260** (2018) 498.

[25] A. Windmüller, C. A. Bridges, CL. Tsai, S. Lobe, C. Dellen, G. M. Veith, M. Finsterbusch,

S. Uhlenbruck, O. Guillon, *ACS Appl. Energy Mater.*, **1** (2018) 715.

[26] J.-H. Kim, S.-T. Myung, Y.-K. Sun, *Electrochim. Acta*, 49 (2004) 219–227.

[27] Y. Takahashi, H. Sasaoka, R. Kuzuo, N. Kijima, J. Akimoto, *Electrochem. Solid-State Lett.*, **9** (2006) A203.

[28] K. Ariyoshi, Y. Maeda, T. Kawai, T. Ohzuku, *J. Electrochem. Soc.*, **158** (2011) A281.

[29] C. Delmas, C. Fouassier, P. Hagenmuller, *Physica B+C*, **99** (1980) 81.

[30] K. Chiba, N. Taguchi, M. Shikano, H. Sakaebe, *J. Power Sources*, **311** (2016) 103.

[31] V. Petricek, M. Dusek, L Palatinus, *Z. Kristallogr.*, **229** (2014) 345.

[32] M. Belli, A. Scafati, A. Bianconi, S. Mobilio, L. Palladino, A. Reale, E. Burattini, *Solid State Commun.*, **35** (1980) 355.

[33] B. Ammundsen, D.J. Jones, J. RozieÁre, G. R. Burns, *Chem. Mater.*, **8** (1996) 2799.

[34] J. Bréger, M. Jiang, N. Dupré, Y. S. Meng, Y. Shao-Horn, G. Ceder, C. P. Grey, *J. Solid State Chem.*, **178** (2005) 2575.

[35] A. Boulineau, L. Croguennec, C. Delmas, F. Weill, *Solid State Ionics*, **180** (2010) 1652.

[36] Y. Takahashi, N. Kijima, J. Akimoto, *Solid State Ionics* **177** (2006) 691.

[37] N. E. Brese, M. O'keeffe, *Acta Crystallogr.*, **B47** (1991) 192.

[38] R. D. Shannon, *Acta Crystallogr.* **A32** (1976) 751.

[39] R. Alcàntara, M. Jaraba, P. Lavela, J. L. Tirado, *J. Electrochem. Soc.*, **151** (2004) A53.

[40] K. Kanamura, W. Hoshikawa, *Solid State Ionics*, **177** (2006) 113.

[41] T. Ohzuku, M. Nagayama, K. Tsuji, K. Ariyoshi, *J. Mater. Chem.*, **21** (2011) 10179.

[42] K. Kubota, T. Kaneko, M. Hirayama, M. Yonemura, Y. Imanari, K. Nakane, R. Kanno, *J. Power Sources*, **216** (2012) 249.

Chapter IV
Lithium nickel oxide $Li_{2/3}Ni_{1/3}Mn_{2/3}O_2$

－Investigation of the ratio of layered rock-salt

and spinel structure by heat treatment temperature－

Section IV-I　Introduction

Lithium nickel manganese oxide, $Li_{2/3}Ni_{1/3}Mn_{2/3}O_2$, with a layered structure has been extensively investigated as a positive electrode material for rechargeable Li-ion batteries [1–5]. Paulsen et al. revealed superior battery characteristics of O2-type $Li_{2/3}Ni_{1/3}Mn_{2/3}O_2$, such as good cycle performance and a discharge capacity of about 170 mA h g^{-1} between 4.6 and 2.5 V [1]. On the other hand, O3-type $Li_{2/3}Ni_{1/3}Mn_{2/3}O_2$ shows a remarkable discharge capacity of about 200 mA h g^{-1} between 4.7 and 2.5 V; however, it shows poor cycling [6]. The stacking of oxide ions in the O3-type structure is very similar to that of the spinel structure; therefore, the O3-type structure is unstable and easily converts to the spinel structure during electrochemical cycling. This is the main reason for the poor capacity retention in O3-type $Li_{2/3}Ni_{1/3}Mn_{2/3}O_2$.

O3-$Li_{2/3}Ni_{1/3}Mn_{2/3}O_2$ exists as a metastable phase and has been prepared by the Li ion exchange reaction using the Na-based layered compound, P3-$Na_{2/3}Ni_{1/3}Mn_{2/3}O_2$, in an anhydrous molten salt at about 300 °C. Similar chemical composition of O3-$Li_{0.9}Ni_{0.5}Mn_{0.5}O_2$ was reported to have a variation in the crystal structure, depending on the heat-treatment temperature [7]. Above 300 °C, the crystal structure of O3-$Li_{0.9}Ni_{0.5}Mn_{0.5}O_2$ transform to the spinel structure; however, the electrochemical properties were not reported. It is well-known that the O3-type structures convert to the spinel structures during electrochemical cycling [2]. Therefore, the crystal structure is considered to be stabilized in the spinel-like form. Upon increasing the temperature, the O3-$Li_{2/3}Ni_{1/3}Mn_{2/3}O_2$ structure is expected to undergo phase transformation to the spinel-like form, which may improve the electrochemical properties.

In the present study, we have attempted the modification of the layered structure O3-$Li_{2/3}Ni_{1/3}Mn_{2/3}O_2$ using heat treatment. A 5 V class plateau was confirmed for the first time.

Section IV-II Experiment

The precursor, P3-$Na_{2/3}Ni_{1/3}Mn_{2/3}O_2$, was synthesized by a conventional solid-state reaction with stoichiometric amounts of CH_3COONa (98.5% pure), $Ni(OH)_2$ (99.9% pure), and Mn_2O_3 (99.9% pure), with 3% excess Na [2,4,8]. The weighed powder was mixed by ball milling, and then pressed into pellets. The pellets were heated at 650 °C under O_2 flow for 10 h, and then pulverized. The P3-$Na_{2/3}Ni_{1/3}Mn_{2/3}O_2$ powder was mixed with $LiNO_3$ and LiCl (88:12 by weight, with Li/Na = 7) and heated at 260 °C for 1 h in air [2,4]. After the ion exchange reaction, the sample was washed with distilled water and then dried at 80 °C overnight. Finally, to control the crystal structure, the samples were heated at 300, 400, 500, 600, and 700 °C for 5 h in air. Hereafter, we denote O3-$Li_{2/3}Ni_{1/3}Mn_{2/3}O_2$ with thermal treatments at 300, 500, and 700 °C as $O3_{300}$-, $O3_{500}$-, and $O3_{700}$-$Li_{2/3}Ni_{1/3}Mn_{2/3}O_2$, respectively.

The phase purity and crystal structure of the obtained samples were determined by powder X-ray diffraction (XRD) using an AXS D8 ADVANCE diffractometer (Bruker) with a Cu Kα radiation source (operating conditions: 40 kV, 55 mA). The XRD intensity data were collected for 0.5 s at each 0.02° step over a 2θ range of 10°–70°. TOPAS ver. 4.2 software package was used for Pawley analysis [9].

The solid-state [6]Li magic-angle-spinning nuclear-magnetic-resonance ([6]Li-MAS-NMR) spectra of the samples were obtained at room temperature using an AVANCE300 spectrometer (Bruker) at 44 MHz with a spinning rate of 50 kHz for Li nuclei by a rotor-synchronized spin-echo pulse sequence. The pulse width was 3.6 μs (π/2 pulse). The chemical shift was recorded relative to 1.0 M [6]LiCl aqueous solution.

The cationic composition (e.g., Li, Na, Ni, and Mn contents) was determined by inductively coupled plasma-atomic emission spectroscopy (ICP-AES) (Shimadzu ICPS-8000). Electrochemical cycling was performed using CR2032 coin-type cells. The working electrodes were prepared using 10 mg of active material, 10 mg of acetylene black as the conductive agent, and 2 mg of polyvinylidene difluoride as the binder. Al mesh was used as the current collector, and the electrode diameter was 14 mm. The counter electrode was a Li foil cut in a circle with 16 mm diameter and 0.2 mm thickness. A microporous polypropylene sheet was used as a separator. A solution of 1 mol dm^{-3} $LiPF_6$ in a 1:2 (v/v) mixture of ethylene carbonate and diethyl carbonate was used as the electrolyte. Cells were constructed in a dry room with a dew point below −50 °C, and electrochemical measurements were carried out with a current density of 15 mA g^{-1} (19 mA cm^{-2}) at 25 °C after standing overnight under an open circuit condition.

Section IV-III   Results and Discussion

The XRD pattern of P3-$Na_{2/3}Ni_{1/3}Mn_{2/3}O_2$, the precursor for the ion exchange reaction, shows that it can be synthesized almost as a single-phase (Fig. 4-3-1). The lattice parameters, a = 2.8865 (1) and c = 16.781 (1) Å, are in good agreement with those of the previous report (a = 2.8867 and c = 16.7812 Å) [4]. The chemical formula of the precursor is $Na_{0.68}Ni_{0.33}Mn_{0.66}O_2$, which is very close to the ideal formula of $Na_{2/3}Ni_{1/3}Mn_{2/3}O_2$. The lattice parameters and the chemical compositions of all samples are listed in Table 1. After ion exchange with Li, some Na remains and the chemical formula of the sample can be written as $Na_{0.0018}Li_{0.66}Ni_{0.33}Mn_{0.66}O_2$, which corresponds to 0.05 wt% Na for O3-$Li_{2/3}Ni_{1/3}Mn_{2/3}O_2$.

The XRD patterns of both O3- and $O3_{500}$-$Li_{2/3}Ni_{1/3}Mn_{2/3}O_2$ are assigned an almost single phase of the layered rock salt-type structure (space group of $R-3m$), as shown in Fig. 4-3-1. The c-axis length of the samples after ion exchange is much shorter than that of the precursor because the ionic radius of Li^+ (0.76 Å) is smaller than that of Na^+ (1.02 Å) [10], which leads to a reduced distance between $Ni_{1/3}Mn_{2/3}O_2$ layers [11]. A comparison of O3- and $O3_{500}$-$Li_{2/3}Ni_{1/3}Mn_{2/3}O_2$ XRD patterns shows a clear separation of Bragg diffraction lines for 018 and 110 in the as-prepared O3-phase. In the XRD pattern of $O3_{500}$-$Li_{2/3}Ni_{1/3}Mn_{2/3}O_2$, however, both diffraction lines merge into a single broad line, indicating that the ratio of lattice parameters (c/a) is close to 4.90, which is lower than that of the as-prepared O3-phase (Table 4-3-1) [12,13]. The cubic close-packed oxygen array of the rhombohedral structure approaches cubic symmetry [7]. As mentioned earlier, the stacking of oxide ions in both the layered rock salt- and spinel-type structures is equivalent and the only difference between the structures is the transition metal site [14]. The c-axis is shortened by the heat treatment; therefore, the local structure of the transition metal ions is presumed to be similar to the spinel-type structure.
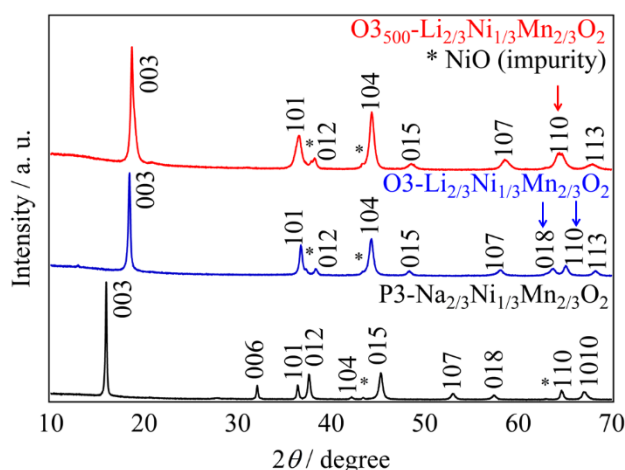
Figure 4-3-1. XRD patterns for the precursor (P3-$Na_{2/3}Ni_{1/3}Mn_{2/3}O_2$), O3-$Li_{2/3}Ni_{1/3}Mn_{2/3}O_2$, and $O3_{500}$-$Li_{2/3}Ni_{1/3}Mn_{2/3}O_2$. The "*" marks indicate NiO (impurity).

Table 4-3-1 The chemical compositions and lattice parameters for the $Na_{2/3}Ni_{1/3}Mn_{2/3}O_2$ and $Li_{2/3}Ni_{1/3}Mn_{2/3}O_2$ samples.

Sample	Composition	a / Å	c / Å	c / a
P3-$Na_{2/3}Ni_{1/3}Mn_{2/3}O_2$	$Na_{0.68}Ni_{0.33}Mn_{0.66}O_2$	2.8665(1)	16.781(1)	5.81
O3-$Li_{2/3}Ni_{1/3}Mn_{2/3}O_2$	$Li_{0.66}Na_{0.0018}Ni_{0.33}Mn_{0.66}O_2$	2.8666(1)	14.470(1)	5.05
O3$_{500}$-$Li_{2/3}Ni_{1/3}Mn_{2/3}O_2$		2.8855(2)	14.238(2)	4.93

Figure 4-3-2 shows the ^{6}Li-MAS-NMR spectra of O3- and O3$_{500}$-$Li_{2/3}Ni_{1/3}Mn_{2/3}O_2$. The O3-$Li_{2/3}Ni_{1/3}Mn_{2/3}O_2$ spectrum shows peaks at 1500 and 750 ppm, which suggests two types of Li sites in the structure [15]. A small and broad resonance at 1500 ppm is assigned to Li in a honeycomb-like arrangement of Mn ions (i.e., six Mn as the nearest neighbors) within the transition metal layer, as found in $Li[Li_{1/3}Mn_{2/3}]O_2$ (Li_2MnO_3) [16,17]. The 750-ppm peak is assigned to Li in the alkali layer of the layered rock salt structure [15]. On the other hand, in the case of O3$_{500}$-$Li_{2/3}Ni_{1/3}Mn_{2/3}O_2$, an additional peak at 925 ppm is observed, which should be related to the spinel-type structure [18]. It is believed that the spinel domains, which cannot be detected by XRD, are present.
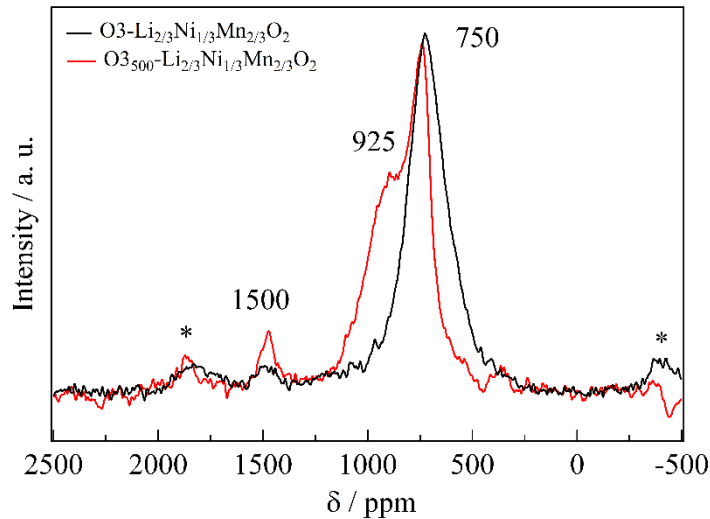
Figure 4-3-2. ^{6}Li-MAS-NMR spectra of O3-$Li_{2/3}Ni_{1/3}Mn_{2/3}O_2$ and O3$_{500}$-$Li_{2/3}Ni_{1/3}Mn_{2/3}O_2$ measured at room temperature. The "*" marks indicate spinning sidebands.

Figure 4-3-3a shows the charge/discharge curves of the O3-$Li_{2/3}Ni_{1/3}Mn_{2/3}O_2$ sample starting from Li extraction at 25 °C. Here, the voltage ranges between 2.0 and 4.8 V and the rate is 0.06 C. Two plateaus in the discharge curve are observed at around 4.2 and 3.0 V, as previously reported [2]. In the present Li/O3-$Li_{2/3}Ni_{1/3}Mn_{2/3}O_2$ cell, the resultant average discharge voltage is 3.41 V and the initial discharge capacity is 194 mA h g^{-1}, which is a higher capacity than that previously reported (170 mAh g^{-1}) [2]. This observation can be explained by the expansion of the voltage range between 2.5 and 4.4 V. This value is equivalent to 0.67 electron transfers per formula unit. Even after 10 cycles of charge/discharge, the discharge capacity remains at 184 mA h g^{-1} and its efficiency is 94.8%. Meanwhile, Zhao et al. did not observe two plateaus and the discharge capacity was large in the voltage range between 4.2 and

4.7 V [6]. It was presumed that the spinel phase was large due to a difference in ion exchange conditions.
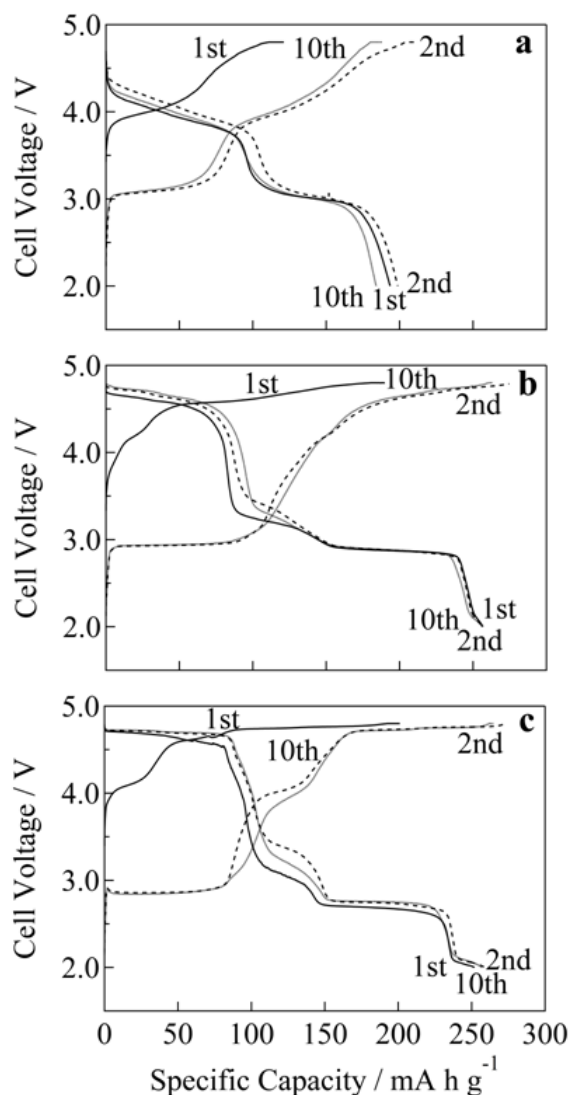

Figure 4-3-3. Charge and discharge curves for (a) $Li/O3\text{-}Li_{2/3}Ni_{1/3}Mn_{2/3}O_2$, (b) $Li/O3_{500}\text{-}Li_{2/3}Ni_{1/3}Mn_{2/3}O_2$ and (c) $Li/O3_{700}\text{-}Li_{2/3}Ni_{1/3}Mn_{2/3}O_2$ cells.

Figure 4-3-3b shows the charge/discharge curves of the $Li/O3_{500}\text{-}Li_{2/3}Ni_{1/3}Mn_{2/3}O_2$ cell. The charge and discharge capacities are confirmed at a high-potential region of around 4.8 V (about 80 mA h g^{-1}). The spinel phase transition is expected to occur at temperatures higher than 260 °C; therefore, the heat treatment stabilizes the crystal structure and improves the electrochemical properties such as cycle performance and initial capacity. This corresponds with the results of the ^6Li-MAS-NMR spectrum of $O3_{500}\text{-}Li_{2/3}Ni_{1/3}Mn_{2/3}O_2$, because the spinel phase is increased (Fig. 4-3-2). In addition, a gradually sloping profile between 3.0 and 4.8 V, which is estimated to correspond to the layered rock salt, is observed here. The average discharge voltage for this cell is 3.21 V, and the initial discharge capacity is 257 mA h g^{-1}. This value corresponds to 0.90 electron transfers per formula unit, i.e., the initial discharge capacity is successfully improved. The discharge capacity at the 3.0 V plateau region in $O3_{500}\text{-}Li_{2/3}Ni_{1/3}Mn_{2/3}O_2$ (about

80 mA h g^{-1}) is improved to twice that in the as-prepared O3-Li$_{2/3}$Ni$_{1/3}$Mn$_{2/3}$O$_2$ (about 40 mA h g^{-1}). The average discharge voltage (3.21 V) is lower than that in the Li/O3-Li$_{2/3}$Ni$_{1/3}$Mn$_{2/3}$O$_2$ cell (3.41 V), although even after 10 cycles of charge/discharge, the capacity remains at 256 mA h g^{-1} and its efficiency is 99.6%.

Figure 4-3-3c shows the charge/discharge curves of the Li/O3$_{700}$-Li$_{2/3}$Ni$_{1/3}$Mn$_{2/3}$O$_2$ cell, in which the electrode shows good reversibility. The average discharge voltage for this cell is 3.03 V, and the initial discharge capacity is 252 mA h g^{-1}. The cell voltage in the 3.0 V region is lower than that in the Li/O3$_{500}$-Li$_{2/3}$Ni$_{1/3}$Mn$_{2/3}$O$_2$ cell, although it is higher in the 4.8 V region. The discharge curve gradually changes in shape from two to three distinct plateaus in comparison with the Li/O3$_{500}$-Li$_{2/3}$Ni$_{1/3}$Mn$_{2/3}$O$_2$ cell. In particular, Li/O3$_{700}$-Li$_{2/3}$Ni$_{1/3}$Mn$_{2/3}$O$_2$ has a distinct plateau in the 2.0 V region.

Figure 4-3-4 shows the c/a ratio and initial discharge capacity for whole samples versus the heat treatment temperature. The 4.8 V plateau region is observed in all of the heat-treated O3-Li$_{2/3}$Ni$_{1/3}$Mn$_{2/3}$O$_2$ samples. This is consistent with the spinel phase, which is generated above 300 °C [7]. The c/a ratio is close to 4.90 in all of the heat-treated O3-Li$_{2/3}$Ni$_{1/3}$Mn$_{2/3}$O$_2$ samples (Table 4-3-1). The discharge capacity rapidly increases by more than 260 °C, which is the ion exchange temperature. Charge and discharge curves for the Li/O3$_{300}$-Li$_{2/3}$Ni$_{1/3}$Mn$_{2/3}$O$_2$ cell are nearly consistent with those previously reported [6].
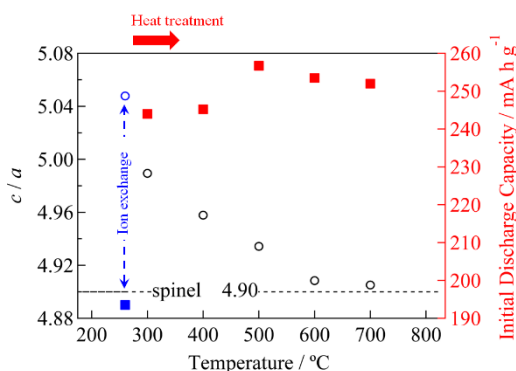
Figure 4-3-4. Charge and discharge curves for (a) Li/O3-Li$_{2/3}$Ni$_{1/3}$Mn$_{2/3}$O$_2$, (b) Li/O3$_{500}$-Li$_{2/3}$Ni$_{1/3}$Mn$_{2/3}$O$_2$ and (c) Li/O3$_{700}$-Li$_{2/3}$Ni$_{1/3}$Mn$_{2/3}$O$_2$ cells.

The discharge capacity improves by increasing the treatment temperature to 500 °C. The maximum discharge capacity and c/a ratio values occur at 500 °C (except for 260 °C, which is the ion exchange temperature). Above 500 °C, the discharge capacity and c/a ratio become constant as about 250 mA h g^{-1} and 4.90, respectively. The discharge curve gradually changes in shape from two to three distinct plateaus. Although the discharge capacity at the 3 V plateau region gradually decreases as the heating temperature increases above 500 °C, the discharge capacity at the 2 V plateau region increases. The change in the O3-Li$_{2/3}$Ni$_{1/3}$Mn$_{2/3}$O$_2$ crystal structure by increasing the treatment temperature from 300 to 700 °C may cause a rearrangement of Li ions in the layer space.

Section IV-IV   Conclusions

   The synthesis processes and electrochemical properties of lithium nickel manganese oxide, $O3$-$Li_{2/3}Ni_{1/3}Mn_{2/3}O_2$, with a layered rock salt-type structure, were examined after a series of different heat treatments (300–700 °C). A novel 5V class plateau region was observed in all thermally treated $O3$-$Li_{2/3}Ni_{1/3}Mn_{2/3}O_2$ cells. These cells showed good charge-discharge performances with an average discharge voltage of 3.0–3.2 V and initial capacities of 240–260 mA h g^{-1} between 2.0 and 4.8 V. In particular, the sample treated at 500 °C ($O3_{500}$-$Li_{2/3}Ni_{1/3}Mn_{2/3}O_2$) displayed a gradually sloping profile between 3.0 and 4.8 V. These performances may be attributed to the retention of the original layered rock salt-type structure. Accordingly, it is clearly confirmed in the present study that thermal treatment of the $O3$-$Li_{2/3}Ni_{1/3}Mn_{2/3}O_2$ material is interesting not only for its good cycle performance, but also for its high voltage and high capacity.

Reference

[1] J.M. Paulsen, C.L. Thomas, J.R. Dahn, *J. Electrochem. Soc*., **147** (2000) 861.

[2] J.M. Paulsen, J.R. Dahn, *J. Electrochem. Soc*., **147** (2000) 2478.

[3] J.M. Paulsen, D. Larcher, J.R. Dahn, *J. Electrochem. Soc*., **147** (2000) 2862.

[4] Z. Lu, R.A. Donaberger, J.R. Dahn, *Chem. Mater*., **12** (2000) 3583.

[5] S. Komaba, K. Yoshii, A. Ogata, I. Nakai, *Electrochim. Acta*, **54** (2009) 2353.

[6] W. Zhao, S. Harada, Y. Furuya, S. Yamamoto, H. Noguchi, *J. Power Sources*, **261** (2014) 324.

[7] N. Yabuuchi, Y.T. Kim, H.H. Li, Y. Shao-Horn, *Chem. Mater*., **20** (2008) 4936.

[8] N. Ishida, H. Hayakawa, J. Akimoto, H. Shibuya, J. Imaizumi, *J. Power Sources*, **244** (2013) 505.

[9] Topas V4: General Profile and Structure Analysis Software for Powder Diffraction Data, Bruker AXS, Karlsruhe, Germany, 2008.

[10] R.D. Shannon, *Acta Crystallogr*., **A32** (1976) 751.

[11] K. Chiba, N. Kijima, Y. Takahashi, Y. Idemoto, J. Akimoto, *Solid State Ionics*, **178** (2008) 1725.

[12] E. Rossen, J.N. Reimers, J.R. Dahn, *Solid State Ionics*, **62** (1993) 53.

[13] R.J. Gummow, D.C. Liles, M.M. Thackeray, *Mat. Res. Bull.*, **28** (1993) 235.

[14] H. Ben Yahia, M. Shikano, H. Kobayashi, *Chem. Mater*., **25** (2013) 3687.

[15] J. Cabana, N.A. Chernova, J. Xiao, M. Roppolo, K.A. Aldi, M.S. Whittingham, C.P. Grey, *Inorg. Chem*., **52** (2013) 8540.

[16] P. Mustarelli, V. Massarotti, M. Bini, D. Capsoni, *Phys. Rev. B,* **55** (1997) 12018.

[17] J. Bréger, M. Jiang, N. Dupré, Y.S. Meng, Y.S. Horn, G. Ceder, C.P. Grey, *J. Solid State Chem*., **178** (2005) 2575.

[18] Y. J. Lee, C. Eng, C.P. Grey, *J. Electrochem. Soc*., **148** (2001) A249.

Chapter V

Sodium lithium nickel manganese oxide

$Na_xLi_{0.67-x}Ni_{0.33}Mn_{0.67}O_2$

－Control of the ratio of layered rock-salt and spinel structure

by residual Na content－

Section IV-I   Introduction

A lithium-deficient nickel manganese oxide $Li_{0.67}Ni_{0.33}Mn_{0.67}O_2$ with a layered structure (O2 and O3 type) has been extensively investigated as a positive electrode material for use in rechargeable lithium batteries [1–7]. Paulsen et al. [1-3] have reported battery performances such as superior cycling performance and discharge capacity of approximately 170 mA h g^{-1} between 4.6 and 2.5 V for $O2\text{-}Li_{0.67}Ni_{0.33}Mn_{0.67}O_2$. On the other hand, $O3\text{-}Li_{0.67}Ni_{0.33}Mn_{0.67}O_2$ exhibits a discharge capacity of approximately 200 mA h g^{-1} between 4.7 and 2.5 V, which is higher than that of the O2-type compound. However, $O3\text{-}Li_{0.7}Ni_{0.33}Mn_{0.67}O_2$ exhibits poor capacity retention on subsequent cycling, due to phase transformation from layered to spinel structure [1–3]. The oxygen array of the O3-type structure is very similar to that of the spinel structure; hence, a direct phase transition is often observed between them, while the O2-type structure does not exhibit such a phase transition and is very stable [1–4]. The poor capacity retention observed for $O3\text{-}Li_{0.67}Ni_{0.33}Mn_{0.67}O_2$ indicates that electrochemical cycling induces the phase transition to the spinel structure [2].

We reported that a thermal treatment after the ion-exchange reaction using a molten salt improved the charge–discharge performance of $O3\text{-}Li_{0.67}Ni_{0.33}Mn_{0.67}O_2$ [7]. When $O3\text{-}Li_{0.67}Ni_{0.33}Mn_{0.67}O_2$ was heated at 500 °C, it exhibits a 5 V class plateau in its charge–discharge voltage-capacity curves. Furthermore, a large discharge capacity of 257 mA h g^{-1} was reported between 2.0 and 4.8 V. Thermal treatment for $O3\text{-}Li_{0.67}Ni_{0.33}Mn_{0.67}O_2$ is extremely interesting as it affords better cycle performance, a higher discharge voltage and specific capacity than as-prepared $O3\text{-}Li_{0.67}Ni_{0.33}Mn_{0.67}O_2$. However, the experimentally demonstrated discharge voltage-capacity curve drastically decreases between 3.0 and 4.8 V because the spinel phase content increases as a result of heat treatment [7]. Recently, a 5 wt% Na-doped NMC ($0.3Li_2MnO_3\text{-}0.7Li_{0.97}Na_{0.03}Mn_{0.33}Ni_{0.33}Co_{0.33}O_2$) has been reported to suppress the spinel transition [8]. Hence, a of the Na contents can improve the charge–discharge performance.

Inspired by the preliminary studies, in this study we sought to synthesize $Na_xLi_{0.67}Ni_{0.33}Mn_{0.67}O_2$ by thermal treatment. The residual Na content x in ion exchange is utilized to clarify the impact of the charge and discharge voltage-capacity curves for thermally treated $Na_xLi_{0.67}Ni_{0.33}Mn_{0.67}O_2$ and the results obtained can be utilized in the design of high-capacity materials.

Section IV-II   Experiment

IV-II-I   Synthesis

The precursor P3-$Na_{0.67}Ni_{0.33}Mn_{0.67}O_2$, was synthesized via a direct solid-state reaction from stoichiometric mixtures of CH_3COONa (98.5% pure), $Ni(OH)_2$ (99.9% pure), and Mn_2O_3 (99.9% pure), with 3% excess Na [7]. First, the weighed powder was mixed through ball milling, and then pressed into pellets. Second, the pellet was heated at 650 °C under an O_2 flow to obtain pure phase of P3 for 10 h and then pulverized. For Na^+/Li^+ exchange, the host material P3-$Na_{0.67}Ni_{0.33}Mn_{0.67}O_2$ was first added to 0.5, 2.0, and 4.0-fold excess of lithium as a solution of LiBr in MeOH at 110 °C for 6 h. Finally, the ion-exchanged powder was filtered, washed with MeOH, and then dried at 90 °C overnight [9].

To induce a change in the crystal structure, the samples were heated at 500 °C for 5 h in air. Hereafter, the thermally treated $Na_xLi_{0.67-x}Ni_{0.33}Mn_{0.67}O_2$ will be referred to as HT-$Na_xLi_{0.67-x}Ni_{0.33}Mn_{0.67}O_2$ for brevity reasons.

IV-II-II   Characterization

The phase purity and crystal structure of the samples were determined by powder X-ray diffraction (XRD) using a D8 ADVANCE diffractometer (Bruker AXS) with a Cu Kα radiation source (operating conditions: 40 kV, 55 mA). XRD intensity data were collected for 0.5 s in steps of 0.02° over a 2θ range of 10°–70°. TOPAS Ver. 4.2 software package was used for Pawley analysis [10].

The cationic composition (e.g., Li, Na, Ni and Mn contents) was determined by inductively coupled plasma-atomic emission spectroscopy (Shimadzu ICPS-8000).

A Titan3 G2 60-300 scanning transmission electron microscope (STEM, FEI), equipped with a Super-X (Bruker) detector for energy-dispersive X-ray spectroscopy (EDS), was employed at an accelerating voltage of 300 kV. The sample powder was directly dispersed on a carbon film supported by a Cu mesh.

Electrochemical measurements were performed using coin-type cells (CR2032). Working electrodes were prepared using 10 mg of active materials, 10 mg of acetylene black as the conductive agent, and 2 mg of polytetrafluoroethylene (PTFE) as the binder. An Al mesh was used as the current collector, and the electrode diameter was 14 mm. A circular Li foil, having a diameter of 16 mm and a thickness of 0.2 mm, was used as the counter electrode. A microporous polypropylene sheet was used as the separator. A 1 M $LiPF_6$ solution in a 1:2 (v/v) mixture of ethylene carbonate and diethyl carbonate was used as the electrolyte. Cells were constructed in a dry room with a dew point below −50 °C, and electrochemical measurements were conducted with a current density of 15 mA g^{-1} (19 mA cm^{-2}) at 25 °C after standing overnight under open-circuit conditions.

Section V-III   Results and Discussion

V-III-I   Structural characterization

Table 1 shows the chemical compositions of all ion-exchanged samples. The control of the residual Na content x was successfully carried out by adjusting the LiBr concentration.

Table 1 Chemical composition of the ion-exchanged samples.

LiBr concentration	Na	Li	Ni	Mn
0.5-fold lithium excess	0.25	0.42	0.33	0.67
2.0-fold lithium excess	0.093	0.57	0.33	0.67
4.0-fold lithium excess	0.034	0.64	0.33	0.67

Figure 5-3-1-1a shows the XRD patterns of the as-prepared P3-$Na_{0.67}Ni_{0.33}Mn_{0.67}O_2$ and ion-exchanged $Na_xLi_{0.67-x}Ni_{0.33}Mn_{0.67}O_2$. In the XRD pattern of $Na_{0.25}Li_{0.42}Ni_{0.33}Mn_{0.67}O_2$ and $Na_{0.093}Li_{0.57}Ni_{0.33}Mn_{0.67}O_2$, one new peak was observed at 17.0°, attributed to the main 002 diffraction peak of the OP2 phase owing to the analogy of the phase transformation from P3-$Na_{0.67}Ni_{0.33}Mn_{0.67}O_2$ [11]. Upon increasing the Li content, the OP2 phase transformed to the O3 phase by a two-phase coexistence state of OP2 and O3. The presence of such an intermediate phase has also been reported for $Na_{0.19}Li_{0.66}Ni_{0.5}Mn_{0.5}O_2$ and $Na_{0.29}Li_{0.53}Ni_{0.5}Mn_{0.5}O_2$ [12]. Here, a layered structure based on the stacking of $Ni_{0.33}Mn_{0.67}O_2$ was maintained. The c-axis length of the sample after the ion-exchange reaction was significantly shorter than that of the precursor because the ionic radius of Li^+ (0.76 Å) is smaller than that of Na^+ (1.02 Å) [13]; that is, the distance between $Ni_{0.33}Mn_{0.67}O_2$ layers decreased with the decrease of x [2,4,7].
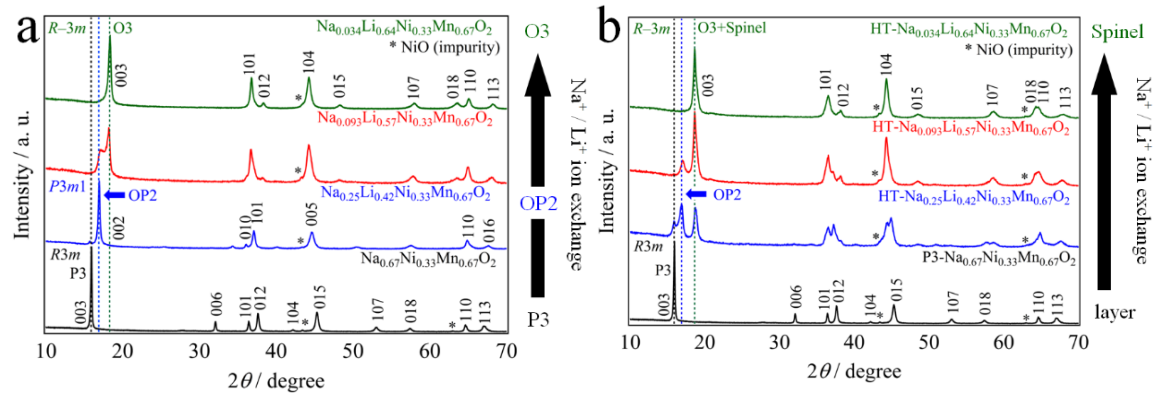
Figure 5-3-1-1. (a) XRD patterns of the as-prepared P3-$Na_{0.67}Ni_{0.33}Mn_{0.67}O_2$ and ion-exchanged O3-$Na_xLi_{0.67-x}Ni_{0.33}Mn_{0.67}O_2$ (x = 0.25, 0.093 and 0.034). (b) XRD patterns of the as-prepared P3-$Na_{0.67}Ni_{0.33}Mn_{0.67}O_2$ and thermally treated HT-$Na_xLi_{0.67-x}Ni_{0.33}Mn_{0.67}O_2$ (x = 0.25, 0.093, and 0.034).

As shown in Fig. 5-3-1-1b, the XRD patterns of HT-$Na_xLi_{0.7-x}Ni_{0.33}Mn_{0.67}O_2$ were assigned as almost pure phases of the layered and spinel type structure. Some very weak peaks, assigned to rock-salt-type NiO, were observed. Upon increasing the Li content, the four-phase coexistence state of P3, OP2, O3, and spinel in HT-$Na_{0.25}Li_{0.42}Ni_{0.33}Mn_{0.67}O_2$ was transformed to the two-phase coexistence state of O3 and spinel in HT-$Na_{0.034}Li_{0.64}Ni_{0.33}Mn_{0.67}O_2$. For

$Na_{0.034}Li_{0.64}Ni_{0.33}Mn_{0.67}O_2$, a clear separation was observed for the 018 and 110 Bragg diffraction peaks (Fig. 5-3-1-1a), while as for HT-$Na_{0.034}Li_{0.64}Ni_{0.33}Mn_{0.67}O_2$ (Fig. 5-3-1-1b), both diffraction lines merged into a single broad diffraction line. This change indicates that after thermal treatment, the cubic-close-packed oxygen array of the rhombohedral structure approaches cubic symmetry [14]. The ratio of lattice parameters c/a for HT-$Na_{0.034}Li_{0.64}Ni_{0.33}Mn_{0.67}O_2$ is 4.93, which is very close to the ideal value of the spinel phase (4.90) [15–16]. As mentioned above, the stacking of the oxide ions in both the layered rock-salt- and spinel-type structure is equivalent, and the only difference between the structures is the TM site [17]. The c-axis was shortened through heat treatment; hence, the site coordination of the TM ions is presumed to be similar to that of the spinel-type structure. Recently, a 5 wt% Na-doped NMC ($0.3Li_2MnO_3$-$0.7Li_{0.97}Na_{0.03}Mn_{0.33}Ni_{0.33}Co_{0.33}O_2$) has been reported to suppress spinel transition [8]. Hence, the control of the Na contents can suppress the spinel transition.
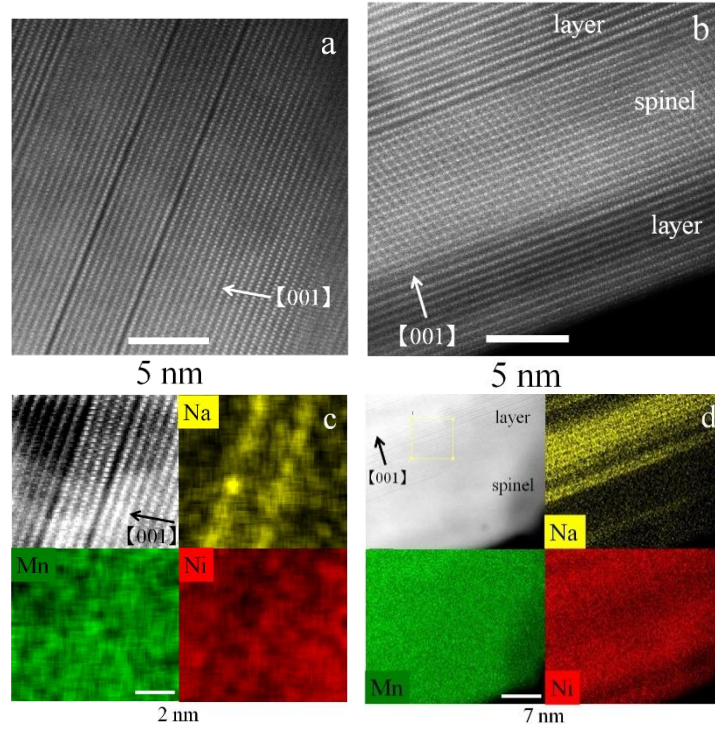
Figure 5-3-1-2. ADF-STEM images of (a) $Na_{0.093}Li_{0.57}Ni_{0.33}Mn_{0.67}O_2$ and (b) HT-$Na_{0.093}Li_{0.57}Ni_{0.33}Mn_{0.67}O_2$. EDS mapping of (c) $Na_{0.093}Li_{0.57}Ni_{0.33}Mn_{0.67}O_2$ and (d) HT-$Na_{0.093}Li_{0.57}Ni_{0.33}Mn_{0.67}O_2$.

Figures 5-3-1-2a and 5-3-1-2b show annular dark-field (ADF) STEM images of $Na_{0.093}Li_{0.57}Ni_{0.33}Mn_{0.67}O_2$ and HT-$Na_{0.093}Li_{0.57}Ni_{0.33}Mn_{0.67}O_2$, respectively. $Na_{0.093}Li_{0.57}Ni_{0.33}Mn_{0.67}O_2$ exhibited a layered structure with two different interlayer distances (Fig. 5-3-1-2a). The presence of residual Na should increase the interlayer distance; hence, the shorter distance corresponds to the Li layer. On the other hand, both layered and spinel structures were observed for HT-$Na_{0.093}Li_{0.57}Ni_{0.33}Mn_{0.67}O_2$ (Fig. 5-3-1-2b). As shown in Fig. 5-3-1-2c, EDS mapping proved that the longer distance corresponds to the Na layer. As shown in Fig. 5-3-1-2d, residual Na was detected at the interlayer, while Na was very minimal in the regions with the spinel structure.

Figure 5-3-1-3 shows a schematic of the mechanism for the spinel phase transition. Li occupies the center of the O_6 octahedron, while Na occupies the center of trigonal prismatic O_6 site. Hence, the precursor $Na_{0.67}Ni_{0.33}Mn_{0.67}O_2$ and ion-exchanged $Li_{0.67}Ni_{0.33}Mn_{0.67}O_2$ exhibit P3- and O3-type structures, respectively. As TM also occupies the center of the O_6 octahedron, TM easily migrates to the Li site; that is, it is difficult for TM to be moved to the Na site because of different oxygen coordination environments. As a result, the Na phases maintain the layered structure, and the Li phases easily transform to the spinel phase as mentioned above. A similar phenomenon has been reported for the Na (de)intercalation of $LiMn_2O_4$ [18].
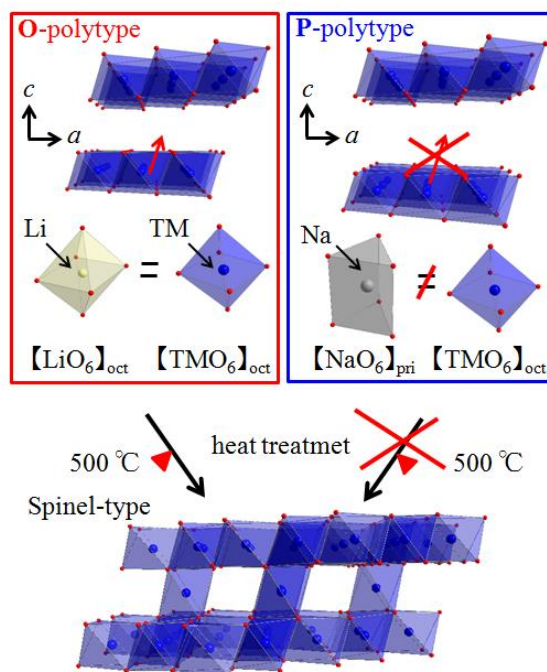
Figure 5-3-1-3. Schematic of polytypic phase transformation induced by thermal treatment of $Na_{0.093}Li_{0.57}Ni_{0.33}Mn_{0.67}O_2$.

V-III-II   Electrochemical properties

Figure 5-3-2-1a shows the initial charge and discharge curves of HT-$Na_xLi_{0.67-x}Ni_{0.33}Mn_{0.67}O_2$ starting from charging in the voltage range between 2.0 and 4.8 V, at a current density of 15 mA g^{-1}, and a temperature of 25 °C. Both charge and discharge curves of all samples exhibited a plateau at around 4.8 V, as has been previously reported for O3$_{500}$-$Li_{0.66}Na_{0.0018}Ni_{0.33}Mn_{0.66}O_2$ [7]. The initial charge capacity increased from 162 mA h g^{-1} (x = 0.25) to 188 mA h g^{-1} (x = 0.034) with decrease in the residual Na content x. HT-$Na_{0.034}Li_{0.64}Ni_{0.33}Mn_{0.67}O_2$ exhibited a maximum discharge capacity of 266 mA h g^{-1}. Furthermore, the shape of the discharge curve also changed from a profile with two distinct plateau to a gradually sloping profile with increase in the residual Na content. The average discharge voltage increased from 3.22 to 3.74 V with increase in the residual Na content x. HT-$Na_xLi_{0.67-x}Ni_{0.33}Mn_{0.67}O_2$ exhibited a maximum discharge energy density of 943 W h kg^{-1} (x = 0.093). The discharge capacity at around the 3 V plateau region of approximately 30 mA h g^{-1} (x = 0.25) was increased to approximately 60 mA h g^{-1} (x = 0.034) for HT-$Na_xLi_{0.67-x}Ni_{0.33}Mn_{0.67}O_2$ compounds. This is consistent with the increase in the spinel phase

with decrease in the residual Na content. Figure 5-3-2-1b shows the cycle performance of HT-Na$_x$Li$_{0.67-x}$Ni$_{0.33}$Mn$_{0.67}$O$_2$. The discharge capacity retention of HT-Na$_x$Li$_{0.7-x}$Ni$_{0.33}$Mn$_{0.67}$O$_2$ increased from 79 to 83 % at 50 cycles with increasing Na content x.
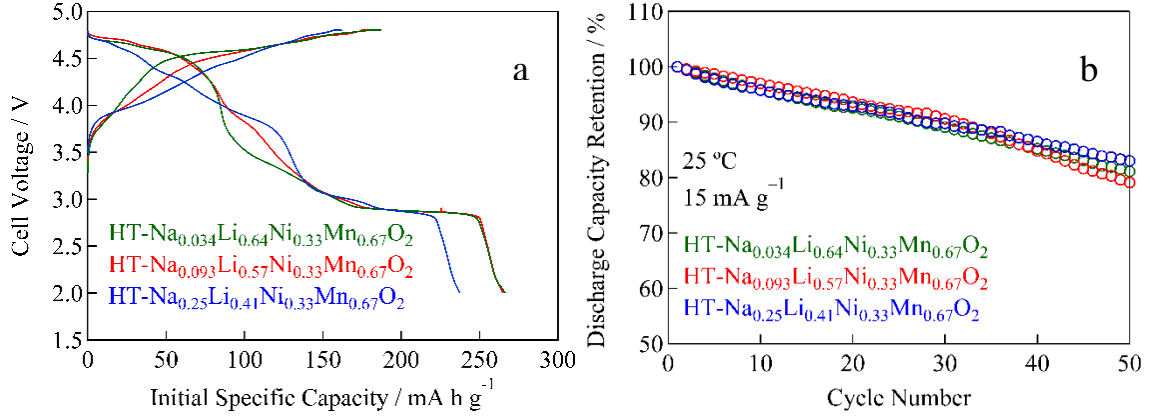

Figure 5-3-2-1. Initial charge and discharge curves for (a) Li/HT-Na$_x$Li$_{0.67-x}$Ni$_{0.33}$Mn$_{0.67}$O$_2$ (x = 0.25, 0.093, and 0.034) cells at a rate of 15 mA g^{-1} in the voltages ranging from 2.0 V to 4.8 V at 25 ^{o}C. Note that the as-prepared sample is Li-deficient sample; therefore, the initial charge capacity is lower than the discharge capacity. Cycle performance for (b) Li/HT-Na$_x$Li$_{0.67-x}$Ni$_{0.33}$Mn$_{0.67}$O$_2$ (x = 0.25, 0.093, and 0.034) cells.

As mentioned above, the (dis)charge curves of HT-Na$_x$Li$_{0.67-x}$Ni$_{0.33}$Mn$_{0.67}$O$_2$ ($0.03 < x \leq 0.25$) varied with the residual Na content x. All phenomena can be associated with the generation of the spinel phase. With a higher residual Na content x, the P-type Na–O coordination suppressed the spinel-phase transformation (Fig. 5-3-1-3). In other words, from a crystallographic viewpoint, the increase in the residual Na content x curtails the formation of the spinel phase, which is reflected by the disparate initial charge and discharge voltage profiles. In HT-Na$_x$Li$_{0.67-x}$Ni$_{0.33}$Mn$_{0.67}$O$_2$ ($0.03 < x \leq 0.25$), the residual Na content x can be adjusted to modify the capacity-voltage responses for various power applications.

Section V-IV   Conclusions

$Na_xLi_{0.67-x}Ni_{0.33}Mn_{0.67}O_2$ ($0.03 < x \leq 0.25$) was prepared as a new class of high-voltage and high-capacity positive electrode materials for rechargeable lithium batteries. In particular, HT-$Na_xLi_{0.67-x}Ni_{0.33}Mn_{0.67}O_2$ ($x = 0.093$) exhibited a maximum (dis)charge capacity of 261 mA h g^{-1} at an average voltage of 3.36 V at 25 °C, translating to an energy density of 943 W h kg^{-1}. The attained performance is attributed to the predominant retention of the layered rock-salt structure over the spinel phase. Thus, the spinel-phase transformation can be curtailed by the variation of the residual Na in the compositions of HT-$Na_xLi_{0.67-x}Ni_{0.33}Mn_{0.67}O_2$ ($0.03 < x \leq 0.25$), demonstrating the feasibility of modifying the capacity–voltage characteristics through a judicious control of the constituent Na content in related compositions.

Reference

[19] J. M. Paulsen, C. L. Thomas, J. R. Dahn, *J. Electrochem. Soc*., **147** (2000) 861.

[20] J. M. Paulsen, J. R. Dahn, *J. Electrochem. Soc*., **147** (2000) 2478.

[21] J. M. Paulsen, D. Larcher, J. R. Dahn, *J. Electrochem. Soc*., **147** (2000) 2862.

[22] Z. Lu, R. A. Donaberger, J. R. Dahn, *Chem. Mater*., **12** (2000) 3583.

[23] S. Komaba, K. Yoshii, A. Ogata, I. Nakai, *Electrochim. Acta*, **54** (2009) 2353.

[24] W. Zhao, S. Harada, Y. Furuya, S. Yamamoto, H. Noguchi, *J. Power Sources*, **261** (2014) 324.

[25] K. Chiba, M. Shikano, H. Sakaebe, *J. Power Sources*, **304** (2016) 60.

[26] M. N. Ates, Q. Jia, A. Shah, A. Busnaina, S. Mukerjee, K. M. Abraham, *J. Electrochem Soc*., **161** (2014) A290.

[27] N. Ishida, H. Hayakawa, H. Shibuya, J. Imaizumi, J. Akimoto, *J. Power Sources*, **244** (2013) 505.

[28] Topas V4: General Profile and Structure Analysis Software for Powder Diffraction Data, Bruker AXS, Karlsruhe, Germany, 2008.

[29] N. Yabuuchi, M. Kajiyama, J. Iwatate, H. Nishikawa, S. Hitomi, R. Okuyama, R. Usui, Y. Yamada, S. Komaba, *Nat. Mater*., **11** (2012) 512.

[30] H. Gwon, S. W. Kim, Y. U. Park, J. Hong, G. Ceder, S. Jeon, K. Kang, *Inorg. Chem*., **53** (2014) 8083.

[31] R. D. Shannon, *Acta Crystallogr*., **A32** (1976) 751.

[32] N. Yabuuchi, Y. T. Kim, H. H. Li, Y. Shao-Horn, *Chem. Mater.*, **20** (2008) 4936.

[33] R. J. Gummow, D. C. Liles, M. M. Thackeray, *Mat. Res. Bull.*, **28** (1993) 235.

[34] E. Rossen, J. N. Reimers, J. R. Dahn, *Solid State Ionics*, **62** (1993) 53.

[35] H. B. Yahia, M. Shikano, H. Kobayashi, *Chem. Mater*., **25** (2013) 3687.

[36] N. Yabuuchi, M Yano, S. Kuze, S. Komaba, *Electrochimica Acta*, **82** (2012) 296.

Chapter VI

Lithium nickel manganese oxide $Li_{0.7}Ni_{1-y}Mn_yO_2$

$-$Control of the ratio of

layered rock-salt and spinel structure by Ni/Mn ratio$-$

Section VI-I Introduction

A lithium-deficient nickel manganese oxide $Li_{0.7}Ni_{0.33}Mn_{0.67}O_2$ with a layered structure (O2 and O3 type) has been extensively investigated as a positive electrode material for use in rechargeable lithium batteries [1–7]. Paulsen et al. [1-3] have reported battery performances such as superior cycling performance and discharge capacity of approximately 170 mA h g^{-1} between 4.6 and 2.5 V for $O2\text{-}Li_{0.7}Ni_{0.33}Mn_{0.67}O_2$. On the other hand, $O3\text{-}Li_{0.7}Ni_{0.33}Mn_{0.67}O_2$ exhibits a discharge capacity of approximately 200 mA h g^{-1} between 4.7 and 2.5 V, which is higher than that of the O2-type compound. However, $O3\text{-}Li_{0.7}Ni_{0.33}Mn_{0.67}O_2$ exhibits poor capacity retention on subsequent cycling, due to phase transformation from layered to spinel structure [1–3]. The oxygen array of the O3-type structure is very similar to that of the spinel structure; hence, a direct phase transition is often observed between them, while the O2-type structure does not exhibit such a phase transition and is very stable [1–3]. The poor capacity retention observed for $O3\text{-}Li_{0.7}Ni_{0.33}Mn_{0.67}O_2$ indicates that electrochemical cycling induces the phase transition to the spinel structure.

We reported that a thermal treatment after the ion-exchange reaction using a molten salt improved the charge–discharge performance of $O3\text{-}Li_{0.7}Ni_{0.33}Mn_{0.67}O_2$ [7]. When $O3\text{-}Li_{0.7}Ni_{0.33}Mn_{0.67}O_2$ was heated at 500 °C, it exhibits a 5 V class plateau in its charge–discharge voltage-capacity curves. Furthermore, a large discharge capacity of 257 mA h g^{-1} was reported between 2.0 and 4.8 V. Thermal treatment for $O3\text{-}Li_{0.7}Ni_{0.33}Mn_{0.67}O_2$ is extremely interesting as it affords better cycle performance, a higher discharge voltage and specific capacity than as-prepared $O3\text{-}Li_{0.7}Ni_{0.33}Mn_{0.67}O_2$. However, the experimentally demonstrated discharge voltage-capacity curve drastically decreases between 3.0 and 4.8 V because the spinel phase content increases as a result of heat treatment [7]. Recently, spinel-phase $LiNiMnO_4$ ($Li_{0.5}Ni_{0.5}Mn_{0.5}O_2$) has been reported to be unstable [8]. Hence, a control of the Mn content can improve the charge–discharge performance.

Inspired by the preliminary studies, in this study we sought to synthesize $Li_{0.7}Ni_{1-y}Mn_yO_2$ ($0.5 \leq y \leq 0.8$) by thermal treatment. The Mn content y is utilized to clarify the impact of the charge and discharge voltage-capacity curves for thermally treated $Li_{0.7}Ni_{1-y}Mn_yO_2$ ($0.5 \leq y \leq 0.8$) and the results obtained can be utilized in the design of high-capacity materials.

Section VI-II Experiment

VI-II-I Synthesis

The precursor P3-$Na_{0.7}Ni_{1-y}Mn_yO_2$ (y = 0.67 and 0.80) was synthesized by a direct solid-state reaction from stoichiometric mixtures of CH_3COONa (98.5% pure), $Ni(OH)_2$ (99.9% pure) and Mn_2O_3 (99.9% pure) with 3% excess sodium [1,3,7]. First, the weighed powder was mixed by ball milling and then pressed into a pellet. Second, the pellet was heated at 650 °C under an O_2 flow to obtain pure phase of P3 for 10 h and then pulverized.

The starting material of O3-$NaNi_{0.5}Mn_{0.5}O_2$ was synthesized by a direct solid-state reaction of stoichiometric mixtures of CH_3COONa, $Ni(OH)_2$ and Mn_2O_3 with 5% excess sodium [9]. First, the weighed powder was pelletized and heated at 800 °C for 20 h in air. Second, the heated pellet was quenched in liquid N_2 and then pulverized. Third, P3-$Na_{0.7}Ni_{0.5}Mn_{0.5}O_2$ precursor was prepared by chemical oxidation. O3-$NaNi_{0.5}Mn_{0.5}O_2$ was oxidized with 0.01 M iodine in an acetonitrile solution for 4 h at 25 °C [10]. Finally, the oxidized powder was filtered, washed with acetonitrile, and then dried at 90 °C overnight.

For Na^+/Li^+ exchange, the host material P3-$Na_{0.7}Ni_{1-x}Mn_xO_2$ was refluxed with 4.0-fold lithium excess amount of a solution of LiBr in MeOH [11]. Finally, the ion-exchanged powder was filtered, washed with MeOH, and then dried at 90 °C overnight.

To induce a change in the crystal structure, the samples were heated at 500 °C for 5 h in air. Hereafter, the thermally treated $Li_{0.7}Ni_{1-y}Mn_yO_2$ ($0.5 \leq y \leq 0.8$) will be referred to as HT-$Li_{0.7}Ni_{1-y}Mn_yO_2$.

VI-II-II Characterization

The phase purity and crystal structure of the samples were determined by powder X-ray diffraction (XRD) using a D8 ADVANCE diffractometer (Bruker AXS) with a Cu Kα radiation source (operating conditions: 40 kV, 55 mA). XRD intensity data were collected for 0.5 s in steps of 0.02° over a 2θ range of 10°–70°. TOPAS Ver. 4.2 software package was used for Pawley analysis [12].

The cationic composition (e.g., Li, Na, Ni and Mn contents) was determined by inductively coupled plasma-atomic emission spectroscopy (Shimadzu ICPS-8000).

The solid-state ^6Li magic-angle spinning nuclear magnetic resonance (^6Li MAS-NMR) spectra of the samples were recorded at room temperature using an AVANCE 300 spectrometer (Bruker) at 44 MHz with a spinning rate of 50 kHz for Li nuclei by a rotor-synchronized spin-echo pulse sequence. The pulse width was 3.6 μs (π/2 pulse). The chemical shift was recorded relative to a 1.0 M ^6LiCl aqueous solution. ^6Li spectral decomposition was performed using the Dmfit software, which allows for the variation of peak position, peak height, line width, and the ratio of Gaussian to Lorentzian functions [13].

Thermogravimetric analysis (TGA) was performed on a Q5000IR apparatus (TA Instruments). The experiments were carried out by heating the sample (approximately 15 mg) from 50 to 900 °C at 20 °C min^{-1} under air. The samples were cooled from 900 to 50 °C at 1 °C min^{-1} under air.

Electrochemical measurements were performed using coin-type cells (CR2032). Working electrodes were prepared using 10 mg of active materials, 10 mg of acetylene black as the conductive agent, and 2 mg of polytetrafluoroethylene (PTFE) as the binder. An Al mesh was

used as the current collector, and the electrode diameter was 14 mm. A circular Li foil, having a diameter of 16 mm and a thickness of 0.2 mm, was used as the counter electrode. A microporous polypropylene sheet was used as the separator. A 1 M $LiPF_6$ solution in a 1:2 (v/v) mixture of ethylene carbonate and diethyl carbonate was used as the electrolyte. Cells were constructed in a dry room with a dew point below $-50\ ^\circ C$, and electrochemical measurements were conducted with a current density of 15 mA g^{-1} (19 mA cm^{-2}) at 25 $^\circ C$ after standing overnight under open-circuit conditions.

Section VI-III   Results and Discussion

VI-III-I   Structural characterization

Table 6-3-1-1 lists the results of a chemical analysis of the ion-exchanged samples. Negligible amounts of residual Na were present in these samples (i.e., 0.03–0.04). To simplify the chemical formula, the sample composition was denoted as $x = 0$. Considering the negligible Na content, $Na_{0.034}Li_{0.64}Ni_{0.33}Mn_{0.67}O_2$ was also represented in $Li_{0.7}Ni_{0.33}Mn_{0.67}O_2$.

Table 6-3-1-1 Chemical analysis results for each sample. Each value is normalized to contain one TM per formula .

Sample	Na	Li	Ni	Mn
$Li_{0.7}Ni_{0.5}Mn_{0.5}O_2$	0.038	0.73	0.50	0.50
$Li_{0.7}Ni_{0.33}Mn_{0.67}O_2$	0.034	0.64	0.33	0.67
$Li_{0.7}Ni_{0.2}Mn_{0.8}O_2$	0.033	0.69	0.20	0.80

Figure 6-3-1-1 shows the XRD patterns of the as-prepared $O3\text{-}NaNi_{0.5}Mn_{0.5}O_2$, chemically oxidized $P3\text{-}Na_{0.7}Ni_{0.5}Mn_{0.5}O_2$, ion-exchanged $O3\text{-}Li_{0.7}Ni_{0.5}Mn_{0.5}O_2$ and $HT\text{-}Li_{0.7}Ni_{0.5}Mn_{0.5}O_2$ ($O3\text{-}Li_{0.7}Ni_{0.5}Mn_{0.5}O_2$ with thermal treatment). All the obtained samples were identified to be pure phases [9,14]. The c-axis length of $P3\text{-}Na_{0.7}Ni_{0.5}Mn_{0.5}O_2$ after chemical oxidation was significantly greater than that of the as-prepared $O3\text{-}NaNi_{0.5}Mn_{0.5}O_2$ because NaO_6 prisms were larger than NaO_6 octahedra, and the distance between the $Ni_{0.5}Mn_{0.5}O_2$ layers was enlarged; that is, the c-axis length was elongated [9]. The c-axis length of $Li_{0.7}Ni_{0.5}Mn_{0.5}O_2$ was significantly shorter than that of $Na_{0.7}Ni_{0.5}Mn_{0.5}O_2$ because the ionic radius of Li^+ (0.76 Å) is smaller than that of Na^+ (1.02 Å) [15], which in turn decreases the distance between the $Ni_{0.5}Mn_{0.5}O_2$ layers.

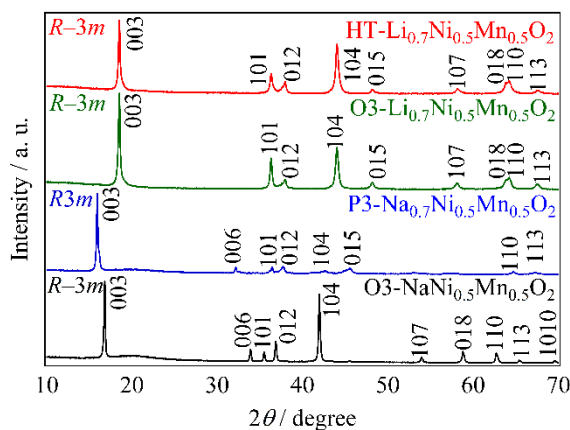Figure 6-3-1-1. XRD patterns of the as-prepared $O3\text{-}NaNi_{0.5}Mn_{0.5}O_2$, chemically oxidized $P3\text{-}Na_{0.7}Ni_{0.5}Mn_{0.5}O_2$, ion-exchanged $O3\text{-}Li_{0.7}Ni_{0.5}Mn_{0.5}O_2$, and thermally treated $HT\text{-}Li_{0.7}Ni_{0.5}Mn_{0.5}O_2$.

Figure 6-3-1-2. shows the XRD patterns of the as-prepared $P3\text{-}Na_{0.7}Ni_{0.2}Mn_{0.8}O_2$, ion-exchanged $O3\text{-}Li_{0.7}Ni_{0.2}Mn_{0.8}O_2$ and $HT\text{-}Li_{0.7}Ni_{0.2}Mn_{0.8}O_2$. All the obtained samples were identified to be pure phases.
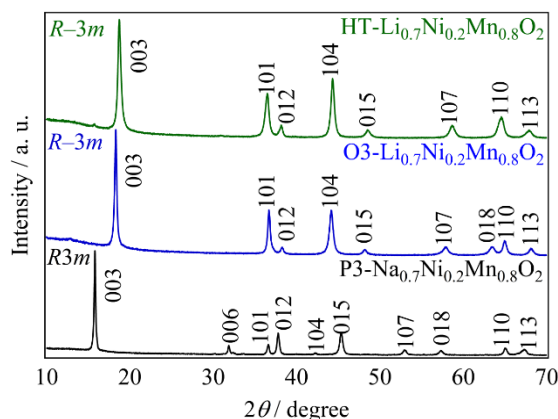
Figure 6-3-1-2. XRD patterns of the as-prepared P3-$Na_{0.7}Ni_{0.2}Mn_{0.8}O_2$, ion-exchanged O3-$Li_{0.7}Ni_{0.2}Mn_{0.8}O_2$, and thermally treated HT-$Li_{0.7}Ni_{0.2}Mn_{0.8}O_2$.

Table 6-3-1-2 lists the lattice parameters for HT-$Li_{0.7}Ni_{1-y}Mn_yO_2$. Both a- and c-axis length gradually decreased with increase in the substituted Mn content y from 0.5 to 0.8 because $Ni_{1-y}Mn_yO_6$ octahedra should contract owing to the different ionic radius between Ni^{2+} (0.69 Å) and Mn^{4+} (0.53 Å) [15]. In addition, the c/a ratio approached 4.90 with increasing y, which is the ideal value for a spinel-type structure [16–17].

Table 6-3-1-2 The lattice parameters for HT-$Li_{0.7}Ni_{1-y}Mn_yO_2$.

Sample	a / Å	c / Å	c/a
HT-$Li_{0.7}Ni_{0.5}Mn_{0.5}O_2$	2.8943(1)	14.353(1)	4.959
HT-$Li_{0.7}Ni_{0.33}Mn_{0.67}O_2$	2.8831(1)	14.221(1)	4.933
HT-$Li_{0.7}Ni_{0.2}Mn_{0.8}O_2$	2.8812(1)	14.165(1)	4.916

Figure 6-3-1-3 shows the ^6Li MAS-NMR spectra of HT-$Li_{0.7}Ni_{1-y}Mn_yO_2$. Three resonances were observed at 1500, 925, and 750 ppm, indicative of Li ions occupying three crystallographically different sites in the structure. The small, broad resonance at 1500 ppm was assigned to Li in a honeycomb-like arrangement of manganese ions (i.e., 6 Mn nearest neighbors) within the TM layer, as observed in $Li[Li_{1/3}Mn_{2/3}]O_2$ (Li_2MnO_3) [18–19]. Moreover, the peak at 750 ppm was attributed to the layer-type structure, which is assigned to Li in an alkali environment [19]. The peak at 925 ppm was attributed to the spinel-type structure [20]. Table 6-3-1-3 lists the ratio of the peak areas of 1500, 925, and 750 ppm peaks for HT-$Li_{0.7}Ni_{1-y}Mn_yO_2$. No distinct difference was confirmed in the variation of the 1500 ppm peaks in all samples. On the other hand, the spinel phase content for the peak at 925 ppm increased from 33% ($y = 0.5$) to 69% ($y = 0.8$). This is consistent with the c/a ratio approaching 4.90 with increasing y as mentioned above (Table 6-3-1-2).
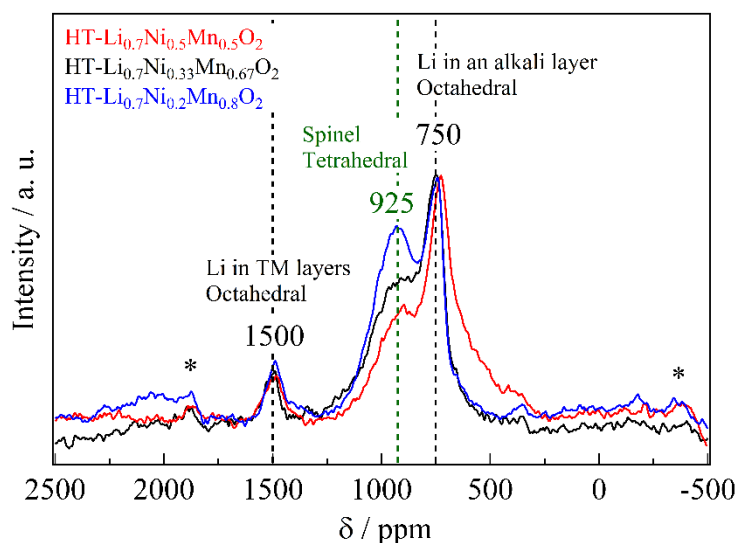
Figure 6-3-1-3. ^{6}Li MAS-NMR spectra of HT-Li$_{0.7}$Ni$_{1-y}$Mn$_y$O$_2$ (y = 0.5, 0.67, and 0.8) measured at room temperature. Spinning sidebands are indicated in asterisks.

Table 6-3-1-3 Calculation of probabilities for a Li environment with HT-Li$_{0.7}$Ni$_{1-y}$Mn$_y$O$_2$.

Sample	1500 ppm	925 ppm	750 ppm
HT-Li$_{0.7}$Ni$_{0.5}$Mn$_{0.5}$O$_2$	5 %	33 %	62 %
HT-Li$_{0.7}$Ni$_{0.33}$Mn$_{0.67}$O$_2$	6 %	59 %	35 %
HT-Li$_{0.7}$Ni$_{0.2}$Mn$_{0.8}$O$_2$	6 %	69 %	25 %

Figure 6-3-1-4 shows the TGA results for Li$_{0.7}$Ni$_{1-y}$Mn$_y$O$_2$ in the temperature ranging from 50 to 900 °C. During initial heating, Li$_{0.7}$Ni$_{0.5}$Mn$_{0.5}$O$_2$ exhibited a clear weight loss between 50 and 450 °C and above 650 °C. Moreover, above 700 °C, the weight change appeared to be reversible, and finally, the weight was ca. −3% at room temperature. On the other hand, on heating, Li$_{0.7}$Ni$_{1-y}$Mn$_y$O$_2$ (y = 0.67 and 0.8) exhibited an initial weight gain between 300 and 500 °C, followed by a slight change in weight up to 650 °C, beyond which a sharp weight loss was observed. The weight loss above 700 °C was reversible, and the weight at 700 °C was retained at 50 °C to give a final weight of approximately −0.5%. Such weight loss and regain behavior have been reported to be caused by the loss or gain of oxygen [21]. A high correlation was observed between the weight loss at a heat treatment temperature of 500 °C and spinel phase amount of ^{6}Li MAS-NMR.

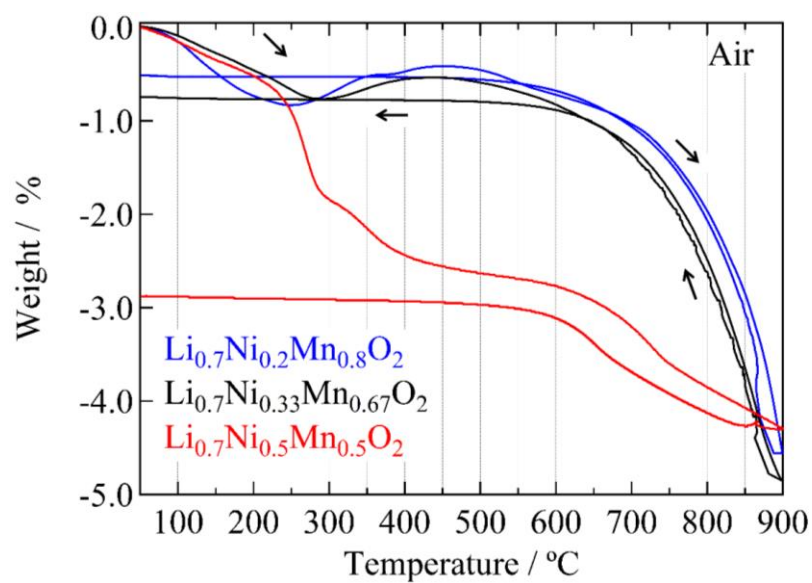Figure 6-3-1-4. TGA curves of $Li_{0.7}Ni_{1-y}Mn_yO_2$ (y = 0.5, 0.67, and 0.8), showing the weight variation upon oxygen loss and regain.

VI-III-II   Electrochemical performance

Figure 6-3-3-1 shows the initial charge and discharge voltage-capacity curves of HT-$Li_{0.7}Ni_{1-y}Mn_yO_2$ starting from charging in the voltage range between 2.0 and 4.8 V, at a current density of 15 mA g^{-1} and a temperature of 25 °C. The initial charge capacity decreased from 194 to 175 mA h g^{-1} with increasing Mn content x, while the initial discharge capacity increased. HT-$Li_{0.7}Ni_{0.2}Mn_{0.8}O_2$ exhibited a maximum discharge capacity of 280 mA h g^{-1}. Moreover, the voltage discharge curve also changed from a profile with two distinct plateau to a sloping voltage profile with decreasing Mn content. The average discharge voltage of the HT-$Li_{0.7}Ni_{1-y}Mn_yO_2$ decreased from 3.57 V ($y = 0.5$) to 2.89 V ($y = 0.8$). The discharge capacity at the 3 V plateau region increased from approximately 20 mA h g^{-1} ($y = 0.5$) to approximately 120 mA h g^{-1} ($y = 0.8$) for HT-$Li_{0.7}Ni_{1-y}Mn_yO_2$ compounds because the spinel phase increased with the Mn content (Fig. 6-3-1-3); that is, c/a ratio approached to 4.90 (Table 6-3-1-3).
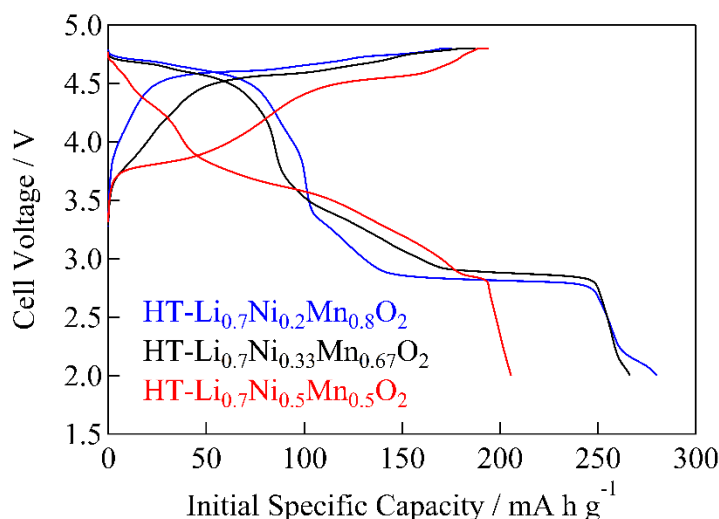
Figure 6-3-3-1. Initial charge and discharge voltage-capacity curves for Li/HT-$Li_{0.7}Ni_{1-y}Mn_yO_2$ ($y = 0.5$, 0.67, and 0.8) cells at a rate of 15 mA g^{-1} in the voltages ranging from 2.0 V to 4.8 V at 25 °C. Note that the as-prepared sample is Li-deficient sample; therefore, the initial charge capacity is lower than the discharge capacity.

Figure 6-3-3-2 shows the cycle performance of HT-$Li_{0.7}Ni_{1-y}Mn_yO_2$. The discharge capacity retention of HT-$Li_{0.7}Ni_{1-y}Mn_yO_2$ increased from 80 to 87 % at 50 th cycles with increasing Mn content y. Figure 6-3-3-3 and 6-3-3-2 show the initial charge and discharge voltage-capacity curves and the cycle performance of $Li_{0.7}Ni_{1-y}Mn_yO_2$ with their HT counterparts. The HT-$Li_{0.7}Ni_{1-y}Mn_yO_2$ attain not only high capacity and high voltage but also good cycle.
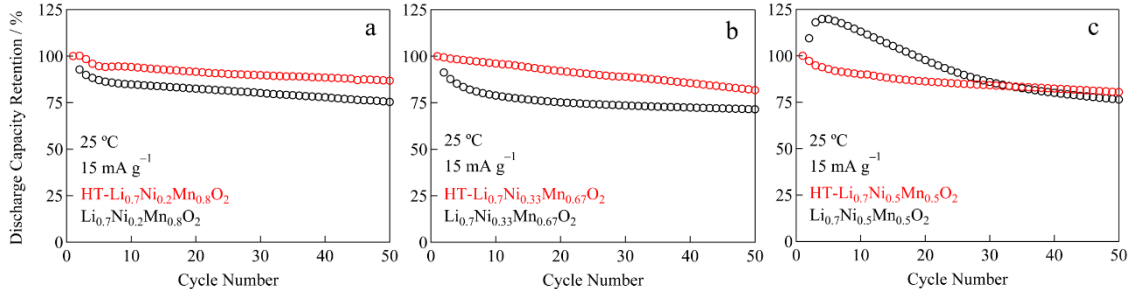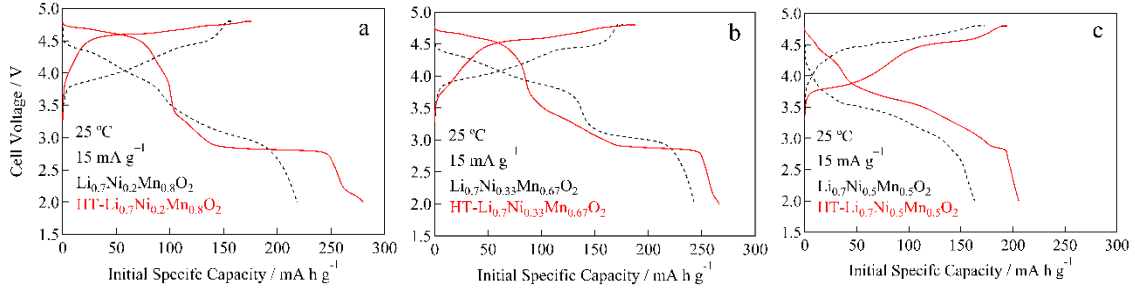
Figure 6-3-3-2. Cycle performance for Li/Li$_{0.7}$Ni$_{1-y}$Mn$_y$O$_2$ and Li/HT-Li$_{0.7}$Ni$_{1-y}$Mn$_y$O$_2$ (y = 0.5, 0.67, and 0.8) cells at a rate of 15 mA g^{-1} in voltages ranging from 2.0 V to 4.8 V at 25 ^{o}C.

Figure 6-3-3-3. Initial charge and discharge voltage-capacity curves for Li/Li$_{0.7}$Ni$_{1-y}$Mn$_y$O$_2$ and Li/HT-Li$_{0.7}$Ni$_{1-y}$Mn$_y$O$_2$ (y = 0.5, 0.67, and 0.8) cells at a rate of 15 mA g^{-1} in voltages ranging from 2.0 V to 4.8 V at 25 ^{o}C. Note that the as-prepared sample is Li-deficient sample; therefore, the initial charge capacity is lower than the discharge capacity.

As mentioned above, the initial charge and discharge voltage-capacity curves of HT-Li$_{0.7}$Ni$_{1-y}$Mn$_y$O$_2$ (0.5 $\leq$ y $\leq$ 0.8) varied with the Mn content y. All phenomena can be associated with the generation of the spinel phase. The decrease in the Mn content y resulted in a deviation from the spinel phase owing to the difference in the ionic radius between Ni^{2+} (0.69 Å) and Mn^{4+} (0.53 Å) in octahedral coordination (Table 6-3-1-2). In other words, from a crystallographic viewpoint, the decrease in the Mn content y curtail the formation of the spinel phase, which is reflected by the different initial charge and discharge voltage-capacity curves. In HT-Li$_{0.7}$Ni$_{1-y}$Mn$_y$O$_2$ (0.5 $\leq$ y $\leq$ 0.8), the Mn content y can be adjusted to modify the voltage-capacity curves for various power applications.

Section V-IV   Conclusions

In this study, HT-$Li_{0.7}Ni_{1-y}Mn_yO_2$ ($0.5 \leq y \leq 0.8$) was prepared as a class of high-voltage and high-capacity positive electrode materials for rechargeable lithium batteries. The attained performance is attributed to the predominant retention of the layered rock-salt structure over the spinel phase. Thus, the spinel-phase transformation can be curtailed by the variation of the Mn content in the compositions of HT-$Li_{0.7}Ni_{1-y}Mn_yO_2$ ($0.5 \leq y \leq 0.8$), demonstrating the feasibility of modifying the capacity–voltage characteristics through a judicious control of the constituent Mn content in related compositions.

Reference

[37] J. M. Paulsen, C. L. Thomas, J. R. Dahn, *J. Electrochem. Soc.*, **147** (2000) 861.

[38] J. M. Paulsen, J. R. Dahn, *J. Electrochem. Soc.*, **147** (2000) 2478.

[39] J. M. Paulsen, D. Larcher, J. R. Dahn, *J. Electrochem. Soc.*, **147** (2000) 2862.

[40] Z. Lu, R. A. Donaberger, J. R. Dahn, *Chem. Mater.*, **12** (2000) 3583.

[41] S. Komaba, K. Yoshii, A. Ogata, I. Nakai, *Electrochim. Acta*, **54** (2009) 2353.

[42] W. Zhao, S. Harada, Y. Furuya, S. Yamamoto, H. Noguchi, *J. Power Sources*, **261** (2014) 324.

[43] K. Chiba, M. Shikano, H. Sakaebe, *J. Power Sources* **304** (2016) 60.

[44] J. Bhattacharya, C. Wolverton, *J. Electrochem. Soc.*, **161** (2014) A1440.

[45] S. Komaba, N. Yabuuchi, T. Nakayama, A. Ogata, T. Ishikawa, I. Nakai, *Inorg. Chem.*, **51** (2012) 6211.

[46] R. Gupta, A. Manthiram, *J. Solid State Chem.*, **121** (1996) 483.

[47] N. Ishida, H. Hayakawa, H. Shibuya, J. Imaizumi, J. Akimoto, *J. Power Sources* **244** (2013) 505.

[48] Topas V4: General Profile and Structure Analysis Software for Powder Diffraction Data, Bruker AXS, Karlsruhe, Germany, 2008.

[49] D. Massiot, F. Fayon, M. Capron, I. King, S. L. Calvé, B. Alonso, J. O. Durand, B. Bujoli, Z. Gan, G. Hoatson, *Magn. Reson. Chem.*, **40** (2002) 70.

[50] H. Gwon, S. W. Kim, Y. U. Park, J. Hong, G. Ceder, S. Jeon, K. Kang, *Inorg. Chem.*, **53** (2014) 8083.

[51] R. D. Shannon, *Acta Crystallogr*. A, **32** (1976) 751.

[52] R. J. Gummow, D. C. Liles, M. M. Thackeray, *Mat. Res. Bull.*, **28** (1993) 235.

[53] E. Rossen, J. N. Reimers, J. R. Dahn, *Solid State Ionics*, **62** (1993) 53.

[54] P. Mustarelli, V. Massarotti, M. Bini, D. Capsoni, *Phys. Rev. B*, **55** (1997) 12018.

[55] J. Bréger, M. Jiang, N. Dupré, Y. S. Meng, Y. Shao-Horn, G. Ceder, C. P. Grey, *J. Solid State Chem.*, **178** (2005) 2575.

[56] Y. J. Lee, C. Eng, C. P. Grey, *J. Electrochem. Soc.*, **148** (2001) A249.

[57] J. Song, D. W. Shin, Y. Lu, C. D. Amos, A. Manthiram, J. B. Goodenough, *Chem. Mater.*, **24** (2012) 3101.

Chapter VII

Sodium lithium nickel manganese oxide

$$Na_xLi_{0.67+y}Ni_{0.33}Mn_{0.67}O_2$$

－Control of the ratio of

layered rock-salt and spinel structure by residual Na content－

Section VII-I Introduction

Lithium nickel manganese oxides have attracted a great deal of interest as a positive electrode material for lithium-ion batteries owing to their high capacity and high voltage. In particular, lithium-deficient $Li_{0.67}Ni_{0.33}Mn_{0.67}O_2$ with an O3-type layered structure has been extensively investigated as a promising material for a positive electrode [1-4]. The O3-$Li_{0.67}Ni_{0.33}Mn_{0.67}O_2$ is known to be a metastable phase and can readily be synthesized by the Na/Li ion-exchange reaction of a Na-based layered compound, P3-$Na_{0.67}Ni_{0.33}Mn_{0.67}O_2$. It may be noted that the layered structures are named according to the packing designation commonly used for layered oxides [5]. For example, the letters P and O describe the alkali ion environment (prismatic and octahedral, respectively), whereas the numbers 1, 2, and 3 indicate the number of slabs required to describe the unit cell [5]. The discharge capacity of the O3-$Li_{0.67}Ni_{0.33}Mn_{0.67}O_2$ vs Li/Li$^+$ has been reported to be about 200 mA h g^{-1} between 4.8 and 2.0 V [4]. In addition, it exhibits poor cycle performance as it undergoes a phase transformation to the spinel structure upon electrochemical cycling as is commonly known in the O3-type structure. Since the oxygen array in the O3-type structure is very similar to that of the spinel structure, a direct phase transformation is often observed [1].

Recently, we reported that thermal treatment after the ion-exchange reaction by a molten salt method improved the cycle performance of O3-$Li_{0.67}Ni_{0.33}Mn_{0.67}O_2$ [4]. The charge and discharge voltage-capacity curves of the thermally treated O3-$Li_{0.67}Ni_{0.33}Mn_{0.67}O_2$ exhibited a plateau around about 4.8 V and a high discharge capacity of 257 mA h g^{-1} between 4.8 and 2.0 V vs Li/Li$^+$. The thermal treatment for O3-$Li_{0.67}Ni_{0.33}Mn_{0.67}O_2$ is extremely interesting as it affords better cycle performance, a higher discharge voltage, and higher specific capacity compared to the values for as-prepared O3-$Li_{0.67}Ni_{0.33}Mn_{0.67}O_2$ [4]. However, the discharge voltage-capacity curve showed a steep slope between 4.7 and 3.0 V vs Li/Li$^+$, owing to the increased spinel phase content as a result of the thermal treatment.

We previously investigated sample preparation by a reflux method followed by thermal treatment and have successfully improved the discharge capacity. The initial discharge capacity increased from 257 mA h g^{-1} for the molten salt method to 265 mA h g^{-1} for the reflux method [6]. In addition, the discharge voltage-capacity curve showed a gradual slope between 4.7 and 3.0 V vs Li/Li$^+$ and a plateau around about 4.8 V, owing to the decreased spinel phase as a result of higher residual Na content. However, the high discharge performance could not be utilized in the present battery system by using graphite as the negative electrode material, because the initial charge capacity was only about 180 mA h g^{-1} in the thermally treated $Na_{0.093}Li_{0.57}Ni_{0.33}Mn_{0.67}O_2$ by using Li metal. From this viewpoint, further lithiation should be performed during the synthesis of thermally treated samples.

In this paper, we have studied $Na_xLi_{0.67+y}Ni_{0.33}Mn_{0.67}O_2$ ($0.010 \leq x \leq 0.013$, $0.16 \leq y \leq 0.20$) synthesized by chemical lithiation using LiI [7,8]. To the best of our knowledge, this is the first attempt to clarify the relationship between the charge-discharge properties and crystal structure of $Na_xLi_{0.67+y}Ni_{0.33}Mn_{0.67}O_2$.

Section VII-II   Experiment

VII-II-I   Synthesis

The precursor P3-$Na_{0.67}Ni_{0.33}Mn_{0.67}O_2$ was synthesized by the conventional solid state reaction of a stoichiometric mixture of CH_3COONa (98.5% pure), $Ni(OH)_2$ (99.9% pure), and Mn_2O_3 (99.9% pure) with 3% excess sodium [1-4]. Firstly, the weighed powder was mixed using the ball milling method and then pressed into pellets. Secondly, the pellets were heated at 650 °C for 10 h under O2 flow to obtain a pure P3 phase, following which the pellets were pulverized. For conducting the Na/Li ion-exchange reaction, the host material P3-$Na_{0.67}Ni_{0.33}Mn_{0.67}O_2$ was refluxed with 0.4, 0.8, and 1.6-fold excesses of lithium supplied in the form of a solution of LiBr (99.9% pure) in methanol (MeOH) at 110 °C for 5 h [6]. The sample was filtered, washed with MeOH, and then dried at 90 °C overnight. To induce a change in the crystal structure, the sample was heated at 500 °C for 5 h in air [4,6]. Hereafter, the thermally treated $Na_zLi_{0.67-z}Ni_{0.33}Mn_{0.67}O_2$ will be referred to as O3$_{HT}$-$Na_zLi_{0.67-z}Ni_{0.33}Mn_{0.67}O_2$. The thermally treated sample was refluxed with a 2.0-fold excess of lithium supplied in the form of a LiI solution (99.9% pure) in acetonitrile (CH_3CN) at 140 °C for 5 h.[7,8] After LiI chemical lithiation, the sample was filtered, washed with CH_3CN and MeOH, and then dried at 90 °C overnight.

VI-II-II   Characterization

The samples were characterized by powder X–ray diffraction (XRD) using a D8 ADVANCE diffractometer (Bruker) with a Cu Kα radiation source (operating conditions: 40 kV and 55 mA). XRD intensity data were collected for 0.25 s at 2θ intervals of 0.02° over a range of 10 to 70°. TOPAS Ver. 4.2 software package was used for Pawley analysis.[9] Cationic chemical composition of Li, Na, Ni and Mn was determined from inductively coupled plasma-atomic emission spectroscopy (ICP-AES; Shimadzu ICPS–8000). The solid-state 6Li magic-angle spinning nuclear magnetic resonance (^6Li MAS-NMR) spectra were recorded at room temperature using an AVANCE300 spectrometer (Bruker) at 44 MHz with a spinning rate of 50 kHz for 6Li nuclei by a rotor-synchronized spin-echo pulse sequence. The pulse width was 3.6 μs ($\pi/2$ pulse) and the chemical shift was recorded relative to a 1.0 mol dm^{-3} ^6LiCl aqueous solution. ^6Li spectral decomposition was performed using the Dmfit software, which allows for the variation of peak position, peak height, line width, and the ratio of Gaussian to Lorentzian functions [10]. Further, scanning electron microscopy (SEM, Keyence VE-8800) was used to characterize the morphology and crystal sizes of the samples obtained before and after chemical lithiation.

VI-II-III   Electrochemical properties

Electrochemical cycling test was performed using a lithium coin-type cell (CR2032). The working electrode was prepared using a mixture of 10 mg of active material, 10 mg of acetylene black as the conductive agent and 2 mg of polytetrafluoroethylene as the binder. The mixture was cast on the Al mesh, the current collector, and pressed, and then the circular working electrode with a diameter of 14 mm was obtained. A Li foil, cut in a circle with a diameter of 16 mm and thickness of 0.2 mm was used as the counter electrode, while a microporous polypropylene sheet was used as the separator. A 1 mol dm^{-3} $LiPF_6$ solution in a 1:2 (v/v)

mixture of ethylene carbonate and diethyl carbonate was used as the electrolyte. Cells were fabricated in a dry room with a dew point below −50 °C and tested at 25 °C. Charge capacity was measured in the constant current and constant voltage (CCCV) mode up to 4.8 V vs Li/Li$^+$ with a current density of 15 mA g^{-1} (19 mA cm^{-2}) and then using a potentiostatic step for 15 min, while the discharge capacity was measured in the constant current (CC) mode with a current density of 15 mA g^{-1} to 2.0 V vs Li/Li$^+$.

Section VII-III   Results and discussion

VII-III-I   Synthesis

P3-$Na_{0.67}Ni_{0.33}Mn_{0.67}O_2$ was used as the precursor for the ion-exchange reaction. Table 7-3-1-1 shows the chemical compositions of all the samples. The residual Na content was successfully adjusted by the LiBr concentration. The Li content in all the samples was increased by chemical lithiation, while the residual Na content was close to 0.

Table 7-3-1-1 Chemical composition of all the samples.

Concentration	Na	Li	Ni	Mn
LiBr 0.4-fold molar	0.27	0.39	0.33	0.67
chemical lithium insertion	0.013	0.86	0.33	0.67
LiBr 0.8-fold molar	0.19	0.47	0.33	0.67
chemical lithium insertion	0.012	0.87	0.33	0.67
LiBr 1.6-fold molar	0.15	0.51	0.33	0.67
chemical lithium insertion	0.010	0.83	0.33	0.67

Figure 7-3-1-1a shows the XRD patterns of P3-$Na_{0.67}Ni_{0.33}Mn_{0.67}O_2$ and thermally treated samples. All the patterns exhibited some very weak peaks corresponding to rock-salt-type NiO, which is a trace impurity. P3-$Na_{0.67}Ni_{0.33}Mn_{0.67}O_2$ can be obtained as a nearly single phase with the space group $R3m$ [2]. All the patterns showed phase separation of the layered and spinel-type structures. With decreasing residual Na content x, the four-phase coexistence of the P3, OP2, O3, and spinel phases in $O3_{HT}$-$Na_{0.27}Li_{0.39}Ni_{0.33}Mn_{0.67}O_2$ was transformed to the three-phase state consisting of OP2, O3 and spinel phases in $O3_{HT}$-$Na_{0.19}Li_{0.47}Ni_{0.33}Mn_{0.67}O_2$ and $Na_{0.15}Li_{0.51}Ni_{0.33}Mn_{0.67}O_2$ [4,6,11]. Hereafter, we denote $Na_xLi_{0.67+y}Ni_{0.33}Mn_{0.67}O_2$ by a residual Na content before chemical lithiation, 0.15, 0.19, and 0.27, as Sample015, Sample019 and Sample027, respectively.
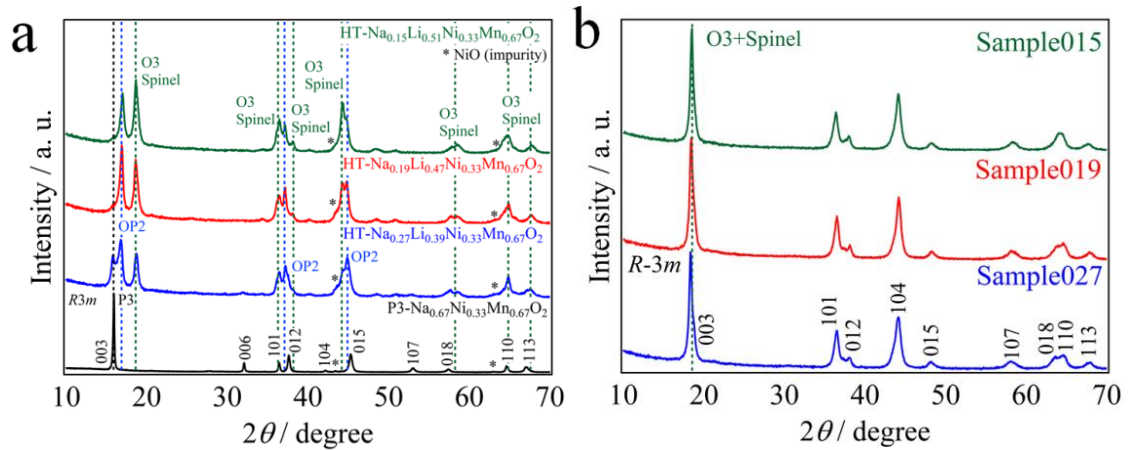

Figure 7-3-1-1. XRD patterns of (a) the as-prepared P3-$Na_{0.67}Ni_{0.33}Mn_{0.67}O_2$ and before chemical lithiation, and (b) after chemical lithiation.

The powder XRD patterns of them (Fig. 7-3-1-1b) were fully indexed with the space group R-$3m$. Before chemical lithiation, a clear separation of the diffraction peaks between 15 and 20° was observed (Fig. 7-3-1-1a), while a single broad diffraction peak was observed after chemical lithiation (Fig. 7-3-1-1b). P3 and OP2 phases disappeared upon chemical lithium insertion. The

broad XRD patterns observed for Sample015, Sample019 and Sample027 may be considered to originate from a mixture of the layered and spinel-type structures. By using the layered structure model (space group: $R-3m$), the lattice parameters of Sample015, Sample019 and Sample027 were calculated with TOPAS Ver. 4.2 and the results are presented in Table 7-3-1-2.

Table 7-3-1-2 Chemical composition of all the samples.

Sample	a / Å	c / Å	c / a
Sample027 $(\mathbf{Na_{0.013}Li_{0.86}Ni_{0.33}Mn_{0.67}O_2})$	2.8819(1)	14.403(1)	5.00
Sample019 $(\mathbf{Na_{0.012}Li_{0.87}Ni_{0.33}Mn_{0.67}O_2})$	2.8821(1)	14.362(1)	4.98
Sample015 $(\mathbf{Na_{0.010}Li_{0.83}Ni_{0.33}Mn_{0.67}O_2})$	2.8898(1)	14.313(1)	4.95

The lattice parameter a, which reflects the nearest-neighbor O-O distance, decreased slightly with increasing the residual Na content [12]. On the other hand, the lattice parameter c increased significantly from 14.313 to 14.403 Å. This can be explained by the expansion of the interlayer space, which was occupied by the alkali ions,1-4 because the ionic radius of Na^+ (1.02 Å) is larger than that of Li^+ (0.76 Å) [13]. In addition, the c/a ratio approached 4.90 with decreasing the residual Na content, which is the theoretical value for a spinel structure [14,15]. In other words, the cubic-close-packed oxygen array of the rhombohedral structure approached cubic symmetry [16]. The stacking of oxide ions in both the layered rock-salt and spinel-type structures is identical, and the only difference between the structures is the site occupied by the transition metal (TM) [17]. However, considering that the residual Na content in the chemical lithiation samples is subtle, significant changes in the coordination environment around Na atom could not be expected. The coordination environment around Li atoms is more important, because it induces significant differences among the chemical lithiation samples.
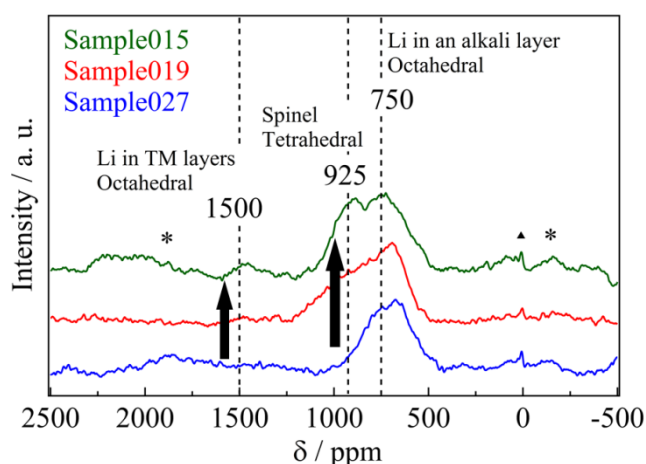

Figure 7-3-1-2. ^{6}Li-MAS-NMR spectra of Sample015, Sample019 and Sample027 measured at room temperature. "*" and "▲" indicate spinning sidebands and additional signals arising from traces of Li salt, respectively.

Figure 7-3-1-2 shows the ^{6}Li MAS-NMR spectra of Sample015, Sample019 and Sample027. Three resonances were observed at 1500, 925, and 750 ppm, indicating that Li occupied three crystallographically different sites in the structure (an additional resonance at 0 ppm is attributed to traces of Li salt) [18]. The small, broad resonance at 1500 ppm was assigned to Li$^+$ in a honeycomb-like arrangement surrounded by the 6 manganese ions within the TM layer, as observed in Li[Li$_{1/3}$Mn$_{2/3}$]O$_2$ (Li$_2$MnO$_3$) [19,20]. The resonance at 750 ppm was attributed to the layered structure O3-Li$_{0.67}$Ni$_{0.33}$Mn$_{0.67}$O$_2$, which is assigned to LiO$_6$ in octahedral coordination [21]. The resonance at 925 ppm was attributed to the spinel structure LiNi$_{0.5}$Mn$_{1.5}$O$_4$, which is assigned to LiO$_4$ in tetrahedral coordination [22]. A distinct difference in the variation of 1500 and 925 ppm resonances at various c/a ratios was observed (Table 7-3-1-2).

Table 7-3-1-3 shows the spinel phase content for Sample015, Sample019 and Sample027. The spinel phase content for the peak at 925 ppm increased from 7.1 % (Sample027) to 31 % (Sample015) with decreasing the residual Na content. The chemical lithiation samples have almost the same chemical composition although the ^{6}Li MAS-NMR spectra and the c/a ratio of the lattice parameter vary (Table 7-3-1-2). To illustrate this clearly, the difference of the ^{6}Li MAS-NMR spectra of the samples before chemical lithiation is compared.

Table 7-3-1-2 Spinel and layer structure content of Sample015, Sample019 and Sample027.

Sample	Spinel	Layer
Sample027 (Na$_{0.013}$Li$_{0.86}$Ni$_{0.33}$Mn$_{0.67}$O$_2$)	7 %	93 %
Sample019 (Na$_{0.012}$Li$_{0.87}$Ni$_{0.33}$Mn$_{0.67}$O$_2$)	21 %	79 %
Sample015 (Na$_{0.010}$Li$_{0.83}$Ni$_{0.33}$Mn$_{0.67}$O$_2$)	31 %	69 %
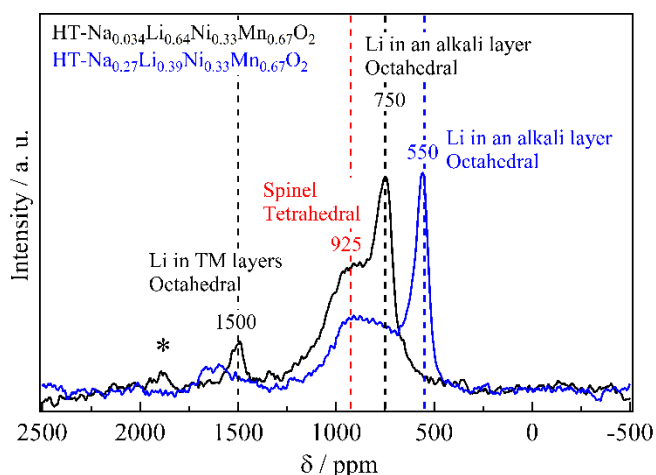
Figure 7-3-1-3 ^{6}Li-MAS-NMR spectra of HT-Na$_z$Li$_{0.67-z}$Ni$_{0.33}$Mn$_{0.67}$O$_2$ (before chemical lithiation) measured at room temperature. "*" indicates a spinning sideband.

Figure 7-3-1-3 shows the ^{6}Li MAS-NMR spectra of HT-Na$_z$Li$_{0.67-z}$Ni$_{0.33}$Mn$_{0.67}$O$_2$. HT-Na$_{0.27}$Li$_{0.39}$Ni$_{0.33}$Mn$_{0.67}$O$_2$ spectrum is plotted together with HT-Na$_{0.034}$Li$_{0.63}$Ni$_{0.33}$Mn$_{0.67}$O$_2$ spectrum reported previously for comparison [4]. Four observed resonances indicated that the Li occupied four crystallographically different sites in HT-Na$_{0.27}$Li$_{0.39}$Ni$_{0.33}$Mn$_{0.67}$O$_2$. The resonance at the 925 ppm which showed Li occupied the tetrahedral site in the spinel phase component increased with decreasing the value of the Na content. In other words, a fraction of the spinel phase component for the samples has been dominated by the residual Na content after the Na/Li ion-exchange reaction of the Na-based layered compound, P3-Na$_{0.67}$Ni$_{0.33}$Mn$_{0.67}$O$_2$. The resonance at 550 ppm is attributed to OP2-type layered structure, which is presumably assigned to LiO$_6$ in octahedral coordination. To illustrate 550 ppm peak, XRD patterns and ^{6}Li MAS-NMR spectrum of Na$_{0.27}$Li$_{0.39}$Ni$_{0.33}$Mn$_{0.67}$O$_2$ before heat treatment are compared.

Figure 7-3-1-4a and 7-3-1-4b show the XRD patterns and ^{6}Li MAS-NMR spectrum, respectively. As shown in Fig. 7-3-1-4b, Na$_{0.27}$Li$_{0.39}$Ni$_{0.33}$Mn$_{0.67}$O$_2$ was identified to be a nearly single phase of OP2 layered structure with space group $P3m1$ [11]. The strong peak at 550 ppm was observed. However, the resonance at 750 ppm was not observed, which is presumably attributed to O3-type layered structure with LiO$_6$ in octahedral coordination.
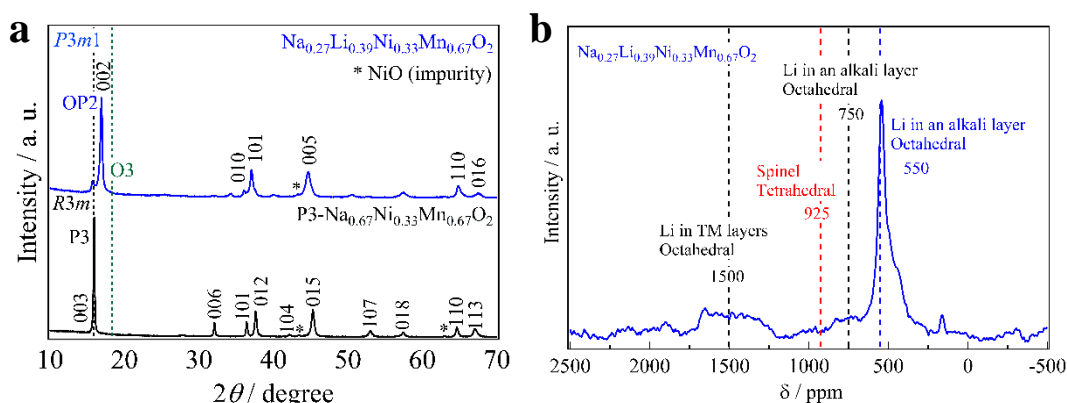

Figure 7-3-1-4 (a) XRD patterns of P3-Na$_{0.67}$Ni$_{0.33}$Mn$_{0.67}$O$_2$ and Na$_{0.27}$Li$_{0.39}$Ni$_{0.33}$Mn$_{0.67}$O$_2$ before heat treatment. (b) ^{6}Li-MAS-NMR spectrum of Na$_{0.27}$Li$_{0.39}$Ni$_{0.33}$Mn$_{0.67}$O$_2$ before heat treatment measured at room temperature.

VII-III-II   Electrochemical properties

Figure 7-3-2-1a shows the initial charge and discharge voltage-capacity curves of Sample015, Sample019 and Sample027 starting from charging in the voltage range between 2.0 and 4.8 V vs Li/Li$^+$ at a current density of 15 mA g^{-1} (0.06 C), at 25 °C. The initial discharge voltage-capacity curves exhibited two plateaus. The plateaus at around 4.7 and 2.8 V vs Li/Li$^+$ were attributed to the Ni$^{2+/4+}$ and Mn$^{3+/4+}$ redox reactions in the spinel phase, respectively [23]. In addition, the initial discharge voltage-capacity curve exhibited a gradual slope between 4.7 and 2.8 V vs Li/Li$^+$, which is attributed to the layered rock-salt structure [4,6]. Figure 7-3-2-1b shows the initial differential (dis)charge voltage curves for Sample015, Sample019 and Sample027. The peaks highlighted in red circles at around 4.7 and 2.8 V vs Li/Li$^+$ assigned to the redox reaction of the spinel phase component as mentioned above were observed and intensity of the peaks increased with increasing the value of the resonance at 925 ppm (Fig.

7-3-1-2) [23]. In Li-rich layered, the cation rearrangement in the initial charge delivered high discharge capacity [24]. In Li-deficient layered, the heat treatment at 500 °C caused the cation rearrangement including (i) the migration of transition metals from the crystal lattice: the layered structure transformed to the spinel structure [6].
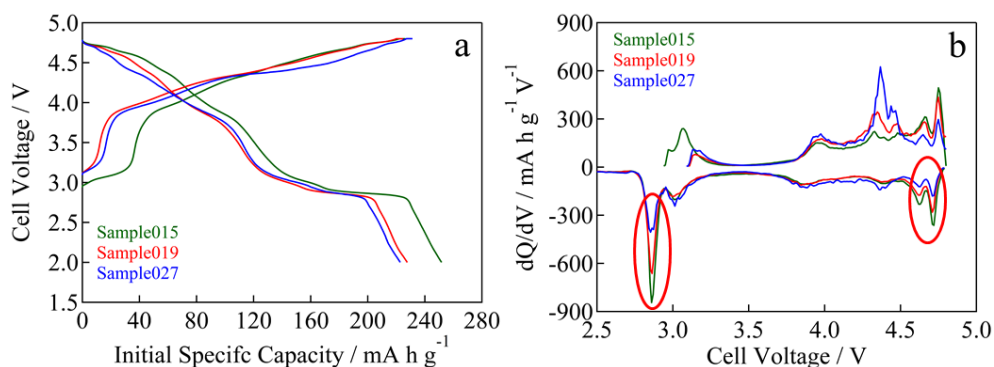

Figure 7-3-2-1 (a) Initial charge and discharge voltage curves for Sample015, Sample019 and Sample027. (b) Initial differential (dis)charge voltage plots for Sample015, Sample019 and Sample027.

In the case of Sample015, the initial charge capacity increased from 171 mA h g^{-1} for before chemical lithiation to 226 mA h g^{-1} for after chemical lithiation with increasing the Li content (Fig. 7-3-2-2a). The initial maximum discharge capacity and energy density were 252 mA h g^{-1} and 893 W h kg^{-1}, respectively.
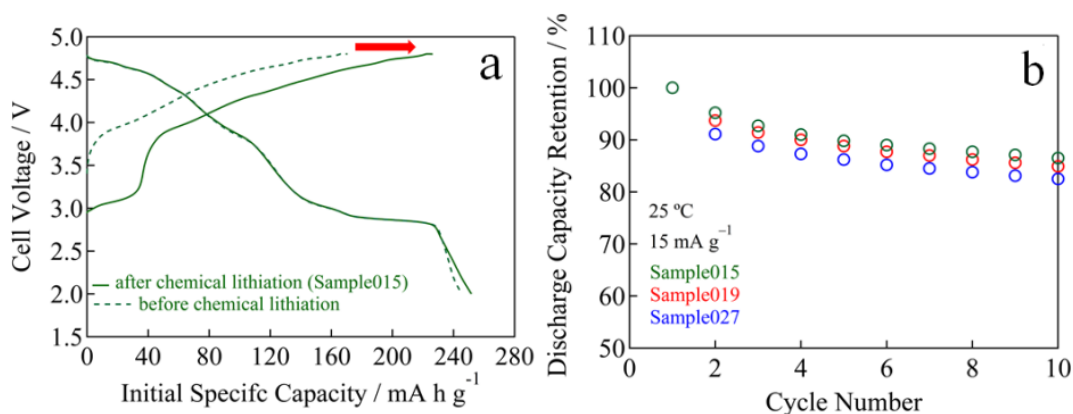

Figure 7-3-2-2 (a) Initial charge and discharge voltage curves for before and after chemical lithiation sample (Sample015). (b) Cycle performance of Sample015, Sample019 and Sample027.

Fig. 7-3-2-2b and 7-3-2-3 show the cycle performances of Sample015, Sample019 and Sample027. The discharge capacity retention of Sample015, Sample019 and Sample027 increased from 83 to 87 % at the 10th cycle with decreasing the residual Na content (Fig. 7-3-2-2b). Similarly, the average discharge voltage at the 10th cycle almost linearly increased with decreasing the residual Na content (Fig. 7-3-2-3).

One can say that the high carbon content in the composite electrode seems to affect the

capacity obtained. Therefore, the electrochemical performance was tested by a conventional composition with the lower carbon content. The composite electrode comprised the active material (95 wt %) with Super-P carbon (2.5 wt %) and PVdF (2.5 wt %). A 27.0 mg cm^{-2} of coating area density was used. As shown in Fig. 7-3-2-3a and 7-3-2-3b, Sample015 can sustain a high capacity and good capacity retention. In Na$_x$Li$_{0.67+y}$Ni$_{0.33}$Mn$_{0.67}$O$_2$ ($0.010 \leq x \leq 0.013$, $0.16 \leq y \leq 0.20$), the c/a ratio should reflect the spinel phase content, which would affect the charge and discharge voltage-capacity curves and cycle performance.
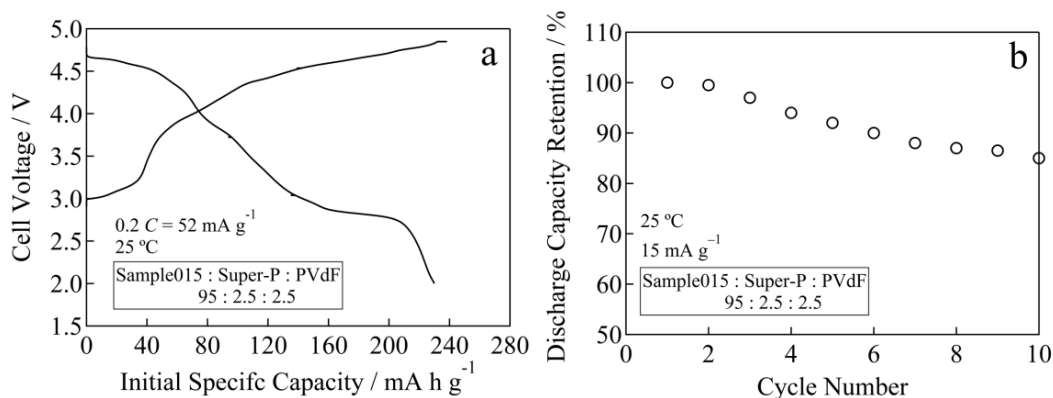

Figure 7-3-2-3 (a) (a) Initial specific capacity and (b) cycle performance for Sample015 at a rate of 52 mA g^{-1} (0.2 C) between 2.0 and 4.8 V vs Li/Li$^+$ at 25 °C.

Section VII-IV   Conclusions

In summary, we have synthesized $Na_xLi_{0.67+y}Ni_{0.33}Mn_{0.67}O_2$ ($0.010 \leq x \leq 0.013$, $0.16 \leq y \leq 0.20$) positive electrode materials by chemical lithiation using LiI. Cells containing these materials exhibited a gradually sloping curve. The initial maximum discharge capacity was 252 mA h g^{-1} in the case of Sample015 ($Na_{0.010}Li_{0.83}Ni_{0.33}Mn_{0.67}O_2$). This study clearly demonstrates the feasibility of obtaining suitable voltage-capacity characteristics by judiciously controlling the residual Na content x in $Na_xLi_{0.67+y}Ni_{0.33}Mn_{0.67}O_2$ ($0.010 \leq x \leq 0.013$, $0.16 \leq y \leq 0.20$) and related compositions. We show the relationship between the charge-discharge properties and crystal structure of $Na_xLi_{0.67+y}Ni_{0.33}Mn_{0.67}O_2$ by chemical lithiation using LiI. Although the chemical lithiation process in this study is a little cumbersome, the good electrochemical performance demonstrated by the obtained material is an advantage for the practical utilization.

Reference

[58] J. M. Paulsen, J. R. Dahn, *J. Electrochem. Soc.*, **147** (2000) 2478.

[59] Z. Lu, R. A. Donaberger, J. R. Dahn, *Chem. Mater.*, **12** (2000) 3583.

[60] W. Zhao, S. Harada, Y. Furuya, S. Yamamoto, H. Noguchi, *J. Power Sources*, **261** (2014) 324.

[61] K. Chiba, M. Shikano, H. Sakaebe, *J. Power Sources*, **304** (2016) 60.

[62] C. Delmas, C. Fouassier, P. Hagenmuller, *Physica*, **99B**, (1980) 81.

[63] K. Chiba, N. Taguchi, M. Shikano, H. Sakaebe, *J. Power Sources*, **311** (2016) 103.

[64] N. Ishida, H. Hayakawa, H. Shibuya, J. Imaizumi, J. Akimoto, *J. Electrochem. Soc.*, **160** (2013) A297.

[65] N. Ishida, H. Hayakawa, J. Akimoto, H. Shibuya, J. Imaizumi, *J. Power Sources*, **244** (2013) 505.

[66] TOPAS V4: General Profile and Structure Analysis Software for Powder Diffraction Data, Bruker AXS, Karlsruhe, Germany, 2008.

[67] D. Massiot, F. Fayon, M. Capron, I. King, S. L. Calvé, B. Alonso, J. O. Durand, B. Bujoli, Z. Gan, G. Hoatson, *Magn. Reson. Chem.*, **40** (2002) 70.

[68] N. Yabuuchi, M. Kajiyama, J. Iwatate, H. Nishikawa, S. Hitomi, R. Okuyama, R. Usui, Y. Yamada, S. Komaba, *Nat. Mater.*, **11** (2012) 512.

[69] J. Cabana, S. H. Kang, C. S. Johnson, M. M. Thackeray, C. P. Grey, *J. Electrochem. Soc.*, **156** (2009) 730.

[70] R. D. Shannon, *Acta Crystallogr. Sect. A*, **32** (1976) 751.

[71] E. Rossen, J. N. Reimers, J. R. Dahn, *Solid State Ionics*, **62** (1993) 53.

[72] R. J. Gummow, D. C. Liles, M. M. Thackeray, *Mat. Res. Bull.*, **28** (1993) 235.

[73] N. Yabuuchi, Y. T. Kim, H. H. Li, Y. S. Horn, *Chem. Mater.*, **20** (2008) 4936.

[74] H. B. Yahia, M. Shikano, H. Kobayashi, *Chem. Mater.*, **25** (2013) 3687.

[75] N. Treuil, C. Labrugére, M. Menetrier, J. Portier, G. Campet, A. Deshayes, J. C. Frison, S. J. Hwang, S. W. Song, J. H. Choy, *J. Phys. Chem. B*, **103** (1999) 2100.

[76] P. Mustarelli, V. Massarotti, M. Bini, D. Capsoni, *Phys. Rev. B*, **55** (1997) 12018.

[77] J. Bréger, M. Jiang, N. Dupré, Y. S. Meng, Y. S. Horn, G. Ceder, C.P. Grey, *J. Solid State Chem.*, **178** (2005) 2575.

[78] J. Cabana, N. A. Chernova, J. Xiao, M. Roppolo, K. A. Aldi, M. S. Whittingham, C. P. Grey, *Inorg. Chem.*, **52** (2013) 8540.

[79] Y. J. Lee, C. Eng, C. P. Grey, *J. Electrochem. Soc.*, **148** (2001) A249.

[80] S. H. Park, S. -W. Oh, S. H. Kang, I. Belharouak, K. Amine, Y. -K. Sun, *Electrochim. Acta*, **52** (2007) 7226.

[81] N. Yabuuchi, K. Yoshii, S.T. Myung, I. Nakai, S. Komaba, *J. Am. Chem. Soc.*, **133** (2011) 4404.

Chapter VIII
Summary

Soft chemical synthetic method has applied to produce new chemical compositions in the lithium manganese oxide system utilizing the additional Ni. Co, and residual Na contents, and the crystal structure and chemical and electrochemical properties of the obtained materials were investigated from a view point of high capacity positive electrode material for lithium ion battery applications. In this thesis several results have been obtained as shown below :

Research on tunnel-type $Li_{0.44}MnO_2$ prepared by ion exchange method using $Na_{0.44}MnO_2$ as a starting material has also been reported. However, since the reported $Li_{0.44}MnO_2$ has a small Li content of 0.44, the charge capacity is about 100 mAh g^{-1}. For this reason, it has not reached a practical level and improvement of capacity is required. Recently, the specific capacity and discharge profile were improved by an additional Li insertion treatment in molten $LiNO_3$-LiOH salt at low temperature. The obtained $Li_{0.55}MnO_2$ sample exhibited the initial charge capacity of about 150 mAh g^{-1} with the average discharge voltage of 3.7 V vs. Li/Li$^+$. In addition, a further chemical lithiation treatment using LiI was performed to increase the Li content in the $Li_{0.82}MnO_2$ sample. The obtained $Li_{0.82}MnO_2$ sample exhibited the initial charge capacity of about 210 mAh g^{-1} between 4.8 and 2.5 V vs. Li/Li$^+$ with a fixed current density of 10 mA g^{-1} at 25 °C. However, the structural details of $Li_{0.44+x}MnO_2$, especially the Li site positions, have not been revealed yet, to our knowledge. By revealing the Li site positions, it is possible to estimate the maximum specific capacity of the crystal structure.

In the present research, we have successfully determined the precise positions of the Li atoms in $Li_{0.44+x}MnO_2$ for the first time. In $Li_{0.44+x}MnO_2$, the maximum Li content was found to be 0.80 by crystal structure analysis using powder neutron diffraction measurement. Further, from the electrochemical measurement, the specific capacity of $Li_{0.80}MnO_2$ was about 200 mAh g^{-1}. From this, it was possible to estimate the maximum specific capacity of $Li_{0.44+x}MnO_2$ by clarifying the Li sites of the crystal structure.

Lithium-deficient O6-$Li_xCo_{0.5}Mn_{0.5}O_2$ and O3-$Li_{2/3}Ni_{1/3}Mn_{2/3}O_2$ with layered rocksalt structure was prepared by ion-exchange of Na$^+$ for Li$^+$ from $Na_xCo_{0.5}Mn_{0.5}O_2$ and $Na_{2/3}Ni_{1/3}Mn_{2/3}O_2$ with layered rocksalt structure, respectively. A similar chemical composition of lithium-deficient O3-$Li_{0.7}Ni_{0.5}Mn_{0.5}O_2$ with layered rocksalt structure was reported to have a transformation of the crystal structure, depending on the heating temperature. Above 300 °C, the crystal structure of O3-$Li_{0.7}Ni_{0.5}Mn_{0.5}O_2$ transformed to spinel structure. However, phase transition from layered rock-salt to spinel structure by heat treatment has not been reported to be prepared by a soft-chemical method. We research phase transition from layered rock-salt to spinel structure by heat treatment, and electrochemical and structural properties of the samples are investigated for the first time.

In O6-$Li_xCo_{0.5}Mn_{0.5}O_2$ and O3-$Li_{2/3}Ni_{1/3}Mn_{2/3}O_2$, phase transition from layered rock-salt to spinel structure by heat treatment did not result in single phase but two phase coexistence of layered rock-salt and spinel structure. It was also found that the ratio of layered rock-salt and spinel structure can be controlled by heat treatment temperature.

A thermal treatment after the ion-exchange reaction using a molten salt improved the charge-discharge performance of O3-$Li_{2/3}Ni_{1/3}Mn_{2/3}O_2$. When O3-$Li_{2/3}Ni_{1/3}Mn_{2/3}O_2$ was heated at 500 °C, it exhibits a 5 V class plateau in its charge and discharge voltage-capacity curves. Furthermore, a large discharge capacity of 257 mA h g^{-1} was reported between 2.0 and 4.8 V.

Thermal treatment for $O3\text{-}Li_{2/3}Ni_{1/3}Mn_{2/3}O_2$ is extremely interesting as it affords better cycle performance, a higher discharge voltage and specific capacity than as-prepared $O3\text{-}Li_{2/3}Ni_{1/3}Mn_{2/3}O_2$. However, the experimentally demonstrated discharge voltage-capacity curve drastically decreases between 3.0 and 4.8 V because the spinel phase content increases as a result of heat treatment. Recently, a 5 wt% Na-doped NMC $(0.3Li_2MnO_3\text{-}0.7Li_{0.97}Na_{0.03}Mn_{0.33}Ni_{0.33}Co_{0.33}O_2)$ has been reported to suppress the spinel transition, and spinel-phase $LiNiMnO_4$ $(Li_{0.5}Ni_{0.5}Mn_{0.5}O_2)$ has been reported to be unstable. Hence, a control of the Na and Mn contents can improve the charge–discharge performance. Inspired by the preliminary studies, in this study we sought to synthesize $Na_xLi_{0.7-x}Ni_{1-y}Mn_yO_2$ and $Na_xLi_{0.67+y}Ni_{0.33}Mn_{0.67}O_2$ by thermal treatment. The residual Na content x in ion exchange and the Mn content y are utilized to clarify the impact of the charge and discharge voltage-capacity curves.

In $Na_xLi_{0.67-x}Ni_{0.33}Mn_{0.67}O_2$, $Li_{0.7}Ni_{1-y}Mn_yO_2$, and $Na_xLi_{0.67+y}Ni_{0.33}Mn_{0.67}O_2$, the ratio of layered rock-salt and spinel structure was controllable by residual Na amount and Mn amount in addition to the heat treatment temperature. The electrochemical properties were charge and discharge curves reflecting the crystal structure.

In summary, there are two points obtained from this study. First, the maximum specific capacity can be estimated by clarifying the Li sites. Second, by controlling the ratio of layered rock-salt and spinel structure, it is possible to provide an optimum charge and discharge curves according to the application. Accordingly, soft chemical synthetic technique is valid in controlling the chemical and electrochemical properties of new electrode materials.

The above results will contribute to the future studies on the development of new electrode materials with high capacity and high voltage for lithium ion battery applications

Acknowledgements